# A MEMS BASED DRUG EFFECT ANALYSIS SYSTEM UTILIZING DROPLET MICROFLUIDICS

A THESIS SUBMITTED TO
THE GRADUATE SCHOOL OF NATURAL AND APPLIED SCIENCES OF
MIDDLE EAST TECHNICAL UNIVERSITY
BY

METİN DÜNDAR ÖZKAN

IN PARTIAL FULFILLMENT OF THE REQUIREMENTS FOR THE DEGREE
OF MASTER OF SCIENCE
IN
THE DEPARTMENT OF ELECTRICAL AND ELECTRONICS ENGINEERING

JULY 2018

Approval of the thesis:

**A MEMS BASED DRUG EFFECT ANALYSIS SYSTEM UTILIZING DROPLET MICROFLUIDICS**

Submitted by **METİN DÜNDAR ÖZKAN** in partial fulfillment of the requirements for the degree of **Master of Science in the Department of Electrical and Electronics Engineering, Middle East Technical University** by,

Prof. Dr. Halil KALIPÇILAR _____
Director, **Graduate School of Natural and Applied Sciences, METU**

Prof. Dr. Tolga ÇİLOĞLU _____
Head of Department, **Electrical and Electronics Engineering, METU**

Prof. Dr. Haluk KÜLAH _____
Supervisor, **Electrical and Electronics Engineering, METU**

Assoc. Prof. Dr. Ender YILDIRIM _____
Co-Supervisor, **Mechanical Engineering, Çankaya University**

**Examining Committee Members:**

Prof. Dr. Tayfun AKIN _____
Electrical and Electronics Engineering, METU

Prof. Dr. Haluk KÜLAH _____
Electrical and Electronics Engineering, METU

Assoc. Prof. Dr. Ender YILDIRIM _____
Mechanical Engineering, Çankaya University

Assist. Prof. Dr. Serdar KOCAMAN _____
Electrical and Electronics Engineering, METU

Assist. Prof. Dr. Kıvanç AZGIN _____
Mechanical Engineering, METU

**Date:**
18.07.2018

**I hereby declare that all information in this document has been obtained and presented in accordance with academic rules and ethical conduct. I also declare that, as required by these rules and conduct, I have fully cited and referenced all material and results that are not original to this wok.**

**Name, Last name : Metin Dündar Özkan**

**Signature :** _____

## ABSTRACT

A MEMS BASED DRUG EFFECT ANALYSIS SYSTEM UTILIZING DROPLET MICROFLUIDICS

Özkan, Metin Dündar

M.Sc., Department of Electrical and Electronics Engineering

Supervisor: Prof. Dr. Haluk Külah

Co-Supervisor: Assoc. Prof. Dr. Ender Yıldırım

July 2018, 104 pages

**Keywords:** Electrostatic microvalve, normally closed, Microelectromechanical Systems (MEMS), lab-on-a-chip, droplet microfluidics, drug effect analysis.

This thesis proposes a fully integrated lab-on-a-chip system designed for drug effect analysis based on the droplet microfluidics. It is mainly designed for screening multi-drug responses of cells in an automated operation. The distinguished feature of the drug screening system is that it includes droplet-based single cell encapsulation. The system includes two main subsystems which are parylene-based and normally closed electrostatic microvalves and droplet generation system. The integration of microvalves with droplet system enabled an automated system for screening drug effects on K-562 leukemia cells because the valves allow or block the flows of drugs to be able to simultaneous observe multiple drugs and their combinations. Drug

screening analysis was applied on singly encapsulated cells within the droplets. Flow-focusing junction was used to form the picolitre-droplets at a frequency of 130 Hz.

For electrostatic microvalves, the theoretical analysis of the valve operation was discussed based-on 1-D lumped model, continuous reduced-order model, and finite element analysis. The details of the first-generation design, its operation principle and step-by-step fabrication procedure were provided. The fabricated microvalve with 300 µm-radius and spiral top electrode were tested. The pull-in voltage was measured to be 177 V and while the pull-out occurred at 95 V. Moreover, the opening duration of the valve was 0.94 s and the valve was closed in 1.86 s. Besides the design details and operational characterization, the important point here is to obtain a microvalve in smooth operation and directly usable in the system all the time. Further, the improvement in the performance of the valves was necessary for the intended application. Thus, the second-generation microvalve design was proposed. By first providing the fabrication procedure, the valves with 300 µm-radius and full top electrode was tested, and they operated at a pull-in voltage of 76 ± 11.4 V, and then this voltage was reduced to 41.5 ± 7.8 V for 410 µm-valve with spiral top electrode. The valves could respond to voltage variation in less than 1 s while opening; yet the closing duration was slightly greater as 1.5- 2.8 s.

The system operated at -10 kPa outlet vacuum pressure for high-frequency droplet formation. After performing a control group experiment for the viability of cells without any drug, the responses of encapsulated cells in different drug droplets were observed over 2 hours using the fluorescence intensity change based on CTCF method under fluorescent microscope as the proof-of concept.

# ÖZ

DAMLACIK MİCROAKIŞKANLARINI KULLANAN MEMS TABANLI İLAÇ ETKİSİ ANALİZ SİSTEMİ

Özkan, Metin Dündar

Yüksek Lisans, Elektrik ve Elektronik Mühendisliği Bölümü

Tez Yöneticisi: Prof. Dr. Haluk Külah

Ortak Tez Yöneticisi: Doç. Dr. Ender Yıldırım

Temmuz 2018, 104 sayfa

**Anahtar Sözcükler:** Elektrostatic mikrovalf, normalde kapalı, Mikroelektromekanik Sistemler (MEMS), çip-üstü laboratuvar, damlacık mikroakışkanları, ilaç etkisi analizi.

Bu tez, damlacık mikroakışkanlara dayanan ilaç etkisi analizi için tasarlanmış tamamen entegre bir çip-üstü-laboratuar sistemi önermektedir. Esas olarak, otomatik şekilde hücrelerin çoklu ilaç tepkilerini taramak için tasarlanmıştır. İlaç tarama sisteminin ayırt edici özelliği, damlacık bazlı tekil hücre hapsetmesini içermesidir. Sistem, parilen bazlı ve normalde kapalı elektrostatik mikrovalfler ve damlacık üretim sistemi olarak iki ana alt sistemi içerir. Mikrovalflerin damlacık sistemiyle entegrasyonu ile beraber K-562 lösemi hücrelerinde ilaç etkilerini taramak için otomatik bir sistem sağlanmıştır çünkü valfler, ilaçların akışlarının çoklu ilaçları ve bunların kombinasyonlarını eşzamanlı olarak gözlemleyebilmesine izin vermekte veya

engellemektedir. İlaç etkisi tarama analizi damlacıklar içinde tek başına hapsedilmiş hücreler üzerinde uygulanmıştır. Akışa odaklanan birleşme noktası, 130 Hz'lik bir frekansta pikolitre hacimli damlacıklarını oluşturmak için kullanılmıştır.

Elektrostatik mikrovalfler için, valf operasyonunun teorik analizi, 1-D toplanmış model, sürekli indirgenmiş sıralı model ve sonlu elemanlar analizine dayanılarak tartışılmıştır. Birinci nesil tasarımın detayları, çalışma prensibi ve adım adım üretim prosedürü sağlanmıştır. 300 mikron yarıçaplı ve spiral üst elektrotlu olarak üretilmiş mikrovalf test edilmiştir. Çekme gerilimi 177 V olarak ölçülmüş ve çekilme ise 95 V'de gerçekleşmiştir. Ayrıca, valfin açılma süresi 0.94 s iken valf 1.86 s'de kapatılmıştır. Tasarım detayları ve karakterizasyonun yanı sıra, buradaki bir önemli detay, düzgün bir şekilde çalışan ve sistemde her zaman doğrudan kullanılabilen bir mikrovalf elde etmektir. Ayrıca, amaçlanan uygulama için valflerin performansında gelişme gerekliliği oluşmuştur. Böylece ikinci nesil mikrovalf tasarımı önerilmiştir. İlk önce üretim prosedürünü sağlayarak, 300 mikron yarıçapındaki ve tam üst elektrotlu valfler test edilmiş ve bunlar 76 ± 11.4 V'lik bir çekme geriliminde çalıştırılmış ve daha sonra bu voltaj üst elektrotu spiral ve 410 mikronluk valfler ile 41.5 ± 7.8 V'ye düşürülmüştür. Valfler, açılma sırasında 1 saniyeden daha az sürede voltaj değişimlerine cevap verebilmiş; kapanış süresi ise 1.5 - 2.8 s'den biraz daha fazla olmuştur.

Sistem, yüksek frekanslı damlacık oluşumu için -10 kPa çıkış vakum basıncında çalıştırılmıştır. Herhangi bir ilaca maruz kalmayan hücrelerin yaşayabilirliği için bir kontrol grubu deneyi gerçekleştirdikten sonra, farklı ilaç damlacıklarında hapsedilmiş hücrelerin tepkileri, konsepti kanıtlamak için floresan mikroskop altında CTCF yöntemine dayalı floresan yoğunluk değişimi kullanılarak 2 saat boyunca gözlemlenmiştir.

*To My Family*

## ACKNOWLEDGMENTS

I would like to, firstly and most importantly, express sincerest gratitude to my family not only for their support in the duration of this thesis but also for their love, motivation, faith and advices during my entire life. They believed in me in every respect and I was not be able to do this without their supports. I would like to express my deepest gratitude to my supervisor Prof. Dr. Haluk Külah who have been supportive and encourager. I am indebted to him, to his belief in me and to the share of excitement towards the achievements in our projects and in our lives. It has been an incredible experience to be part of his research team for excellent three years. I am also truly grateful to my co-supervisor Assist. Prof. Ender Yıldırım. His precious guidance, comments, support, and insightful perspective for both professional and personal respects made my study enriched and added value. I have learnt a lot from him and am lucky that I had the opportunity to work with him. For her invaluable remarks, opinions and motivations, I would like to thank to Assoc. Prof. Ebru Özgür. Her motivation and suggestions in the meetings powered us all the time.

I specially thank to my project-partners Ali Can Atik and Maryam Parsiyan for the valuable times to work with them and for their help in any respect. It was true fun to have enjoyable times in daily life and at work and brainstorming with Ali Can and Maryam. I am deeply thankful to Kaan Sel, Volkan Mehmet İşlek, Hüseyin Boyacı, Deniz Sargun, Onur Memioğlu, Berker Peköz and Miraç Eren Aydoğan, all of whom have been my close friends for more than eight years in ODTÜ. I would like to also thank to all members of BioMEMS research group for their collaborations and supports, but most importantly for their sincere friendship. In no specific order, I am thankful to Kaan Sel, Furkan Gökçe, Mahmut Kamil Aslan, Bedirhan İlik, Hasan Uluşan, Taylan Berkin Töral, Salar Chamanian, Eren Aydın, Aziz Koyuncuoğlu, Mustafa Kangül, Begüm Şen Doğan, Parinaz Ahsrafi Özkayar, Gürhan Özkayar, Zeynep Çağlayan, Yağmur Demircan, Berat Yüksel, Berkay Çiftçi, Didem Çetin,

Andaç Yiğit, Alper Kaan Soydan, Ahmet Efe and Dilek Işık, and also to Aysel Büyükbaş Uluşan, and Pardis Chamanian who are counted as our group member.

Moreover, I am indebted especially to Taylan Berkin Töral, Adem Saraç, Levent Abat, Orhan Akar and all METU MEMS researchers for their guidance and helps in the fabrication. During this study, I gratefully acknowledge the financial support of the Scientific and Technological Research Council of Turkey, TÜBİTAK on the project with the grant number 114E098, and also the financial support of Ministry of Development.

**TABLE OF CONTENTS**

## LIST OF TABLES

## LIST OF FIGURES

## LIST OF ABBREVIATIONS

| | |
|---|---|
| **CPD** | Critical Point Drying |
| **FEA** | Finite Element Analysis |
| **IPA** | Isopropyl Alcohol |
| **LOC** | Lab-on-a-chip |
| **MEMS** | Microelectromechanical Systems |
| **ODE** | Ordinary Differential Equation |
| **PDE** | Partial Differential Equation |
| **PET** | Positron Emission Tomography |
| **PDMS** | Polydimethylsiloxane |
| **SAM** | Self-Assembled Monolayer |
| **SEM** | Scanning Electron Microscope |
| **RPMI** | Roswell Park Memorial Institute Medium |
| **μTAS** | Micro Total Analysis System |

# CHAPTER 1

## INTRODUCTION

The demand for small but fast, cheap and functional systems has revolutionized the technologies for the benefit of our lives in terms of mobile activities. Miniaturization of the systems while increasing their performance has, for this reason, been an interest for researchers and engineers in a broad range of areas including electronics as well as other fields of engineering. For the electronics point of view, the technological improvements in microfabrication techniques has led to the progression of semiconductor and integrated circuit industries. A well-known reflection of miniaturization idea in electronics is Moore's law which predicts that the number of transistors on a chip doubles every 1.5 to 2 years. Mechanics has also taken its share of trend of making smaller by evolving to micromechanics. Further, the introduction of microelectromechanical systems (MEMS) widened the outlook of miniaturized mechanics by the integration of electrical and mechanical components that can have a critical physical dimension ranging from millimeters to micrometers. As MEMS device fabrication is realized by standard batch-processing methods, the pace of the dramatic progresses in silicon fabrication technology has pave the way of MEMS, enhancing the capabilities by creating diverse fields. Today, the application areas include industries of automotive (accelerometers for airbag systems and gyroscopes), biomedical (pacemakers, drug delivery systems, microsurgery tools), telecommunication (smart antennas), household appliances (pressure sensors for water level detection, washing machines, air conditioner,), consumer applications (inkjet printers, DLP projectors, smartphones, Nintendo Wii) and defense applications (low cost night vision, home security systems), as illustrated in Figure 1.1.


**Figure 1.1.** Diverse application fields of MicroElectroMechanical Systems (adapted from [1]).

Because of its distinct advantages, the concept of miniaturization has created and still continues to create new markets. Among the variety, one deserves a special attention. The need towards miniaturization of analytic chemistry motivated the use of MEMS technology. In 1990, it was Manz *et al.* [2] who laid the foundations of miniaturized total analysis systems (μTAS). They theoretically showed that the modular combination of miniaturized components could be used to automatically perform all sample handling steps such as sampling, transport, sample pretreatment, detection and data analysis. In addition to the reduction of device size, the driving forces behind the prevalence of these systems were actually the need for more accurate results with the increase in the throughput. Later, due to their implementation at micro levels by means of MEMS fabrication techniques, they were revolutionized, and started to be referred as micro total analysis systems, also known as “lab-on-a-chip” (LOC) systems. These systems downsize all laboratory facilities into small sample area and enable small

volume of reagent usage, high throughput and detailed analyses of high quality at low costs for short analysis times.

Most of the LOC systems are shaped around microfluidics as it has emerged and gained popularity due to the fact that the origins of microfluidics [3] is based on the miniaturization of analytical methods. The revolution of the chemical and molecular analysis with microfluidics has been achieved first by gas-phase chromatography [4], high-pressure liquid chromatography [5] and capillary electrophoresis [6]. Later, the improvements in the performance of microfluidic LOC systems have increased their popularity over two decades by gathering various fields including chemistry, biology, material science and many engineering disciplines. This allows wide range of application areas to emerge such as microanalytical chemistry [7], drug discovery [8], drug delivery [9], clinical diagnostics [10], proteomics [11], genomics [12] and single cell applications [13], all of which benefit from the field of microfluidics.

## 1.1. Droplet-Based Drug Effect Analysis in Cancer Research

### 1.1.1. Droplet Microfluidics

Since the emergence of technology developed for the microscale research of fluid flows, a variety of microfluidic techniques has been proposed to find solutions for the analytical and biological problems. Most of the microfluidic systems are based on the manipulation of continuous flow of several miscible fluids in the microchannel. The flows are usually controlled by pressure driven flows using a syringe pump or vacuum pump, and also by electroosmotic flow or interfacial tension driven flow [14]. However, the continuous flow systems may have some drawbacks for specific applications. For example, if an analysis needs to be carried out where many fluids are present, cross-contamination between samples may occur due to intimate contact of different molecules with channel walls [15]. Microvalves can be used for physical isolation of fluids; however the contamination of sample plugs can still occur due to

Taylor dispersion—a phenomena describing the convection of inhomogeneous fluids in a laminar-flow microchannel [15], [16].

In contrast to continuous flow systems, droplet microfluidics is an alternative method to avoid the aforementioned issues. Droplets have the capability of serving as picolitre-microreactors to ensure the confinement of reactants in fluidic material and thus to compartmentalize the reactions by the help of interfacial forces, which eliminates the cross-contamination caused through sample-contact channels. Moreover, the technology provides all the generic advantages peculiar to fluidic operations at microscale. It offers usage of small volume of reagents, rapid analysis and high throughput screening. Distinctively, droplet microfluidics enables the analysis of large number of droplets without the need for complex analysis and large device sizes. All these distinguishing features highlight droplet microfluidics for many applications of biomedical research.

In the literature, different applications of droplet-based systems are available such as analyses of protein expression [17], gene expression [18], polymerase chain reaction [19]–[22], enzyme kinetics [23], chemical reactions [24], synthesis of microparticles [25], [26] and single cell encapsulation [27]–[29].

### 1.1.2. Droplet-Based Single Cell Analysis

The cellular specificity is crucial in cell biology, biochemistry and genetics, and thus a need-to-consider feature in understanding of certain activities at cellular levels. The concept predicates that the activity of every cell, even isogenic cells, may differ from each other [30]. The conventional methods assume that the individual cell responses are similar and can be deduced from average of cell culture. However, the dominant biological mechanism of each cell does not always correspond to population averages since the individual cells can have different molecular structures due to functional variations. The results of ensemble cell measurements can therefore be misleading. In concern with this, cell responses can be vitally significant in cancer therapies because

the sensitivities of each cancer cell against the same drug type is often heterogeneous. This may lead to the failure of cancer treatment or recurrence of disease. For this reason, a more accurate interpretation is needed to examine the cell-to-cell variations [31], [32].

The fact that single cell analysis is crucial in specific applications has led to the development of different tools, methods and protocols to analyze the cells individually. Droplet-based approaches have started to be used as a powerful method for analysis of individual cells. The single cells are immobilized within droplets of picolitre volumes, forming chemically isolated micro reactors where the response of individual cells can be individually detected (Figure 1.2). This decreases the biological noise, improves the quality of experiments and data analyses.

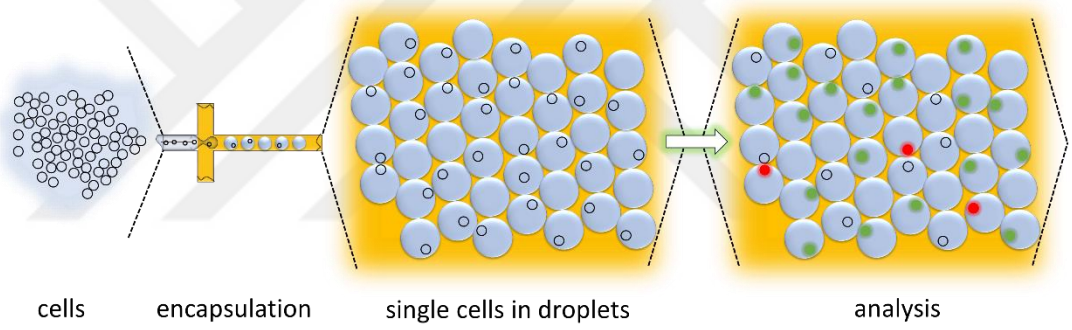


**Figure 1.2.** Cell encapsulation and analysis with fluorescence microscopy using droplet microfluidics.

Once the droplet-based single cell assays have been recognized for the great potential in cancer diagnosis and therapies by researchers, droplet-based platforms have been favored to screen drug-cell interactions in this regard. Brouzes *et al.* [27] analyzed the interaction of U937 human cells with Mitomycin C by encapsulating the cells within the droplets. However, the system was not fully integrated in this work. The formation of the droplet library containing the drug-cell mixture and the observation of these droplets cannot be performed simultaneously on the same chip. Kim *et al.* [29] demonstrated a microfluidic platform on which single-cell screening was performed for long-term culture and analysis of the cell growth rates by trapping cells in an array.

After on-chip fluorescent tagging, target cells showing traits of interest could be extracted for further analyses. Similarly, Gong *et al.* [33] reported a droplet-based microfluidic device for cytotoxicity observation. The efficiency of cytochalasin D drug solution on human breast cancer cells was investigated by using the fluorescence activity of Calcein AM.

## 1.2. Background Information on Microvalves

The power of microfluidics has become a stubborn fact for researchers. What makes microfluidics more powerful than it has been is the ability to integrate microchannel networks with internal or external functional components such as sensors, mixers, dividers, pumps, valves etc. The realization of integrated systems with such components make the implementation of complex three-dimensional analyses possible, which renders these systems superior to the conventional. The manipulation of sample flows may rise as a requirement for some applications. In this sense, micropumps can be used to transfer small volume-fluids by controlling their flows at high precision. Also, microvalves are in use within microfluidic systems for flow manipulation. They fulfill not only the control of the flows but also the demands on separation, timing and controlling the flow rate. These functions are usually achieved by utilizing a movable element. Such systems can have substantial potential in the applications where large number of samples are required to be run in order to avoid cross-contamination and to reduce the analysis time significantly.

Table 1.1 provides insight into general classification of microvalves proposed in the literature [34]. Microvalves can be mainly divided into two groups as passive and active microvalves. Passive microvalves have no moving components, which, thus, does not necessitate the use of energy sources. They can be sorted as mechanical passive—check valve [35] and non-mechanical passive—capillary [36] microvalve. On the other hand, active microvalves contain a moving element—membrane or valve seat, determining the on/off mode of microvalves by means of external sources. They are also grouped as mechanical active—electrokinetic [37], [38], electromagnetic

[39]–[41], piezoelectric [42]–[44], electrostatic [45]–[47], and non-mechanical active microvalves—electrochemical [48]–[51], phase change [52], [53], and external active—pneumatic [54]–[57], modular [58] microvalves. In addition, microvalves can be also classified depending on their initial working mode as normally open, normally closed and bistable microvalves. The actuation mechanisms and fundamental configurations of various active microvalves such as pneumatic, piezoelectric, electrostatic and electrochemical are visualized in Figure 1.3.

Among the all types, the miniaturization of valves was first realized by electromagnetic microvalves. The first microvalve was designed by Terry *et al.* [4] in 1979 for a gas chromatographic air analyzer system, and fabricated on a silicon substrate. The operation of mechanism is based on electromagnetic actuation force provided by the change in the magnetic flux density in the motion of direction. Magnetic field is generated with solenoid actuators having coils that are electrically driven. The membrane is deflected due to the motion of movable magnetic material towards the static magnetic material, magnets or metal bars (Figure 1.3.g). Electromagnetic valves enable large deflection of membrane with fast actuation. Nonetheless they have disadvantages of lowering the efficiency due to increase in the heat generation, and off-chip connection requirement for magnets or solenoids [59].

Electrochemical microvalves utilizes the principle of pressure built-up during the electrolysis of water by evolving oxygen (Figure 1.3.h). The membrane is deflected due to this pressure. The concept of electrochemical actuation was first suggested by Neagu *et al.* in 1996 [49]. Pneumatic valves, on the other hand, have the simplest working mechanism compared to others (Figure 1.3.a). It was first introduced by Quake *et al.* in 2000 [60], consisting of two orthogonal channels. A thin elastomeric diaphragm between the channels falls and blocks the flow by pressurizing the top channel. Pneumatic valves are preferable in complex analysis systems for reliability and their easy implementation. As a drawback, they require bulky off-chip connections such as external solenoid valves, control circuit and gas tank, which limits their use at point-of-care [61]. Also, they have slow response time greater than 1 s.

**Table 1.1.** Classification of microvalves (adapted from [34]).

| **Categories** | | | |
|---|---|---|---|
| **Passive** | Mechanical | Check Valve | Flap |
| | | | Membrane |
| | | | Ball |
| | | | In-line mobile structure |
| | Non-mechanical | | Diffuser |
| | | Capillary | Abrupt |
| | | | Liquid triggered |
| | | | Burst |
| | | | Hydrophobic valve |
| | | | |
| **Active** | Mechanical | Magnetic | External magnetic fields |
| | | | Integrated magnetic |
| | | Electric | Electrostatic |
| | | | Electrokinetic |
| | | Piezoelectric | |
| | | Thermal | Bimetallic |
| | | | Thermopneumatic |
| | | | Shape memory alloy |
| | | Bistable | |
| | Non-mechanical | Electrochemical | |
| | | Phase change | Hydrogel |
| | | | Sol-gel |
| | | | Paraffin |
| | | Rheological | Electro-rheological |
| | | | Ferrofluids |
| | External | Modular | Built-in |
| | | | Rotary |
| | | Pneumatic | Membrane |
| | | | In-line |

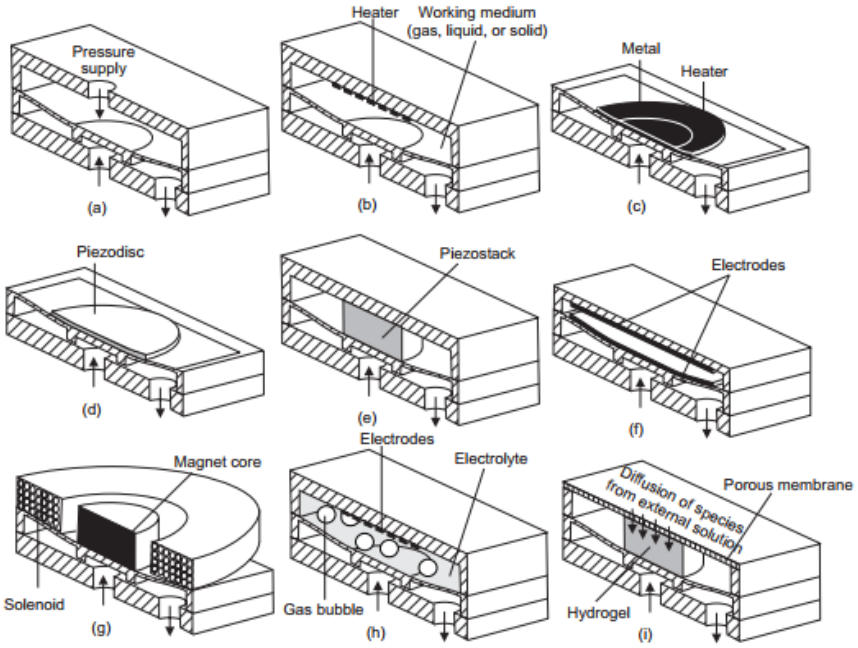


**Figure 1.3.** Basic Actuation mechanisms of various active microvalves. a) pneumatic, b) thermopneumatic, c) thermomechanic, d) piezoelectric, e) piezoelectric, f) electrostatic, g) electromagnetic, h) electrochemical, and i) chemical microvalves (adapted from [62]).

In electrostatic microvalves, two oppositely charged plates are attracted to generate the electrostatic force (Figure 1.3.c). They offer fast response characteristics with high reliability among different microvalves; yet high actuation voltage is required. Electrostatic microvalves provide moderate displacement when compared to magnetic and piezoelectric counterparts. Their fabrication can be easily done by standard microfabrication techniques and materials. Yet, they were not able to sufficiently attract researchers' attention in microfluidic applications because electrostatic actuation results in electrolysis of working fluids. However, the application of AC drive voltage at high frequencies is proven to be useful in preventing the electrolysis [63]. Chang *et al.* [64] demonstrated the operation of a PDMS-based electrostatic microvalve. They applied 15-20 V ac voltage to the valve at a frequency of 5 MHz, where the drive voltage depends on the electrical properties of fluid material.

Microvalves have substantial application areas from biomedical, analytic chemistry to automotive industry. The actuator type used in microvalve has an impact on the miniaturization of the component. Thus, the energy density stored in actuators is an important criteria to compare the performance of valves [62]. Table 1.2 serves a basis for comparison of actuation mechanisms of microvalves in terms of maximum pressure, response time and operational energy. According to the table, electrostatic microvalve is the most efficient valve in terms of energy stored. The operational pressure is in the lowest levels (01.-100 kPa), with the fastest response time, on the order of $10^{-5}$ seconds. In addition, it retains a small footprint (<600 µm). Considering its advantages, electrostatic microvalve can be a reasonable choice depending on the microfluidic applications.

**Table 1.2.** Pressure, time response, and operational energy density ranges of different microvalves (adapted from [62]).

| **Actuation Mechanism** | **Maximum Pressure (kPa)** | **Response Time (s)** | **Operational Energy ($J/m^3$)** |
|---|---|---|---|
| Electromagnetic | 0.1-100 | $10^{-4}$-$10^{-3}$ | - |
| Disk piezoelectric | 0.1-100 | $10^{-4}$-$10^{-3}$ | $10^{7}$ |
| Electrostatic | 0.1-100 | $10^{-5}$ | $10^{2}$-$10^{3}$ |
| Electrochemical | 0.1-100 | 1-10 | $10^{2}$-$10^{4}$ |
| Chemical | 10-100 | 1-10 | $10^{5}$ |
| Pneumatic | $10^{2}$-$10^{3}$ | 1-10 | $10^{6}$ |
| Thermopneumatic | $10^{2}$-$10^{4}$ | $10^{-3}$-1 | $10^{6}$ |
| Shape memory alloy | $10^{2}$-$10^{4}$ | $10^{-3}$-0.1 | $10^{7}$ |
| Thermomechanic | $10^{2}$-$10^{4}$ | $10^{-3}$-0.1 | $10^{7}$ |
| Stack piezoelectric | 0.1-100 | $10^{4}$-$10^{5}$ | $10^{7}$ |

## 1.3. Objective of Thesis

This thesis proposes a lab-on-a-chip system that can be potentially used for patient-specific and combinatorial drug therapy of cancer diseases. The system is designed in such a way that it is fully integrated with electrostatic microvalves to enable automated

operation and includes droplet-based single cell encapsulation for accurate drug effect screening. The objectives of this thesis can be designated as follows:

1. *Droplet-based drug screening system:* A high throughput and fully integrated multi drug screening platform is developed. The system has two main subsystems which are droplet formation system and electrostatic microvalves.

2. *Droplet formation system:* The LOC system is based on the droplet microfluidics technology. Droplets are formed using a designed microchannel network that can perform various operations such as mixing the liquids, forming droplets and collecting the droplets in the chambers for observation. Then, they are used to immobilize the cancer cells inside so that single cell analysis can be achieved. Flow focusing junction-based droplet formation tests are performed to achieve single cell encapsulation.

3. *Re-designing a normally closed electrostatic microvalve:* The first version the electrostatic microvalve was designed by Assoc. Prof. Ender Yıldırım [65]–[67]. The valves are integrated with a microchannel network to operate as switches. The use of electrostatic microvalves allows for the screening of more than one drug in the droplet-based drug screening system, and thus the different dosages to be tested. After the first implementation of the valve, design alterations are deemed necessary because the problems and difficulties encountered during the fabrication and testing of the valves must be overcome for the system integration. For this reason, the normally closed electrostatic microvalve is redesigned by offering solutions to the problems, fabricated using MEMS technology and tested to assess its performance in terms of important figure of merits including pull-in and pull-out voltages, response time and reliability.

4. *Drug effect screening tests:* Based on the established concept, high-throughput cytotoxicity screening of K-562 leukemia cells using anti-cancer drugs and their combinations are dynamically observed for the proof-of-concept.

## 1.4. Organization of Thesis

In Chapter 1, miniaturization concept was introduced by defining MEMS technology and its contribution on the improvement of different technologies. The advantages that μTAS and LOC systems offer for microfluidics was mentioned. Droplet microfluidics and its advantages over the continuous flow was described with application examples. Among these, single cell analysis application was main the focus. Encapsulation of cells in droplets were exemplified by reviewing the literature especially for oncological research. The relation between droplet-based single cell analysis and cancer drug effect analysis was presented. Then, the function of microvalves was described with a brief introduction of various types of valves. Of the common types, the electrostatic microvalve was chosen for the discussion owing to its superiority in response time, pressure range and minimizing the off-chip requirement of LOC systems.

Chapter 2 describes the droplet-based micro total analysis system. The integration of electrostatically actuated microvalves with microchannel network capable of mixing liquids, forming droplets and collecting them in chambers were described and the working principle together with the general view of total analysis system are explained by visual examples. Also, and the basics of droplet microfluidics were discussed briefly and the test results for droplet formation and single cell encapsulation were given.

Chapter 3 is the chapter in which the design, fabrication and characterization of a normally closed electrostatic microvalve is thoroughly discussed. First, theory behind the circular membrane operation is explained and the first-generation design of the valve is suggested. The validity of the design is proven with the simulation results. The MEMS fabrication process of the microvalve is illustrated with images and explained in detail. Some problems were observed during the fabrication and these are elaborated with their solutions. Then, the characterization of the valve in terms of important parameters is discussed. Upon insufficient application specifications, the

second-generation electrostatic microvalve design is proposed instead of the first-generation. The fabrication processes are reviewed with the applied changes. The operational performance is tested in terms of key parameters, and at the end two different design proposals are briefly compared with each other.

In Chapter 4, the fabrication process of μTAS is provided. The drug effect analysis using K-562 cancer cells are shared and the results are discussed for control and medicated group experiments based on CTCF method.

The last chapter, Chapter 5 summarizes the overall work, and highlights the key points of the thesis. Also, the governing idea, future works and suggestions related to research topic are provided at the very end.

Moreover, Appendix A enlarges upon the steps of the electrostatic microvalve fabrication for the two different generation designs presented in this thesis.

# CHAPTER 2

# A FULLY INTEGRATED DROPLET-BASED DRUG EFFECT ANALYSIS SYSTEM

## 2.1. Lab-on-a-chip System Description and Operation Principle

There is a clear need in the literature for a fully integrated total analysis system to observe the drug-individual cell interactions. Droplet based drug screening systems designed so far are neither fully integrated nor suitable for multi-drug effect analysis to screen the effects of different drugs and their combinations. In addition to integrability and multi drug observability, the system should fulfill the requirements in revealing the cell heterogeneity. To fill this gap for targeted therapy, the system necessitates the following mechanisms: selecting different drugs on the chip, controlling the dosages of the drugs within the droplets, being able to separate droplets of different drugs, and keeping these droplets on the chip during the incubation period. As a result of fulfilling the criteria, the control of channel flows is regarded as a must. Microvalves can be used for this purpose, and all the above mechanisms can be accomplished using the valves. Due to their aforementioned advantages, electrostatic microvalves can be preferred in this work for flow manipulation of the fluids in the microchannels.

The proposed LOC system in this thesis enables multi-drug screening of individually encapsulated leukemia cancer cells within anti-cancer drug droplets. The flows are manipulated by normally closed on-chip electrostatic microvalves. Large numbers of single cells are treated by multiple drugs and their combinations in a relatively short period of time. High-throughput cytotoxicity for the target cells can be simultaneously observed in the observation areas composed of spiral channels. In this regard, the

system can be regarded as a promising tool for personal and targeted therapies in treatment of cancer disease.

Figure 2.1 illustrates the combinatorial drug effect analysis system integrated with five normally closed electrostatic microvalves. The dark blue circles located on the microchannels indicate the normally closed electrostatically actuated microvalves, two of which are at the inlet side whereas the other three are at the outlet side. Besides microvalves, the system consists of micromixer unit for rapid homogenous mixing of miscible fluids, X-junction known also as flow-focusing junction for high-throughput droplet formation and single cell encapsulation and lastly spiral-type observation areas to collect the droplets for cytotoxicity screening.

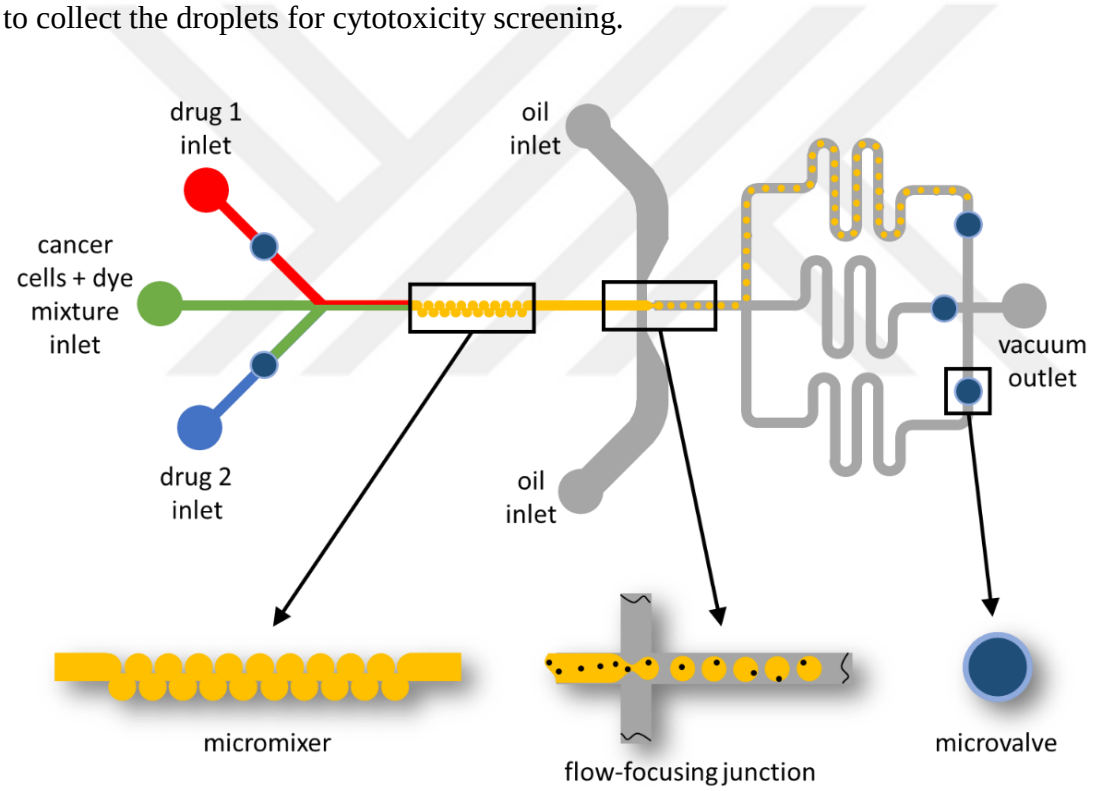


**Figure 2.1.** Integrated lab-on-a-chip system for droplet-based multi-drug screening.

The system operation is visually explained in Figure 2.2, and it works as follows in principle:

1. The experiment starts with obtaining the control group. Without opening any microvalve at the inlet side and thus without using any drug, cell suspension and dye content is first directed to micromixer unit. The micromixer is also used for focusing the cells to the middle of the channel with certain distances in between so that cells are individually encapsulated. Later, the mixture is dispersed at the flow focusing junction by orthogonal and symmetric oil flows. Since the cell suspension and oil are immiscible fluids, droplets containing single cell break off. Droplets flow through the serpentine channel and delivered to upper observation area by opening only microvalve #3. Then, the opened microvalve is closed to collect the droplets in the spiral microchannels.

2. When the microvalves #1 and #4 are opened, drug 1 and cell suspension with fluorescent dye come across at the Y-junction and the mixture is canalized to micromixer structure for rapid mixing. After flowing through the mixer, the mixture of drug 1 and cell suspension meet with lateral oil flows and the generated droplets are gathered at middle observation channels.

3. The corresponding microvalves #2 and #5 at the inlet and outlet sides are opened, and the same procedure is applied for the drug 2. At the end, droplets of drug 2 are collected in the lower spiral microchannels.

After collecting droplets of different drugs within different spiral observation areas, cell viability observation can be made under fluorescent microscope, at the same time. During the viability tests, live cells will fluoresce while fluorescence emission of cells starting to die will decrease. In this way, the effect of drugs on single cells whose responses are independent of each other can be detected.

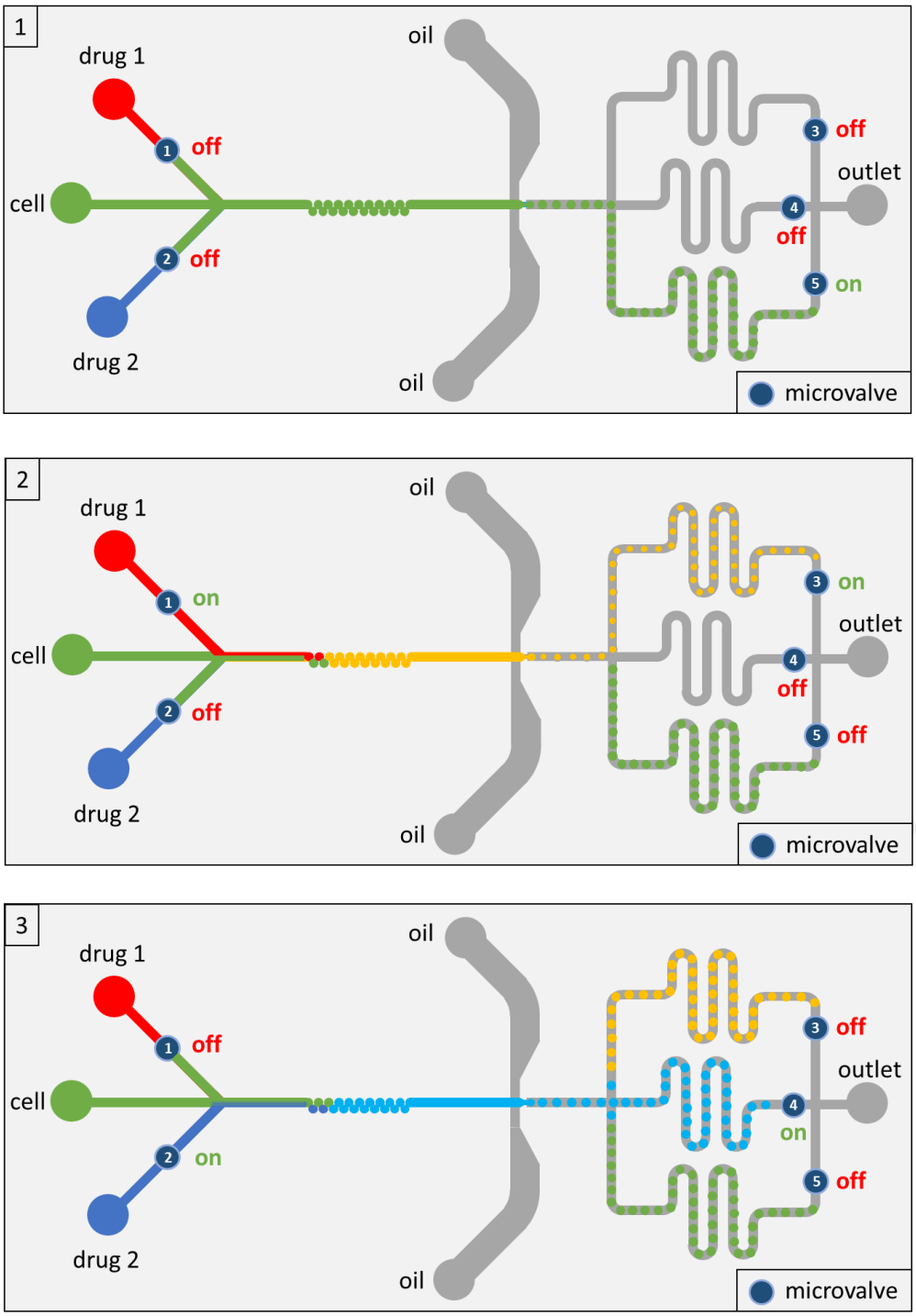


**Figure 2.2.** Working principle of droplet-based multi-drug screening LOC system.

## 2.2. Droplet Formation System

### 2.2.1. Droplet Microfluidics Dynamics

Droplet microfluidics is a significant branch of microfluidics in which continuous fluid phase flow is used to generate pico- or micro-liter droplets of another immiscible phase. While it miniaturizes the biological and chemical processes with small reagent usage at short analysis durations, the unique advantage of droplet microfluidics is the ability to compartmentalize the reactants from the environment and eliminate the risk of cross-contamination of samples. The applications of droplet microfluidics were mentioned in Section 1.1.1. One of the main field of usage of droplet microfluidics is single cell encapsulation. Since the cells can behave heterogeneously in respond to the same factors, it is important to analyze cellular activities individually. This can be of vital in diagnostics of diseases and improves the quality of the results. Moreover, droplet microfluidics offer great potential for high throughput results as the thousands of droplets can even be generated in couple of seconds.

The dynamics of droplet formation can be summarized as follows: In two-phase droplet generation, immiscible fluids are utilized. The fluid having the highest affinity becomes the continuous phase, and the other one with lower affinity is called dispersed phase. Typically, the former is selected from different oil types (silicone, fluorinated, etc.) or air while the latter is selected as water or other fluidic mixtures depending on the application. Droplet generation occurs when the viscous forces exerted by continuous phase overcomes the shear forces of dispersed fluid phase. Other than these factors, the generation dynamics are determined by wetting properties, flow rates, interfacial tension and nozzle geometry. The generation of segments is performed using mainly three geometries—flow focusing, T-junction and co-flowing [68], [69]. Flow focusing is one method of droplet generation [70]–[72]. In this geometry, the flow of dispersed phase is cut by two lateral continuous phases and extruded through a small orifice, which provides more symmetric shearing. This allows improved control over droplet generation and droplet stability. Figure 2.3.a depicts the flow

focusing junction configuration. In T-junction, the dispersed phase and carrier phase come across at an orthogonal channel [73]–[76]. When the tip of the dispersed fluid goes into the main microchannel, the shearing due to continuous phase causes droplets to break up after its sufficient elongation into the channel (Figure 2.3.b). The last and least preferred geometry is co-flowing, illustrated in Figure 2.3.c. The approach employs the same physics as the flow-focusing where droplet break-off occurs when shear forces becomes dominant over the viscous forces.

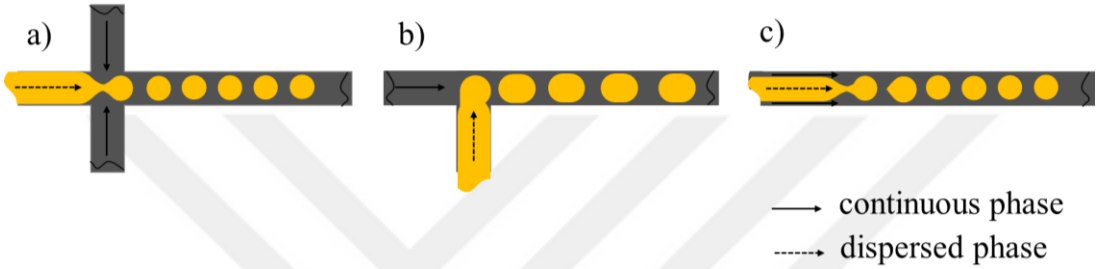


**Figure 2.3.** Droplet generation geometries. a) flow focusing, b) T-junction and c) co-flowing.

The size and shape of droplets can be finely controlled in a monodisperse manner. There is an important dimensionless number used in determining the droplet dynamics. Equation (1.1) defines this number called capillary number, $Ca$:

$$Ca = \frac{\mu v}{\sigma} \tag{1.1}$$

where $\mu$ is the viscosity of carrier phase, $v$ is the velocity of the carrier phase, and $\sigma$ is the interfacial tension between two phases. Another number closely involved in droplet generation with capillary number is dimensionless number called Weber number, $We$:

$$We = \frac{\rho v^2 D_h}{\sigma} \tag{1.2}$$

where $\rho$ is the density of aqueous fluid, $v$ is the velocity of the carrier phase, $D_h$ is the channel hydraulic diameter and $\sigma$ is the interfacial tension between two phases. Using these paired numbers, it is possible to generate monodisperse droplets on the condition that $Ca \ll 1$ and $We \ll 1$ at low flow rates.

The interfacial tension can be controlled by additional chemicals, called surfactants. The surfactants are soluble in organic and aqueous phases and useful in lowering the interfacial tension as they are collected at the interface. Therefore, they facilitate the droplet formation and stabilize them to prevent coalescence. Other than these independent variable, applied pressure and channel geometry are also effective in determining the flow field. The droplet size can be altered using applied pressure by affecting the shear stress exerted on droplets.

### 2.2.2. Droplet Formation Tests

In the analysis of the circuit model created in MATLAB, the channel model as shown in Figure 2.4 was completed to work with the channel geometries and the specified parameters for the intended application. The droplet formation system was then simulated using COMSOL Multiphysics for the desired droplet size and formation frequency (Figure 2.4.a). Different geometrical dimension variations were tried, and several oil and surfactant combinations were used to obtain the best result in terms of droplet formation and stabilization, as summarized in Table 2.1. Among them, optimum channel device dimensions were determined as 40 μm in depth, 100 μm in width with 50 μm nozzle (Figure 2.4.b) while the continuous flow fluid was selected as the Novec 7500 Fluorinated (3M) fluorinated oil with 5% Krytox FSH 157 surfactant. In this design, water containing 2% blue food dye was used to facilitate the observation of droplets as dispersed phase. (For details, please refer to M.Sc. thesis of Ali Can Atik, METU).

Note that in this design only the structures that are necessary for the formation process are used instead of the whole model presented in Section 2.1, and thus the microvalves and the observation chamber are not included in the chip design in order to facilitate the frequency and droplet size characterization. For this purpose, PDMS/glass bonded devices were fabricated using soft lithography technique, as it is visually described in Figure 2.5. Then, the fabricated devices were tested for their performances in terms of droplet formation frequency and droplet diameter.

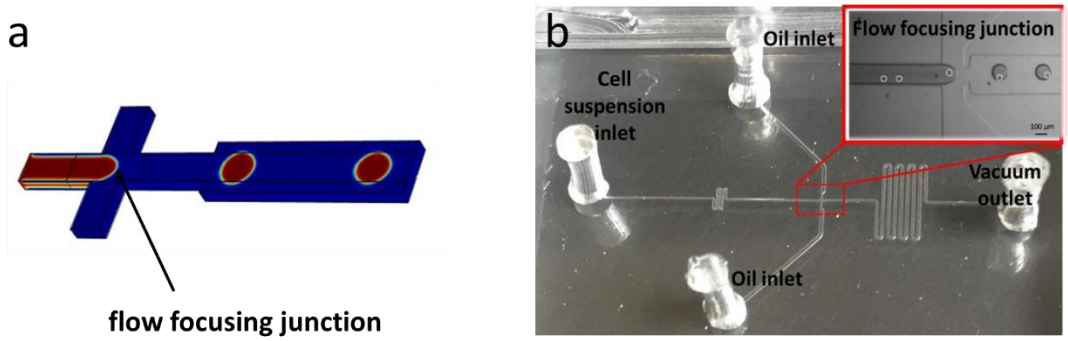


**Figure 2.4:** a) Droplet formation device fabricated using PDMS/glass bonding and b) simulation result.

**Table 2.1.** Different design dimensions for droplet formation system.

| Config. No. | Width (µm) | Depth (µm) | Nozzle (µm) |
|---|---|---|---|
| 1 | 250 | 100 | 100 |
| 2 | 200 | 100 | 100 |
| 3 | 100 | 100 | 50 |
| 4 | 100 | 100 | 50 |
| 5 | 100 | 40 | 50 |
| 6 | 50 | 25 | 25 |

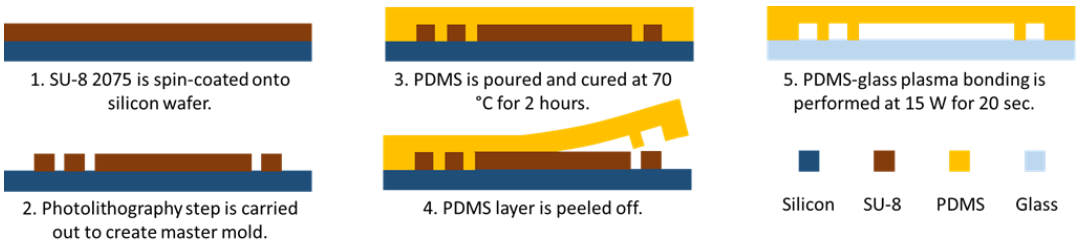


**Figure 2.5.** Fabrication flow of PDMS/glass based-droplet formation device using soft lithography and plasma bonding techniques.

The tests were performed with a microscope (Micros, Lily MCX-500). The video recordings were made using a high-speed camera (Lumenera Lt225M-SCI) and recorded 170 frames per second in the recordings. The outlet pressure in the system is provided by the precision vacuum controller (Elveflow VAC-P-600). In addition, the droplet diameter and frequencies are analyzed and computed using image processing codes generated using MATLAB (MathWorks) software.

In order to form the droplets in dripping regime, the flow rate ratio between dispersed (cell suspension) and continuous (oil) phases was determined as 1:5 with the simulations. The system was designed to operate at -10 kPa vacuum pressure at the outlet for high-frequency droplet formation. As relevant to them, the flow rates were calculated as 2.46 µl/min and 4.31 µl/min for dispersed and continuous phases, respectively. In this case, Figure 2.6 indicates the droplet formation platform containing one outlet and three inlets, one of which is used for dyed water flow and other two are for lateral oil flows in continuous manner. The droplets were formed and collected at an observation area. The droplet formation frequency was determined to be 130 Hz. When cell suspension is used instead of dyed water, the cell encapsulation can be tested. K-562 leukemia cells ($1x10^6$ cell/ml) in RPMI medium were used that are supplied by the Department of Biology, METU. Also, because cell trapping in the droplet is completely random, cell distribution is determined by the Poisson statistic. The cell capture success rate was found to be more than 30% when the cell density was $2.5x10^6$ cells/ml (Figure 2.7).

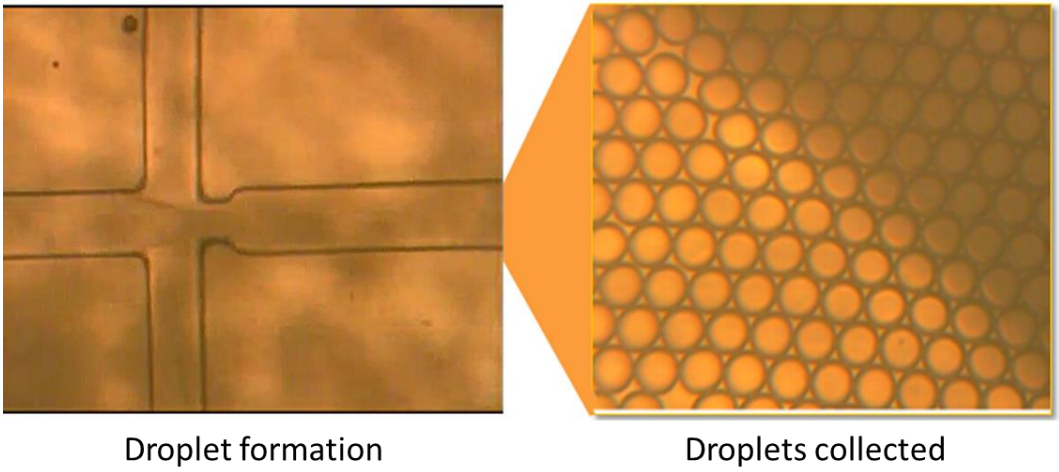


**Figure 2.6.** a) Droplet formation device components and b) collected droplets at the observation area.

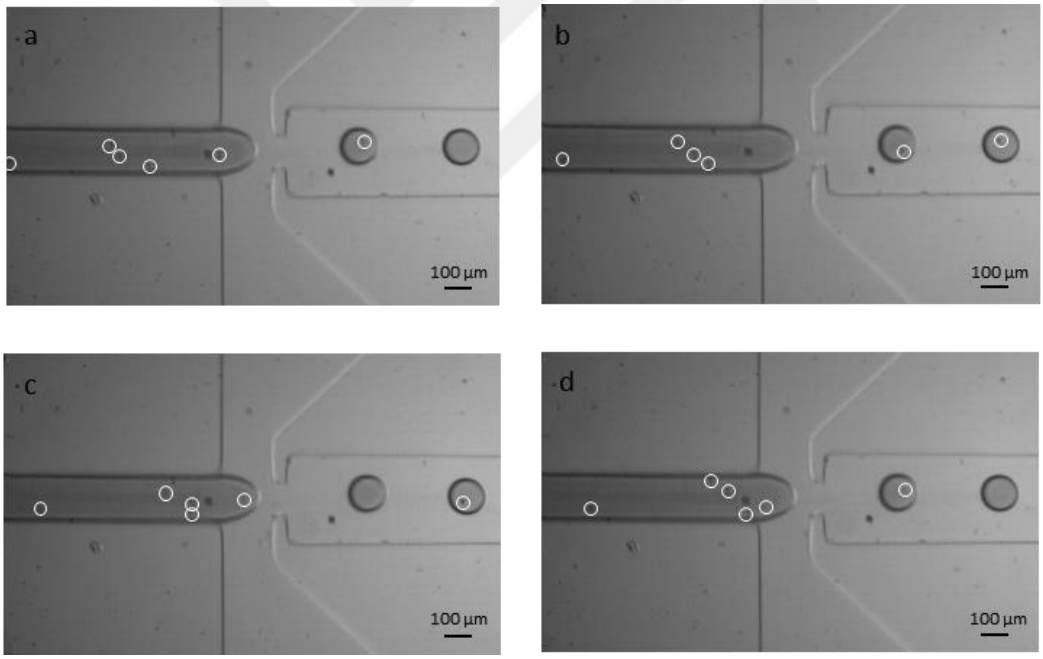


**Figure 2.7.** a) b), c) and d) Images that show the cell encapsulation process step-by-step.

## 2.3. Conclusion

This chapter explains the drug effect analysis system in detail and its working principle as the final goal. The characteristic features of the system were stressed, and an automated analysis was assembled using electrostatic microvalves. In addition, the concept which forms the basis of the drug effect analysis system was discussed: droplet microfluidics. What makes the droplet microfluidics so important for the total system is that since it is designed for cancer cell-drug interaction analysis, single cell-based methods are of vital for the cancer diagnostics due to heterogeneous behavior of the cancer cells. For this purpose, droplet formation system was first realized. According to the requirements of the ultimate platform, difference design simulations were tried, and various materials were used to obtain the best result. Therefore, the droplet formation system was established on the PDMS/glass plasma bonded device with the microchannel dimensions of 40 µm depth x 100 µm width + 50 µm nozzle using fluorinated oil (5% Krytox surfactant) as the continuous phase and blue dyed water as the dispersed phase. The results showed that droplet formation frequency for the droplets with diameter of about 100 µm are obtained at 130 Hz when the droplet formation subsystem is subjected to an output pressure of -10 kPa. Moreover, cancer cells were encapsulated in the droplets in singly manner and the rate of single cell encapsulation was improved when compared to Poisson distribution.

# CHAPTER 3

## DESIGN, FABRICATION AND TESTING OF A NORMALLY CLOSED ELECTROSTATIC MICROVALVE

In this chapter, the analytic model, operation, design, fabrication and performance of the electrostatic microvalves are presented in detail. The microvalve design originated from the model first proposed by Ender Yıldırım [65], and it was aimed to improve the model in terms of fabrication convenience, operation reliability and other factors required for the intended application. Due to complexity of numeric approaches, analytic methods are preferred in the modelling of microvalve. The analytic model basically defines the critical design parameters for the operation of a valve. Design specifications draws the boundaries of the operation of the model while describing the figure of merits. To address the specifications that the valve should meet, the role of microvalve in the intended application should be considered. A microvalve should be able to control the flow of fluid in the microfluidic system. The intended analysis system requires that the switching speed of the valve should be fast enough to allow rapid start/stop for the fluidic operation at high flow rates. Moreover, being integrable into a microfluidic system for the formation of an LOC device is another specification to implement on-chip microvalves.

In the light of above specifications, an analytical mode was first proposed to gain insight into the fundamentals of the valve. Based on the model, the design of a first-generation normally closed electrostatic microvalve was proposed. This model was fabricated using standard MEMS fabrication techniques and tested for its performance. The difficulties confronted in the first-generation model motivated for the design of

second-generation microvalve, and the related design, fabrication and characterization are given in the sequel.

### 3.1. Prediction of Pull-in Phenomena

*Parallel-Plate Approach:*

Actuation mechanism description of the electrostatic microvalve firstly requires a model to be developed. The 1-D lumped model can be derived from a simple approach benefiting from the coupling between electrical and mechanical domains: parallel-plate capacitor approach (Figure 3.1). In this model, there are two parallel plates separated by a distance, *d*, one of which is movable towards the fixed one in vertical direction. Considering the mass-spring model, the movable plate has an imaginary linear spring with a spring constant, *k*, which provides the restoring force on the moving electrode. The deflection of movable element is due to electrostatic forces exerted by an applied potential to the plates. Starting from this point of view, electrostatic microvalve can be model as a parallel-plate actuator in the simplest form. The valve can operate by the deformation of diaphragm attached to the movable plate as the plate is lifted/collapsed. The vertical movement of the suspended plate due to the electric field creates a gap varying capacitance with a single-degree of freedom.

For this simplest model, the resultant force is composed of electrostatic and restoring forces. In equilibrium condition, the net forces are equal to zero resulting from mechanical restoring forces of being equal to electrical forces.

$$F_{el} = m\ddot{x} + b\dot{x} + kx \tag{3.1}$$

where *k* is the spring constant. To simplify the model, the damping effects, fringing fields, and residual and axial stresses are neglected. In order to find the electrostatic force between these plates, the derivative of potential energy is taken with respect to the distance. The potential energy of the capacitor is a well-known formula, given in Equation (3.2).

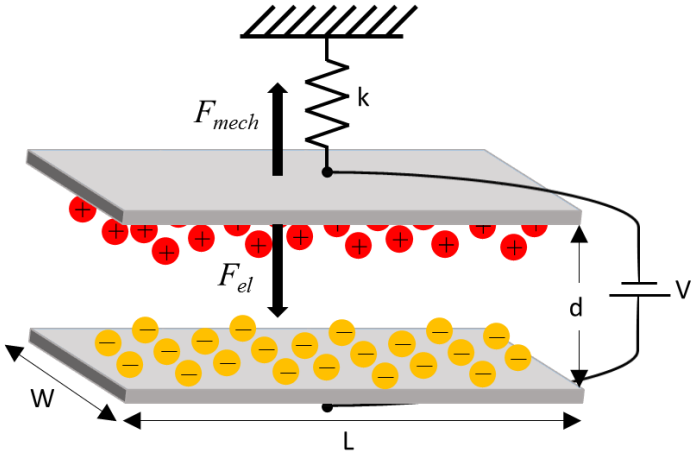


**Figure 3.1.** Parallel-plate approach for representing the microvalve fundamentals.

$$E_{pot} = \frac{1}{2}CV^2 = \frac{1}{2}\varepsilon\frac{A}{d}V^2 \tag{3.2}$$

$$F_{el} = \frac{\partial E_{pot}}{\partial d} = \frac{1}{2}\varepsilon\frac{A}{d^2}V^2 \tag{23.3}$$

where $\varepsilon$ is the dielectric constant of material, $A$ is the area of the plate, and $V$ is the applied potential. Then, by rewriting Equation (3.1) by ignoring the damping effect, it becomes

$$kx = \frac{1}{2}\varepsilon\frac{A}{(d-x)^2}V^2 \tag{3.4}$$

$$F_{net} = \frac{\varepsilon AV^2}{2(d-x)^2} - kx \tag{3.5}$$

The equilibrium of forces can be preserved until a certain voltage beyond which the diaphragm collapses. This phenomenon is known as "*pull-in instability*". Pull-in occurs due to non-linearly increasing electrostatic force with decreasing gap while the mechanical restoring force changes linearly with respect to the gap. The voltage level required to reach the instability is called *"pull-in voltage"* and the displacement point is known as *"pull-in position"*. The phenomenon of pull-in instability should be considered for the operation of electrostatic devices. Although this is an undesirable

effect for certain applications such as capacitive pressure sensors and microphones, there are studies using the instability to good account in sensors as the switching mechanism due to its intrinsic property of electrostatically actuated MEMS devices [77].

In 1967, the theoretical formulations of pull-in instability was pioneered by Nathanson *et al.* [78]. Based on their work, the critical deflection and pull-in voltage can be derived as follows:

When the system is at equilibrium, the net force, $F_{net}$, is zero. Moreover, the tangency of the electrical and mechanical restoring forces is equal to each other at the same point where pull-in occurs. The variation in net force can be found by taking the derivative of net force with respect to the displacement.

$$\left.\frac{\partial F_{net}}{\partial x}\right|_V = \frac{\varepsilon A V^2}{(d-x)^3} - k \tag{3.6}$$

At point where the equilibrium is no longer preserved, Equation (3.6) can be solved for two boundary conditions which are $\partial F_{net}/\partial x = 0$ and $F_{net} = 0$ by the using the stiffness of the circular diaphragm. Then, the value of displacement found is called pull-in displacement, $x_{pi}$.

$$x_{pi} = \frac{1}{3} d \tag{3.7}$$

Equation (3.7) states that the displacement range of top plate is limited to one-third of the initial gap caused by pull-in instability, and it is independent of bias voltage applied. Now that the critical displacement is known, pull-in voltage, $V_{pi}$ can readily be found by substituting Equation (3.7) into Equation (3.5):

$$V_{pi} = \sqrt{\frac{8kd^3}{27\varepsilon A}} \tag{3.8}$$

In order to better understand the pull-in phenomenon, one can graphically examine the gap vs. voltage [79]. Knowing that $k = \varepsilon AV^2/2x(d-x)^2$, Equation (3.8) can rewritten by normalizing the values of displacement and voltage:

$$v = \frac{V}{V_{pi}} \tag{3.9a}$$

$$ב = \frac{x}{d} \tag{3.9b}$$

$$\frac{4}{27}\frac{v^2}{(1-ב)^2} = ב \tag{3.9c}$$

Figure 3.2 indicates that the stability is preserved at a point and beyond this value collapse to from one-third of the initial gap to zero gap occurs at $V = V_{pi}$.

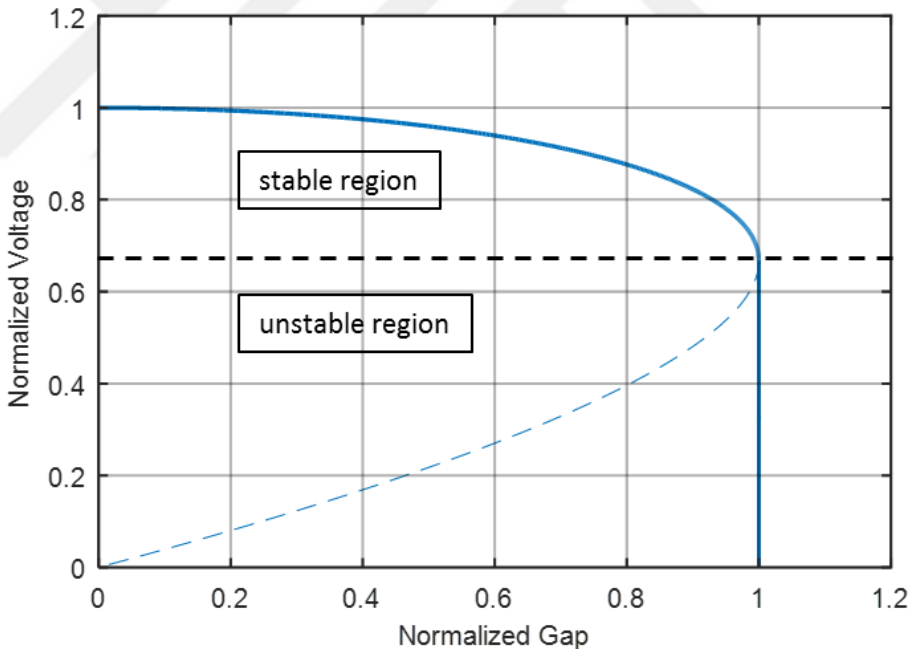


**Figure 3.2.** Normalized graph of gap vs. voltage for electrostatic actuator. The change in the gap is given in response to applied voltage, which indicates that pull-in occurs at the distance one-third of the initial gap [79].

The accurate prediction of pull-in is very important for the operation of electrostatic devices such as capacitive micromachined ultrasonic transducers (CMUTs) or MEMS switches. The 1-D lumped model developed for pull-in effect predicts that the pull-in occurs at a position one-third of the gap. However, this model approximates the behavior of the electrostatic actuator and does not include the plate deformation and diaphragm stretching by considering that the plates are rigid. In fact, the actual valve design has parallel circular plates that are clamped at the outer edges and the top plate is continuously deformed during the operation. Therefore, for a clamped and deformable circular plate model, a more accurate prediction method should be used. Many studies have been relatedly made for the comprehensive pull-in phenomena. The researchers use analytical modeling of membranes or finite element model analysis for this purpose.

*Continuous Reduced-Order Model:*

For more accurate prediction of pull-in, the residual stress due to edge clamping and nonlinear electrostatic force should be considered by an improved model. Vogl *et al.* [80] proposed a continuous reduced-order model to investigate the dynamic behavior of electrostatic devices. They established the governing equations and solve them by accounting for the residual stress and geometric nonlinear hardening using a well-known method. In this manner, Liao *et al.* [81] also investigated the pull-in for clamped circular plates relying on the same model. They analytically analyzed the model for both static and dynamic pull-in effects.

The parallel-plate approach introduced for modeling the electrostatic microvalve is an approach for the actuation mechanism and pull-in phenomena. The actual valve design should analytically be modelled. Figure 3.3 indicates the actual design and Figure 3.4 illustrates the collapsed microvalve for top and cross-sectional views. It has a circular membrane clamped at the outer edges and the intensity of the load is uniformly distributed.

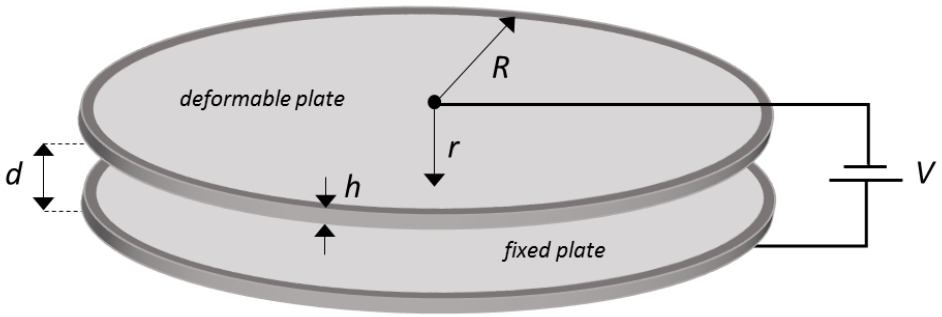


**Figure 3.3.** Schematic of an electrostatically actuated parallel circular plate model fully clamped at the periphery.

To formulate the model for a circular deformable plate, the governing equation of motion should be established. Based on the work of Vogl *et al.* [80], the equation of motion can be expressed for axisymmetric motion:

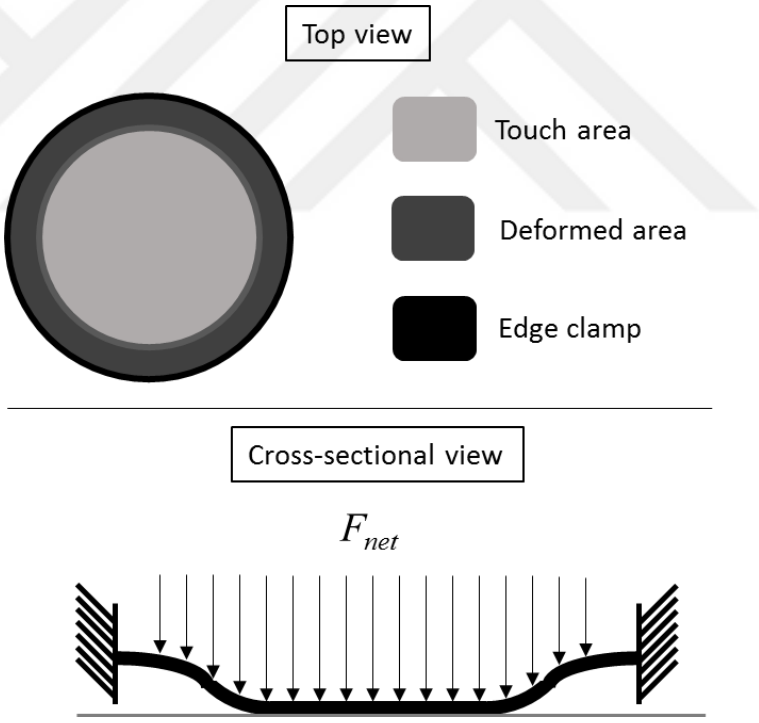


**Figure 3.4.** Top and cross-sectional views of circular diaphragm of microvalve design. It is subjected to a uniformly distributed electrostatic load and deflection occurs.

$$\rho h\frac{\partial^2\widehat{w}}{\partial\hat{t}^2}+2\hat{c}\frac{\partial\widehat{w}}{\partial\hat{t}}+D\widehat{\nabla}^4\widehat{w}$$
$$=\frac{1}{\hat{r}}\frac{\partial}{\partial\hat{r}}\left(\frac{\partial\widehat{w}}{\partial\hat{r}}\frac{\partial\widehat{\phi}}{\partial\hat{r}}\right)+\frac{\hat{\tau}h}{\hat{r}}\frac{\partial}{\partial\hat{r}}\left(\hat{r}\frac{\partial\widehat{w}}{\partial\hat{r}}\right)+\frac{\varepsilon\widehat{V}^2(\hat{t})}{2(d-\widehat{w})^2} \quad (3.10)$$

and

$$\widehat{\nabla}^4\widehat{\phi}=-\frac{Eh}{\hat{r}}\frac{\partial^2\widehat{w}}{\partial\hat{r}^2}\frac{\partial\widehat{w}}{\partial\hat{r}} \quad (3.11)$$

In Equation (3.10), $\rho$ is the plate material density, $h$ is the plate thickness, $\widehat{w}(\hat{r},\hat{t})$ is the plate transverse deflection, $\hat{c}$ denotes the viscous damping coefficient for the material, $D=Eh^3/12(1-\upsilon^2)$ is the bending rigidity with $E$ being the Young's modulus and $\upsilon$ being the Poisson's ratio, $\hat{r}$ is the radial position, $\hat{\tau}$ is the uniform residual biaxial plane stress, $\widehat{V}(t)$ is the DC voltage, $\varepsilon$ is the permittivity of the material between the plates, $d$ is the gap between the plates, and $\hat{t}$ indicates the time at which voltage is applied. The last term in the equation is the electrostatic force acting on the deformable plate. $\widehat{\phi}(\hat{r},\hat{t})$ is the stress function given in Equation (3.11).

For the case of clamped at the outer edges, the boundary conditions with only transverse displacement can be written as

$$\widehat{w}(R,\hat{t})=0,\qquad \frac{\partial\widehat{w}(R,\hat{t})}{\partial\hat{r}}=0,\ \text{and}\quad \widehat{w}(0,\hat{t})\ \text{is bounded,} \quad (3.12)$$

$$\frac{\partial^2\widehat{\phi}(R,\hat{t})}{\partial\hat{r}^2}-\frac{V}{R}\frac{\partial\widehat{\phi}(R,\hat{t})}{\partial\hat{r}}=0,\ \text{and}\quad \widehat{\phi}(0,\hat{t})\ \text{is bounded.} \quad (3.13)$$

Equation (3.12) denotes that the circular top plate is clamped at the outer edges whereas the Equation (3.13) is for the non-stressed condition. Note that the cap (ˆ) in Equation (3.10)-(3.13) denotes the dimensional variables. For analytical convenience, the equations can be non-dimensionalized by first establishing the below set of equations:

$$\widehat{w} = dw\,, \qquad \hat{r} = Rr\,, \qquad \hat{t} = R^2\sqrt{\frac{\rho h}{D}}\,t\,, \tag{3.14a}$$

$$\hat{V}^2(t) = \frac{2Dd^3}{\varepsilon R^4}V^2(t), \qquad \hat{c} = \frac{\sqrt{D\rho h}}{R^2}\,c\,, \qquad \hat{\tau} = \frac{D}{hR^2}\,\tau, \tag{3.14b}$$

$$\beta = 12\,\frac{(1-V^2)d^2}{h^2}, \qquad \text{and} \qquad \widehat{\phi} = Ehd^2\phi \tag{3.14c}$$

Having inserted the set of equations into Equation (3.10) and (3.11), the non-dimensional governing equation of motion for the dynamic behavior of the deformable plate becomes

$$\frac{\partial^2 w}{\partial t^2} + 2c\frac{\partial w}{\partial t} + \nabla^4 w = \tau\frac{1}{r}\frac{\partial}{\partial r}\left(r\frac{\partial w}{\partial r}\right) + \frac{\beta}{r}\frac{\partial}{\partial r}\left(\frac{\partial w}{\partial r}\frac{\partial \phi}{\partial r}\right) + \frac{V^2(t)}{(1-w)^2} \tag{3.15}$$

$$\nabla^4\phi = -\frac{1}{r}\frac{\partial^2 w}{\partial r^2}\frac{\partial w}{\partial r} \tag{3.16}$$

Then, the boundary conditions in non-dimensional form are written as follows:

$$w(1,t) = 0, \qquad \frac{\partial w(1,t)}{\partial \hat{r}} = 0, \quad \text{and} \quad w(0,t) \text{ is bounded,} \tag{3.17}$$

$$\frac{\partial^2 \phi(1,t)}{\partial r^2} - V\frac{\partial \phi(1,t)}{\partial r} = 0, \quad \text{and} \quad \phi(0,t) \text{ is bounded.} \tag{3.18}$$

The derived non-dimensional equation of motion in Equation (3.15) is a partial differential equation (PDE) with boundary conditions. Since the numerical solution for PDE is difficult to establish, a method of approximation is necessary to simplify the analysis. In [80], Vogl *et al*. used the Galerkin method by decoupling the PDEs to obtain the discrete modal ordinary differential equations (ODEs). It is a powerful tool used to approximate the solution of a complex differential equations by converting the strong formulations into weak formulations. Using the Galerkin method, the equation of motions can be reduced to discrete ODEs by stating an initial approximation regarding the deflection, $w(r,t)$, and stress, $\phi(r,t)$, functions as follows:

$$w(r,t) = \sum_{m=1}^{N} \eta_m(t)\phi_m(r) \tag{3.19}$$

$$\phi(r,t) = \sum_{m,n=1}^{N} \eta_m(t)\,\eta_n(t)\psi_{mn}(r) \tag{3.20}$$

where $N$ is the number of modes chosen, $\phi_m(r)$ is the $m$th shape function, $\eta_m(t)$ is the $m$th generalized coordinate for the function $\phi_m(r)$, and $\psi_{mn}(r)$ is the unknown asymmetric function to be determined in the analysis all of which satisfy the related boundary conditions. By using Equation (3.19) and (3.20), the solution procedure of Equations (3.15)-(3.18) can be followed. At this point, Liao *et al.* [81], based on the reduced-order model, made some thorough calculations, and obtained the coupled set of modal ODEs for predicting the pull-in effect, as follows:

$$M\ddot{w} + C\dot{w} + Kw = f_e \qquad \text{for } 1 \le m \le N \tag{3.21}$$

where

$$m_m = \int_0^1 \phi_m^2\, dr \tag{3.22a}$$

$$c_m = 2c \int_0^1 \phi_m^2\, dr \tag{3.22b}$$

$$k_m = \left[\left(\frac{\partial^2}{\partial r^2} + \frac{1}{r}\frac{\partial}{\partial r}\right)\left(\frac{\partial^2 \phi_m}{\partial r^2} + \frac{1}{r}\frac{\partial \phi_m}{\partial r}\right) - \tau\frac{1}{r}\frac{\partial}{\partial r}\left(r\frac{\partial \phi_m}{\partial r}\right)\right] \tag{3.22c}$$

and

$$f_{e,m} = \alpha \int_0^1 F_e \phi_m\, dr \qquad \text{where} \qquad \alpha = \frac{\varepsilon R^4}{Dd^3} \tag{3.23}$$

In Equation (3.21), the only term that should be evaluated is the electrostatic force, $f_e$, since the remaining terms are constant matrices. One way to evaluate $f_e$, is using a finite-order Taylor series expansion. For this purpose, the first-mode of the decoupled

equation, given in (3.23), is used since the first-mode approximation is sufficient to predict the central deflection of the plate [81], [82]. By neglecting the damping effect, the equilibrium condition for the forces can be written as

$$f_{e,1} = f_{mech,1} \tag{3.24}$$

and

$$f_{mech,1} = k_1 w_1 \tag{3.25}$$

where $f_{e,1}$ denotes the first-mode of the electrostatic force while $f_{mech,1}$ is that of mechanical restoring force. $w_1$ is the first-mode deflection of the plate. Then, the tangency of two forces with respect to the first-mode deflection can be established based on the basis of the boundary condition, as in Equation (3.26).

$$\frac{\partial f_{e,1}}{\partial w_1} = \frac{\partial f_{mech,1}}{\partial w_1} \tag{3.26}$$

Solving Equation (3.24) and (3.26) yields

$$f_{mech,1} \frac{\partial f_{el,1}}{\partial w_1} = f_{e,1} \frac{\partial f_{mech,1}}{\partial w_1} \tag{3.27}$$

Equation (3.27) is solved for $w_1$ using Taylor series expansion to the fifth order. Thus,

$$\begin{aligned} & f_{e,1} \frac{\partial f_{mech,1}}{\partial w_1} - f_{mech,1} \frac{\partial f_{e,1}}{\partial w_1} \\ & \cong \alpha V^2 C_1^2 (441.759 + 34.610\hat{\tau})[-0.257 + 0.487 w_1^2 \\ & - 1.132 w_1^3 + 1.912 w_1^4 - 2.806 w_1^5] = 0 \end{aligned} \tag{3.28}$$

The expression in the brackets of the above equation is set to zero to obtain the normalized value of pull-in position. Finally, the normalized pull-in position with respect to the gap is determined as

$$w_{1,pi} \approx 0.415 \tag{3.29}$$

Knowing now that the pull-in position, the static pull-in voltage can be found:

$$V_{s,pi} = \frac{1.325\sqrt{16.777 + 1.314\hat{\tau}}}{\sqrt{a}} \tag{3.30}$$

Making Equation (3.30) dimensional yields

$$V_{s,pi} = \frac{1.325\sqrt{d^3(16.777D + 1.314hR^2\tau)}}{R^2\sqrt{\varepsilon}} \tag{3.31}$$

The pull-in position and voltage found above is valid for the case when the voltage is incrementally applied. However, the actual scenario for the system operation requires the instantaneous voltage application, When the voltage applied to the plates is progressively increased until the voltage at which pull-in occurs, the event called as '*static pull-in*' occurs. The incremental voltage changes the initial deflection and decreases the gap. Therefore, the increase in the nonlinearly behaving electrostatic force causes the pull-in voltage increases. On the other hand, the dynamic actuation is achieved sudden voltage application and results in the overshoot the equilibrium position, which corresponds to '*dynamic pull-in*'. In this case, the critical voltage is reduced whereas the critical displacement where the collapse of the plate occurs becomes larger. According to Nielson *et al.* [83] the ratio of dynamic pull-in and static pull-in is

$$\frac{V_{d,pi}}{V_{s,pi}} \approx 0.911 \tag{3.32}$$

Therefore, by accurately predicting the static pull-in voltage, the dynamic counterpart can be easily found.

*Finite Element Analysis (FEA):*

The continuous model well predicts the pull-in phenomena when compared to 1-D lumped model. In addition, another method for precise prediction of the pull-in voltage/position also validating the theoretical model is the finite element analysis (FEA) method. COMSOL Multiphysics was used as the software to model the problem. The physics utilized was electromechanical and 2-D axisymmetric model was selected as the space dimension to decrease the time of simulation. The mesh was arranged to be mapped with different distributions to five different domains, D1-D5 (Figure 3.5.a). The simulation was performed by parametrically sweeping the deflection, *w*, between the values 0 µm and 5µm with 0.01 µm-displacement intervals. As a result, the displacement is observed (Figure 3.5.b), and pull-in simulation indicates that the critical displacement value is 2 µm from the bottom, i.e., 3/5 of the gap, and the pull-in voltage is found to be 37.7 V (Figure 3.5.c).

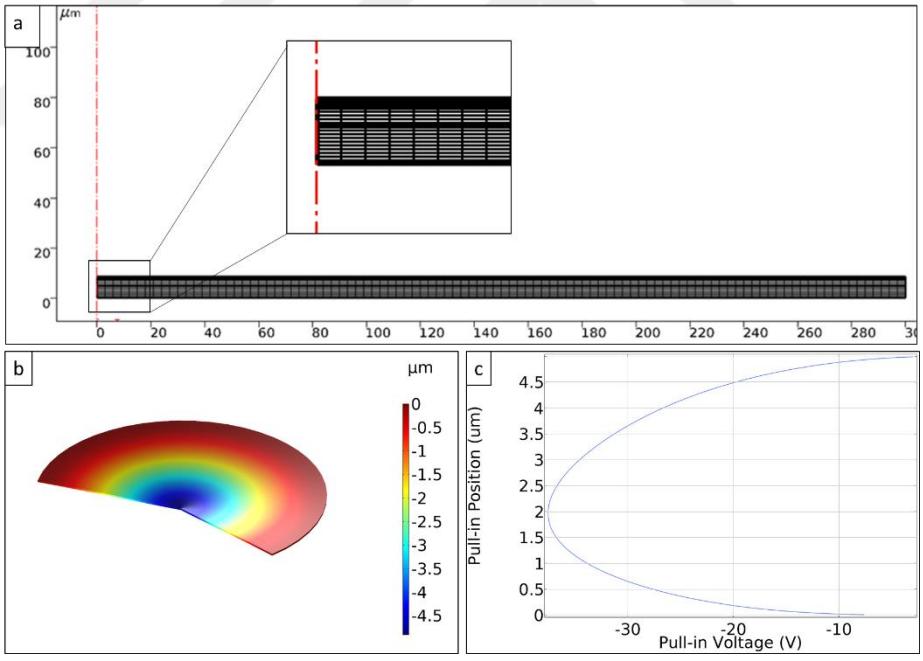


**Figure 3.5.** a) Mesh configuration of the 2-D axisymmetric microvalve model simulated in COMSOL, b) simulation result for deflection after pull-in voltage has been exceed, and c) the graph of pull-in position vs. pull-in voltage for electrostatic actuation, indicating that pull-in occurs at a distance two-third of the initial gap and a voltage about 37.7 V.

In order to evaluate the mesh size dependency of the pull-in voltage and position values, many simulations were made. By varying the degrees of freedom for D1-D5, the graph in Figure 3.6 is obtained, which shows the change in the voltage and position with respect to the number of degrees of freedom. According to the results, it can be concluded that the pull-in position value does not change at all and reaches 2 µm whereas the voltage varies at the level of tenths after the decimal point between 37.505 V and 37.715 V.

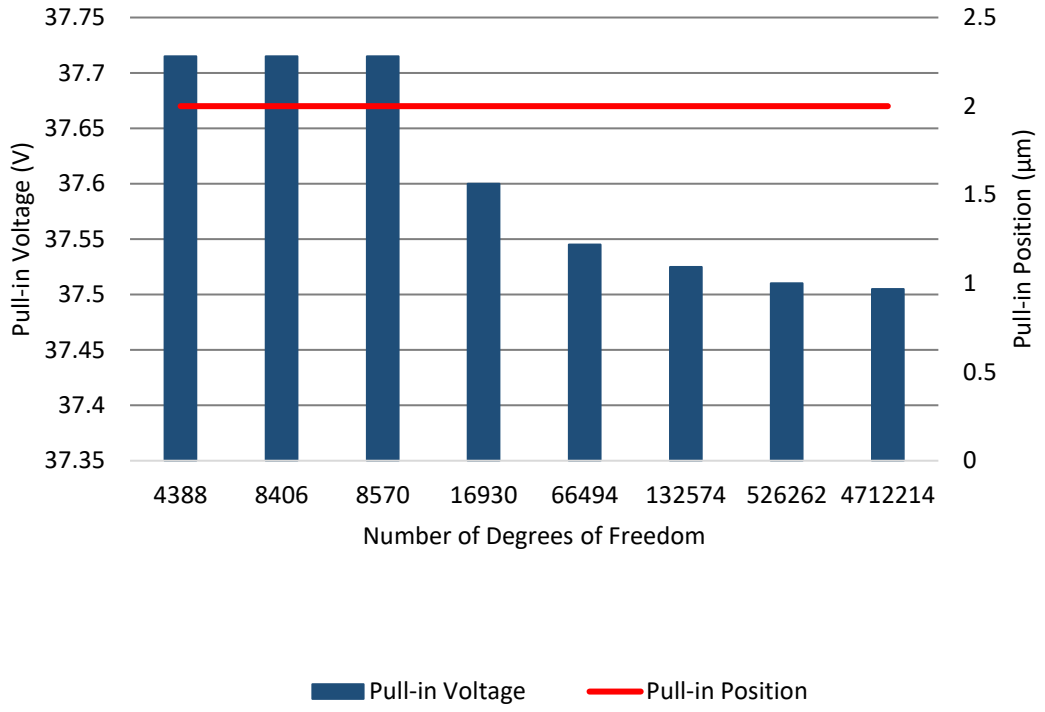


**Figure 3.6.** The graph of mesh size dependency of the pull-in voltage and position. The pull-in position remains constant as 2 µm and the voltage slightly changes between 37.505 V and 37.715 V.

## 3.2. Operation of the Microvalve

Now that the analytical model of the microvalve was explained, the details of the operation of microvalves are considered. As can be seen in Figure 3.7, the normal operating mode of the microvalve is designed to block the fluid flow through the microchannel by means of a flat rectangular wall entirely covering the cross-sectional

area of the channel. Moreover, the design offers a distinct advantage that is absent in most of the electrostatic microvalves proposed in the literature. The electrolysis of the working fluid is avoided by depositing a thin insulating parylene layer on top of the top electrode so that the electrical properties of working fluid has no impact on the actuation potential. In this case, only air within the actuation chamber acts as the dielectric material.

In the open state of the microvalve, the input of the actuator is the voltage and the resultant output is the vertical movement of the top electrode and thus that of circular diaphragm. Actually, the operation of the microvalve is controlled by two basic variables: the pressure exerted on the valve and the electrical potential applied to the valve. The pressure on the valve can be readily determined by means of simulations. Therefore, the electric potential remains the only variable to be controlled for the operation of the valve.

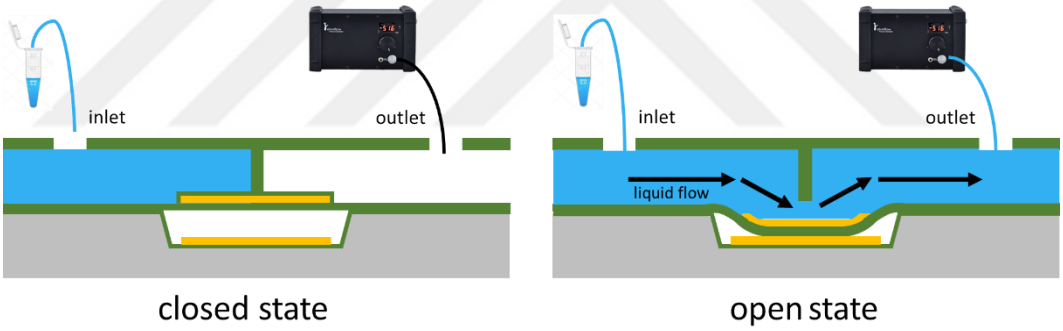


**Figure 3.7.** Working condition of the designed normally closed microvalve. In closed state (above), the liquid flow is prevented by the wall completely covering the cross-sectional area of the microchannel. When a certain voltage is applied, diaphragm collapses on the bottom electrode and flow is enabled in open state (below).

## 3.3. Design and Characterization of the Microvalve

### 3.3.1. First-Generation Design

#### 3.3.1.1. Design

Figure 3.8 illustrates the schematic of a parylene-based and normally closed electrostatic microvalve. It has a circular parylene diaphragm clamped at the outer edges. The bottom electrode is located inside the actuation chamber whereas the top electrode is placed on top of the diaphragm so that the diaphragm can be deflected towards the fixed electrode. When deflected, the compressed air inside the chamber is vented through the outflow connection channels.

The design dimensions were selected according to the analyses made by Yıldırım *et al.* [65]. In this thesis, the valve radius, diaphragm thickness and actuation chamber depth were analytically selected based on Yıldırım's study where different microvalves with different diameters of 150 μm, 250 μm, 350 μm and 450 μm were used and stress analysis of the diaphragm was performed for the elasticity tests to determine by defining an aggregate target function (AOF) to minimize their values. As indicated in Figure 3.8, two different chamber radii of 300 μm and 410 μm were used whereas other dimensions kept the same for the microvalves.

#### 3.3.1.2. MEMS Fabrication

The layout of electrostatic microvalve drawn using layout editing software, Cadence, is given in Figure 3.9. The fabrication process of a normally closed electrostatic microvalve contains six main steps in which different processes are required, as shown in Figure 3.10.

**Table 3.1.** Design parameters and mechanical properties of the materials used in the design are shown together with the first-generation design figure.

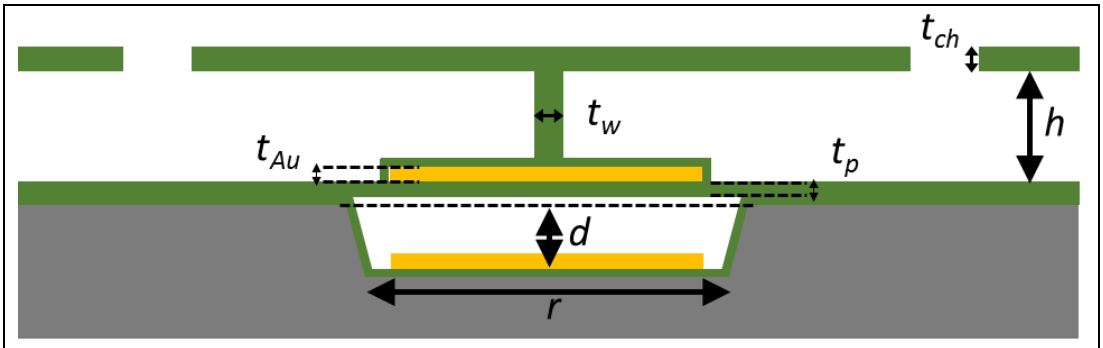


**Figure 3.8.** Design of a first-generation electrostatic microvalve and important parameters.

| **Design Parameter** | **Dimension** |
|---|---|
| Actuation chamber depth ($d$) | 5.5 µm |
| Actuation chamber radius ($R$) | 300 µm, 410 µm |
| Diaphragm thickness ($t_p$) | 2.5 µm |
| Channel height ($h$) | 40 µm |
| Parylene channel thickness ($t_p$) | 10 µm |
| **Mechanical Properties** | **Value** |
| Dielectric permittivity of parylene ($\varepsilon_p$) | 3.15 |
| Elastic modulus of parylene ($E_p$) | 3.2 GPa |
| Poisson's ratio of parylene ($\upsilon_p$) | 0.33 |
| Elastic modulus of gold ($E_{Au}$) | 77.2 GPa |
| Poisson's ratio of gold ($\upsilon_{Au}$) | 0.42 |

The first step includes the formation of actuation chamber and air vents. The circular actuation chamber that enables the gap for membrane to collapse and air vent channels that vents the air inside the chamber after the collapse are created within the silicon substrate with bulk micromachining. The depth of these structures is determined as 5 µm so as to provide a sufficient distance with microvalve diaphragm to fall down and

allow the fluid flow. The diameter of the chamber is 600 µm. Initially, the structure regions are defined with photolithography process. There is a requisite for inclined side walls to have continuous electrical connection between the contact pad on the wafer level and bottom electrode inside the actuation chamber, which is about 5 µm lower than wafer surface. Therefore, an image reversal photoresist, AZ 5214, is used at this step in order to utilize the inclined surface profile of negative resist at the side walls. Later, deep reactive ion etching (DRIE) process is realized. After etching, all polymer layers are removed with oxygen plasma. A parylene layer of 0.5 µm is deposited to electrically isolate the wafer from electrodes since the silicon substrate itself is a conducting material. Silane A-174 must be used to increase its adhesion while depositing the parylene layer, which will facilitate other parylene deposition processes.

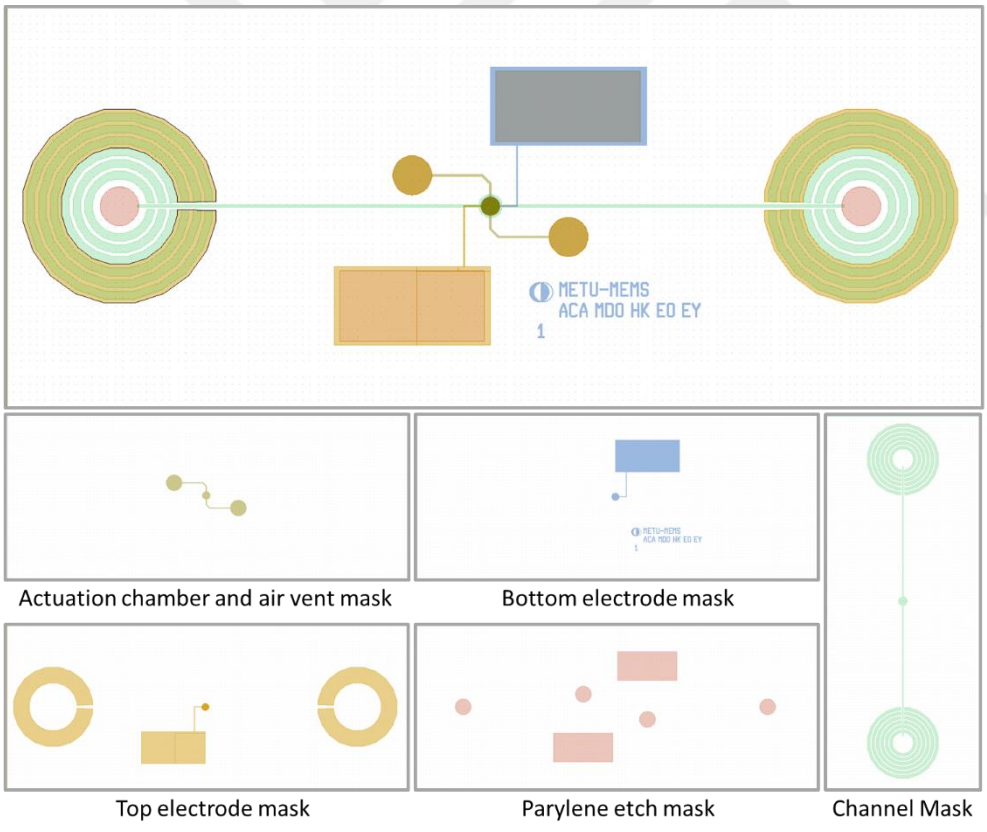


**Figure 3.9.** Overview of the first-generation mask design of the electrostatic microvalves. Each mask is separately shown.

At the second main step, bottom electrodes are formed using AJA/Bestec sputter. First, a titanium (Ti) layer of 20 nm is sputtered to increase the adhesion of gold (Au) to the substrate and then Au layer of 200 nm is coated. The locations of electrodes, contact lines and pads are defined with photolithography step. After applying plasma process, called descum, for surface cleaning, wet etch is performed to etch Au and Ti layers, respectively. Having completed the etching, sacrificial resist layer is removed by immersing the wafer in acetone. The bottom electrode should fit in the chambers with a 50 µm gap around them (from the chamber side walls). Since the diameter of chambers is determined as 600 µm, that of bottom electrode should be 500 µm in circular shape. The contact lines have a width of 30 µm while the pads are rectangular with dimensions of 2000 µm x 3000 µm.

Filling the actuation chamber and air vent channels is the third main step of the fabrication. They are filled with sacrificial photoresist. This step is quite critical since the top surface level of the coated resist should be in alignment with the wafer surface for a smooth parylene membrane formation. Then, parylene layer of 2.5 µm is deposited to create the membrane. The value of membrane thickness was selected since the working reliability was proven by Yıldırım [65]. At this step, silane should not be used during the deposition since it reacts with the PR layer underneath the parylene and swelling occurs.

The fourth main steps is top electrode metallization. The process recipe is the same as that of bottom electrode except the thickness of Ti and Au layers are 10 nm and 100 nm, respectively. Top electrode has a spiral shape that covers the circle with a diameter of 500 µm. Since the top electrodes reside on parylene diaphragm, its collapse into chamber should be facilitated using spirality. Then, a thin silane-free parylene layer is deposited onto the electrode. Since the liquids flow above the top electrode, this layer prevents the liquids from electrolysis.

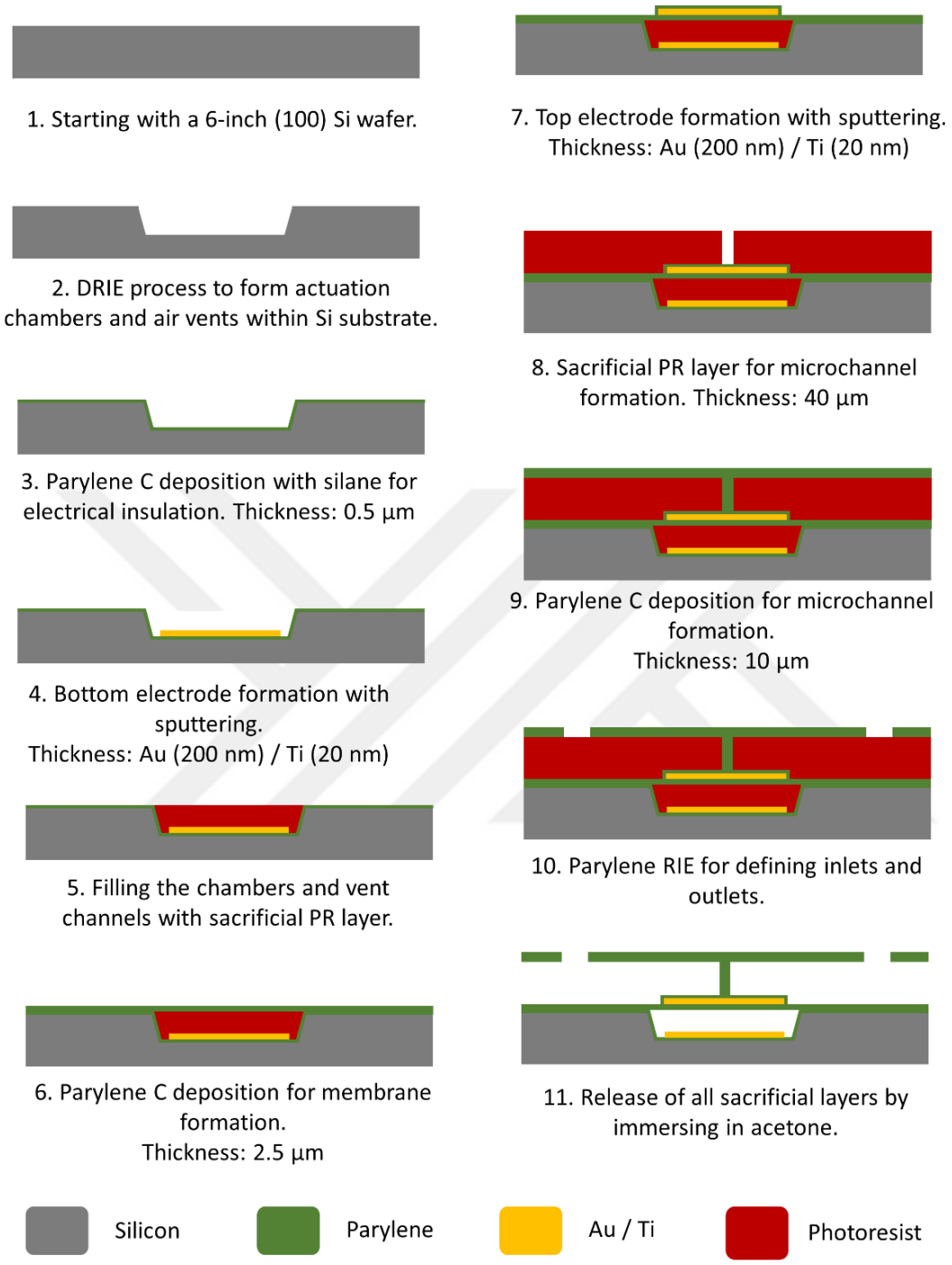


**Figure 3.10.** Fabrication flow of the first-generation normally closed electrostatic microvalve.

Microchannel formation is the fifth step in the fabrication. The channels are formed first by carrying out photolithography step. Since the required thickness of the channels is 40 µm, thick photoresist type should be used. AZ 40 XT is utilized with special care. Next, 10 µm-parylene layer covers the PR layer to form the channel. Again, silane should not be used during the deposition.

At the last step, the inlets and outlets are defined. Photolithography is performed to create masking layer to etch the parylene layer. As the thickest parylene layer on top of a contact pad is 13.5 µm, the etching is done with reactive ion etching (RIE) step accordingly to remove all parylene on the top. Then, the wafer is diced and immersed into acetone for 5-8 days. After IPA/methanol treatment, the dies are dried using hotplate at 70 °C and the fabrication process is completed. An image of the fabricated first-generation electrostatic microvalve is provided in Figure 3.11.

#### 3.3.1.3. Optimization of Fabrication Steps

As already mentioned, the first design of a normally closed electrostatic microvalves were made by Ender Yıldırım [65]. While the performance of microvalves was highly satisfactory, various problems and difficulties have arisen in the fabrication and testing stages. Theoretical solutions have been proposed for previously encountered problems, and there have been some difficulties to be optimized in the final fabrication process. All previous and subsequent challenges are below explained in detail and solution recommendations are introduced for each.

*i. Removal of sacrificial photoresist in actuation chamber:*

**Problem:** The main difficulty of first fabrication was the removal of sacrificial PR used in the actuation chamber. After the sacrificial PR layer was filled into the chamber, two layers of parylene were first deposited for the valve membrane and then for the bottom of the channel. As the next step, very thick PR layer was coated to form

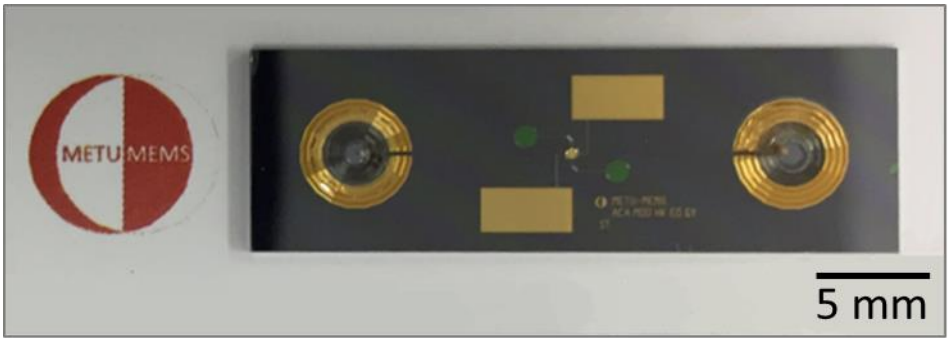


**Figure 3.11.** Image of the fabricated first-generation electrostatic microvalve on silicon wafer.

the microchannel, and then baked, which caused it to be baked for the second time. Thereafter, release process is normally realized by immersing the device in acetone for 2-3 days. However, the removal of PR in the actuation chamber was hardly realized due to excessive baking. In order to completely remove the resist, the device was kept in acetone for days. Holding the device for a long time in acetone, even though the resist was removed, resulted in parylene membrane to swell.

**Solution:** The bake process of PR inside the chamber was optimized not to pose a problem in the release process, based on the studies related to the effect of organic and inorganic solvents on parylene reported by Koydemir *et al.* [84], [85]. Each test device including a microchannel, an inlet and an outlet were fabricated using MEMS technology, as indicated in Figure 3.12. The PR used was SPR 220-7, which was the same type used in the fabrication.

The PR layer coated for microchannel was first baked at 95 °C for 6 hours, which was at 110 °C for 3 hours in the previous process. Then, 5 µm-parylene layer was deposited on the resist. At last, metallization of Au/Ti (50 nm/5nm) was carried out. These three steps are the same as in the actual fabrication for filling the chamber, forming the microchannel and sputtering the valve electrode. Figure 3.13 shows the results related to baking optimization. It was observed that there was no outgassing due to PR, and the parylene layer did not swell.

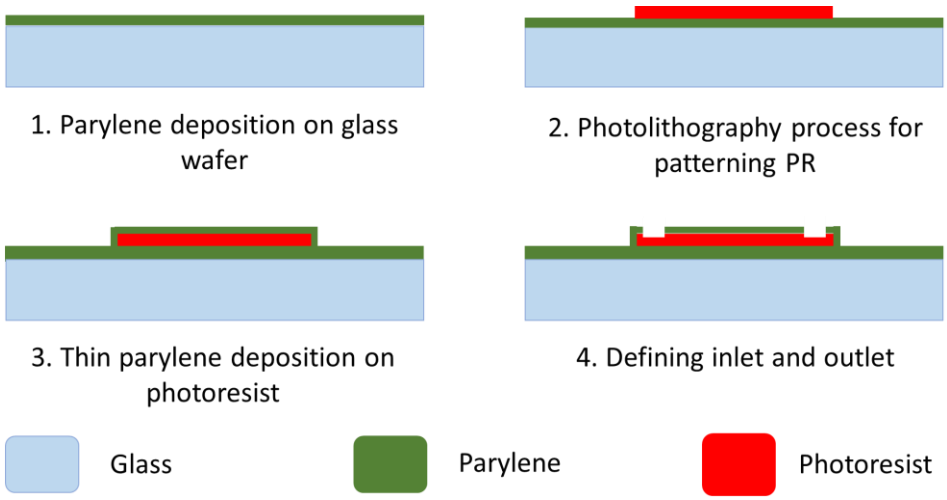


**Figure 3.12.** The process flow of fabrication done for the optimization of baking and removal of sacrificial PR layer.

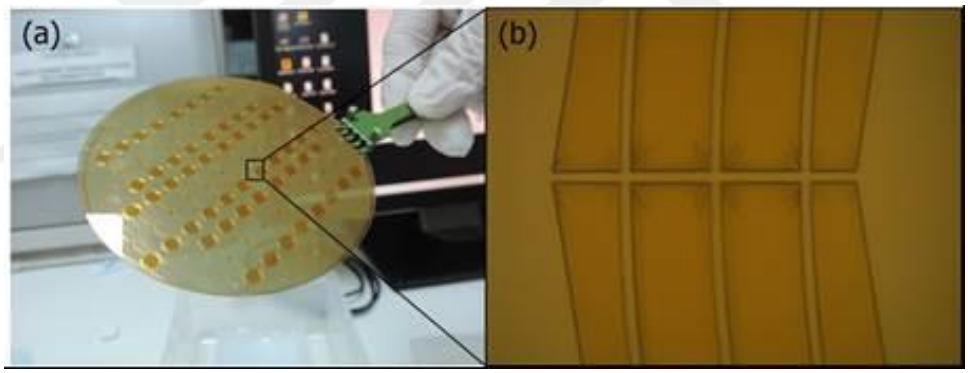


**Figure 3.13.** The parylene surfaces as a result of sufficient baking of sacrificial PR layer. a) The wafer after Au/Ti sputtering, and b) the structures at the inlet side.

*i. Filling of actuation chamber:*

**Problem:** The most critical step of the fabrication is filling process of actuation chamber with photoresist. The surface levels of filled PR layer and wafer should be in alignment so that the parylene diaphragm in the next step be smoothly deposited. Any deformation in the diaphragm may affect the operation performance of the valve.

**Solution:** An optimization process for filling was necessary using different PR types and spin rates. The filling of actuation chamber step was therefore performed several times. The surface profiles of the resist layers were observed with SEM imaging (Figure 3.14).

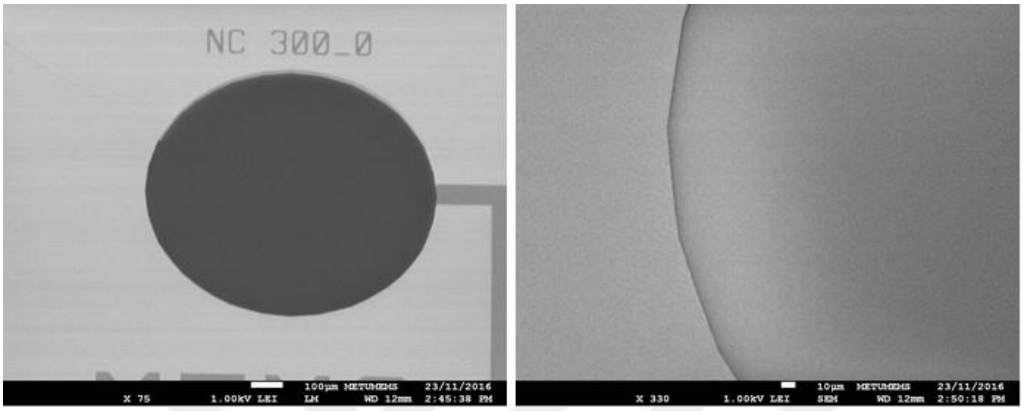


**Figure 3.14.** SEM images of actuation chambers filled with PR (from previous fabrication).

*i. Collapse of diaphragm during PR release:*

**Problem:** Polymers generally have high surface energies. Capillary forces may occur due to surface tension of liquid between the microelements during the release process of sacrificial PR layer. If the forces overcome the restoring force, this results in the stiction of diaphragm (Figure 3.15), which will prevent the valve from functioning, and it will be hard to uncouple after all. Parylene used as the diaphragm material well suits this case. Having fabricated the microvalves using parylene C, stiction was observed during the release process.

**Solution:** Normally, the release process protocol for devices kept in acetone for 3 days was applied by the treatment with IPA for 30 min, methanol for 30 min and drying on hot plate at 70 °C for 5 min. Even though various tests were done by varying possible parameters such as durations, temperature, etc., the device became unusable in case of stiction despite all these steps. To address the solutions of this problem, there are several main approaches on release of MEMS structures to prevent the stiction. If the after-fabrication methods are to be referred, the mostly

followed solutions are freeze-drying, critical point drying (CPD) and surface coating with low surface energy materials such as self-assembled monolayers (SAMs) [86].

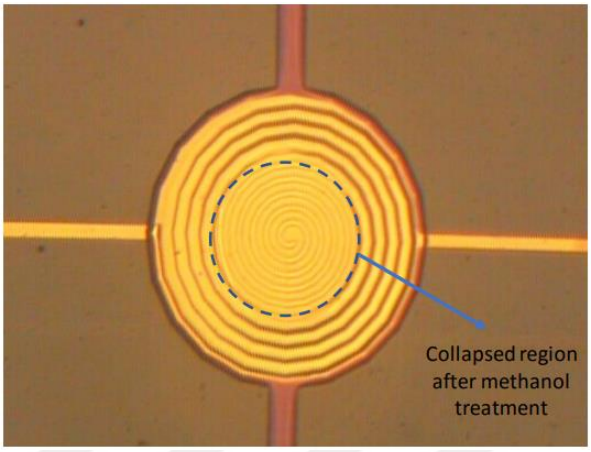


**Figure 3.15.** After Acetone (1.5 day) + IPA (5 min.) + Methanol (5 min.) + hot plate (5 min at 70 °C) treatment, the middle part of diaphragm collapsed without any voltage.

Among these alternatives, vaporization of liquids at a critical point was firstly performed using super critical fluid, $CO_2$, as an effective and widely known process. Since the liquid $CO_2$ introduced during the CPD caused the parylene layers to swell, this method could not accomplish the proper release process, as shown in Figure 3.16. The reason of failure is due to malfunctioning of the device as the pressure value could not be kept constant.

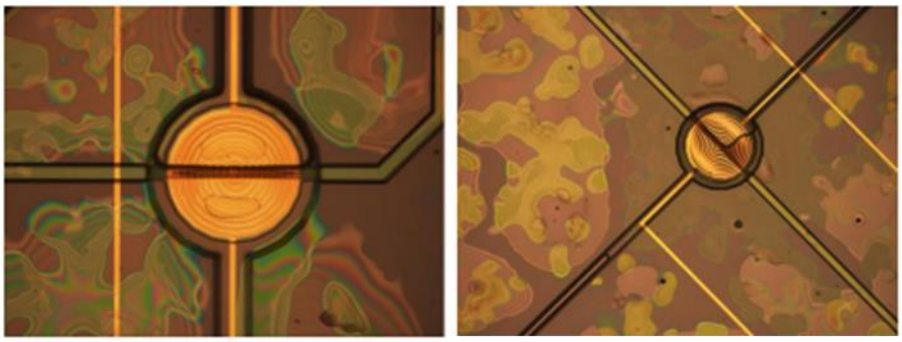

**Figure 3.16.** The results of devices after critical point drying application. Parylene layers have swollen probably due to CO2 introduced during the process.

Then, freeze-drying method is used to eliminate the capillary pull with different chemicals. Takeshima et al. [87] proposed to use t-butyl alcohol that can freeze at 25.6 °C and then expose it to a vacuum environment. As the entire process can be easily implemented, the sample was first treated with IPA and immersed in t-butyl alcohol in the form of liquid warmed by hotplate. Later, it was placed in the refrigerator to make the alcohol frozen in few minutes. Transferring into the vacuum system, it was sublimated after about 2 hour-evacuation. At the end, the dried die was successfully obtained without any stiction. Figure 3.17 indicates the results of six different microvalves to which the freeze-drying protocol was applied, which proved that the stiction could be prevented. However, the device surface becomes dirty due to residuals of t-butyl alcohol even though the duration under vacuum was extended.

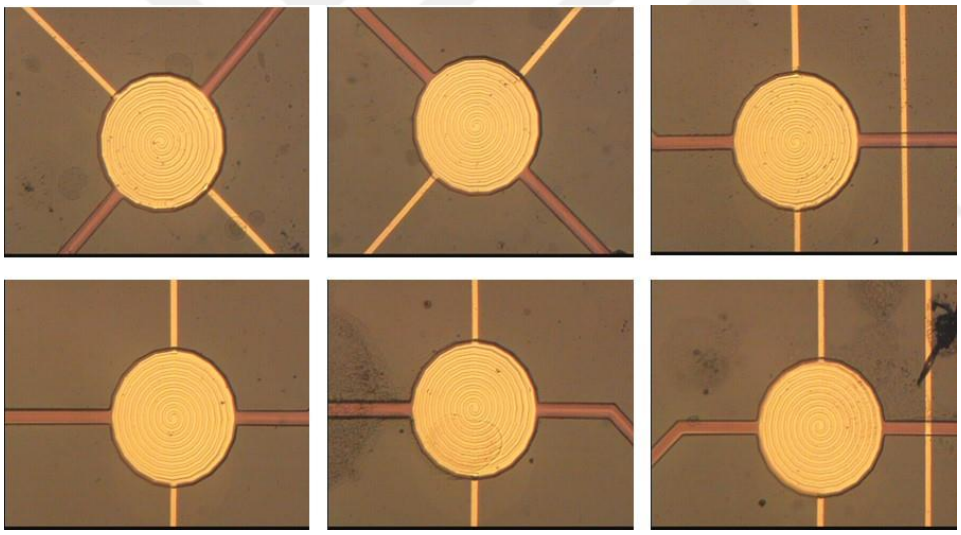

**Figure 3.17.** The results of freeze-drying method for diaphragm collapse of six different microvalves. There was no stiction observed in all diaphragms after the treatment with t-butyl alcohol.

### 3.3.1.4. Characterization

There are several significant figures of merits by which a microvalve operation is evaluated: pull-in and pull-out voltages, response times during opening and close of the valves, pressure range and reliability.

The test set-up for microvalve characterization is shown in Figure 3.18. During the test, a high voltage supply was used to apply the necessary potential to the electrodes while observing under a probe station. The videos were recorded via 30 fps camera and processed with ImageJ and MATLAB.

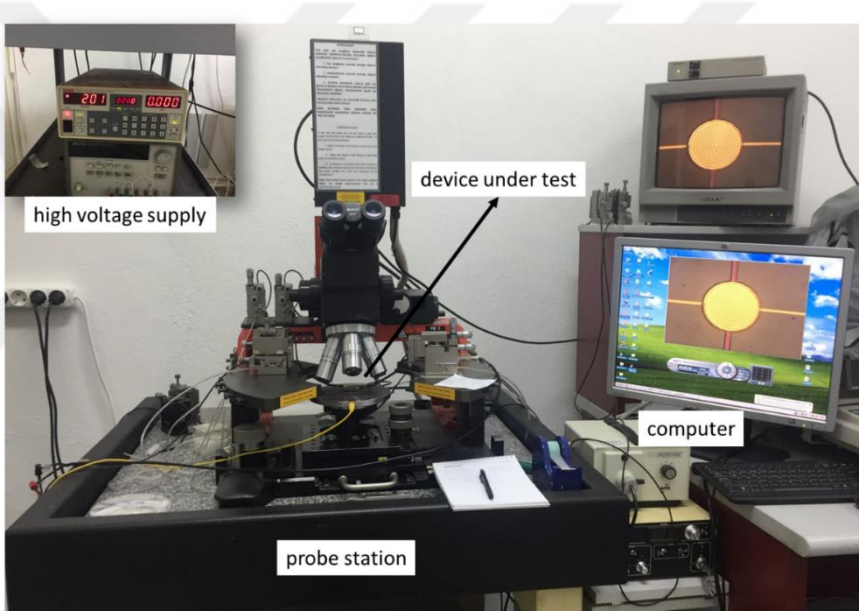


**Figure 3.18.** The experimental set-up for the characterization of an electrostatic microvalve.

The full characterization of the valve related to above mentioned parameters was performed both under flow and no flow conditions. Different electrode radii (300 µm and 410 µm) and shapes (full and spiral top electrodes) were used in the tests and their results were comparatively presented.

*Pull-in and Pull-out Voltages:* Pull-in voltage is defined as the voltage beyond which the movable valve diaphragm suddenly collapses due to instability point in the

electrostatic force characteristics. The pull-in voltage was determined by incrementing the voltage value by 1 V steps from 0 V to a certain value. Having recorded the pull-in voltage, the voltage applied was gradually reduced until the diaphragm turned back to its initial closed state to specify the pull-out voltage. The experimental pull-in voltage values of the first-generation microvalve is given in Figure 3.19. The result shows that pull-in occurred at an applied voltage of 177 V while the pull-out voltage value was measured as 95 V. In consistent with the theory presented by [88], pull-out voltage was found as at a level significantly lower than that of pull-in, which states a hysteresis behavior.

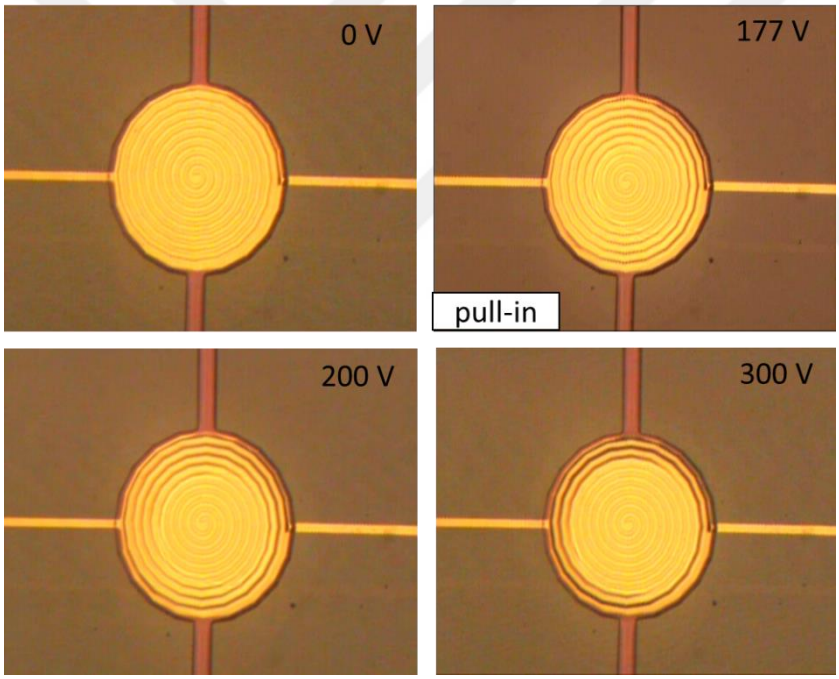


**Figure 3.19.** Microvalve pull-in voltage determination tests. The pull-in occurs at 177 V. The diaphragm collapses and the corresponding applied voltages of 0 V, 177 V, 200 V and 300 V are indicated.

*Response Time:* How fast the microvalve can respond to a change of state in response to a variation in the applied voltage is defined as the response time. The opening and closing reaction times were investigated. The same test set-up was utilized except that

square wave was applied instead of DC voltage. Thus, a high voltage sequencer was used to supply the necessary signal form and voltage value. The response time of a spiral top electrode microvalve with radius of 300 µm was determined using ImageJ. The results indicate that the opening response time is about 0.94 s whereas that of closing occurs at 1.86 s.

*Repeatability:* The repeatability of microvalves was also tested to evaluate one of the important figure of merits of the microvalve performance. The valves were applied to 200 V which is slightly higher than their pull-in voltage and provided to be on/off at a certain period more than 50 times. It was proven that the valve operation was repeatable.

### 3.3.2. Second-Generation Design

#### 3.3.2.1. Design

In order to use the microvalves in the integrated LOC system, the yield must be increased in terms of number of properly operating devices while improving their performances. Therefore, the requirements with the proposed solutions and optimizations have led the way of proposing second-generation design. In this design, the operation of the valve was kept exactly as the same as the previous generation whereas the fabrication process was altered depending on the optimizations. Furthermore, while the elements required for the actuation mechanism were fabricated on the glass wafer, the microchannel configuration was transferred to the PDMS material this time. In other words, the microvalve and microchannel are designed to be bonded using oxygen plasma. Figure 3.20 illustrates the design of second-generation electrostatic microvalve which is in the closed state in its normal operation mode and Table 3.2 denotes the necessary design parameters of the valve and mechanical material properties. Note that the operation of the microvalve is exactly the same as the first-generation microvalve.

**Table 3.2.** Design parameters and mechanical properties of the materials used in the design are shown together with the second-generation design figure.

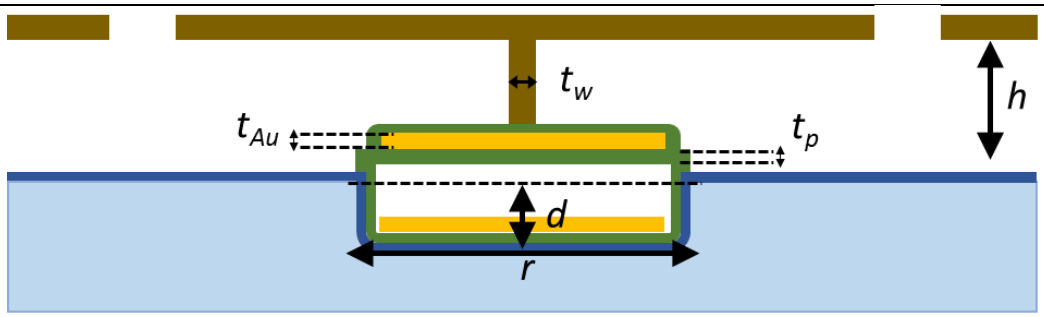


**Figure 3.20.** Design of a second-generation electrostatic microvalve and important parameters.

| **Design Parameter** | **Dimension** |
|---|---|
| Actuation chamber depth ($d$) | 5.5 µm |
| Actuation chamber radius ($r$) | 300 µm, 410 µm |
| Diaphragm thickness ($t_p$) | 2.5 µm |
| Electrode thickness ($t_{Au}$) | 0.22 µm |
| Channel height ($h$) | 40 µm |
| **Mechanical Properties** | **Value** |
| Dielectric permittivity of parylene ($\varepsilon_p$) | 3.15 |
| Elastic modulus of parylene ($E_p$) | 3.2 GPa |
| Poisson's ratio of parylene ($\upsilon_p$) | 0.33 |
| Elastic modulus of gold ($E_{Au}$) | 77.2 GPa |
| Poisson's ratio of gold ($\upsilon_{Au}$) | 0.42 |

### 3.3.2.2. MEMS Fabrication

The fabrication process flow was revised for the optimized steps and new microchannel bonding method, and several changes have been made in the flow. Unlike in the fabrication of first-generation devices, glass wafer was used as the substrate material instead of silicon wafer because it was planned to bond PDMS with

glass. Figure 3.21 shows the mask layouts and their details. The followed process flow given in Figure 3.22 is as follows:

A glass wafer cleaned with piranha was first coated with Cr/Au (50nm/500 nm) metal layers to mask the glass. The regions of actuation chambers and air vents were defined by photolithography using AZ 5214. These layers were patterned with wet etch to clear out the regions to be etched. The glass was etched in pure HF for 50 second to reach a depth of approximately 7 μm. Subsequently, PR removal was carried out by immersing the wafer in PRS 2000 stripper heated to 80 °C. After 15 min + 15 min PR strip treatment, all sacrificial metal layers were removed. Then, 3 minutes-BHF treatment was applied to smooth sharp edges. Afterwards, parylene layer for insulation was deposited. The thickness of parylene was 1 μm and silane was used to increase its adhesion to the surface to avoid the parylene-resist interaction encountered in previous processes.

Next, the bottom electrodes were formed. Ti/Au metal layers were sputtered in Bestec for the thicknesses of 20 nm / 200 nm, respectively. Then, photolithography was done with SPR 220-3 and the electrodes regions were defined by wet etch process. The gold layer was etched with commercial transene gold etchant for 50 sec while the titanium was immersed in HF:H2O2:H2O (1:1:160) solution for 35 sec. All the PR layers were then stripped in acetone for an hour. PRS 2000 stripper could not be used as parylene layer now exists.

Having formed the bottom electrodes, the actuation chambers and air vents were filled with SPR 220-7 resist layer. The thickness of PR layer was determined the same as the depth of the chamber. For hard bake procedure, 6 hour long-hard bake at 90 °C was applied to the wafer. After this process, wafer was deposited with parylene layer of 2.5 μm for membrane formation without silane. The same metallization process was applied to form the top electrodes as in the case of bottom electrode step. Later, a thin parylene layer of 2 μm was deposited to prevent the liquid from electrolysis. After this step, parylene layer was patterned by first performing photolithography and then

parylene RIE etch. This is the last step of the fabrication on the glass wafer and microchannel formation is done with PDMS instead of on top of microvalve using parylene.

For PDMS/glass bonding, a mold wafer was fabricated with AZ 40 XT process. This resist has a positive thick resist with good aspect ratio and the PR thickness was adjusted to be about 40 µm. The PDMS was prepared with mixture of Sylgard 184 pre-polymer (Dow Corning) and curing agent with a ratio of 10:1, and put it in desiccator for 2-3 hours to get rid of bubbles. The PDMS was poured on the mold wafer, and then placed into oven for curing at 80 °C for 2 hours. When finished, the cured PDMS was carefully cut around the edges of petri, removed and partitioned off. Finally, fluidic inlets and outlet were created by punching before bonding.

Since glass-based and PDMS devices were fabricated, the next and final step is permanent plasma bonding of these devices to create a tight seal for microchannel formation. Before bonding, the PDMS surface was cleaned with the help of a scotch tape to remove dusts. With the help of plasma, both device surfaces were exposed to oxygen plasma and the surface properties are changed. The quality of bonding is determined by the exposure duration, RF power and oxygen flow. In this case, the bonding was performed at 40 W and 26 sccm for 40 sec. Right after the treatment, a drop of methanol between the devices was left so that intimate contact of devices was temporarily prevented. This duration allowed to align the PDMS microchannel with the microvalves under the microscope. After the alignment, the devices were put on a hot plate at 110 °C for 5 minutes to evaporate the methanol in between. Then, the device was ready to be tested.

The fabricated second-generation microvalve on the glass wafer is provided in Figure 3.23.a. It contains only the microvalve part. In Figure 3.23.b, the glass die and PDMS microchannel were bonded using oxygen plasma.

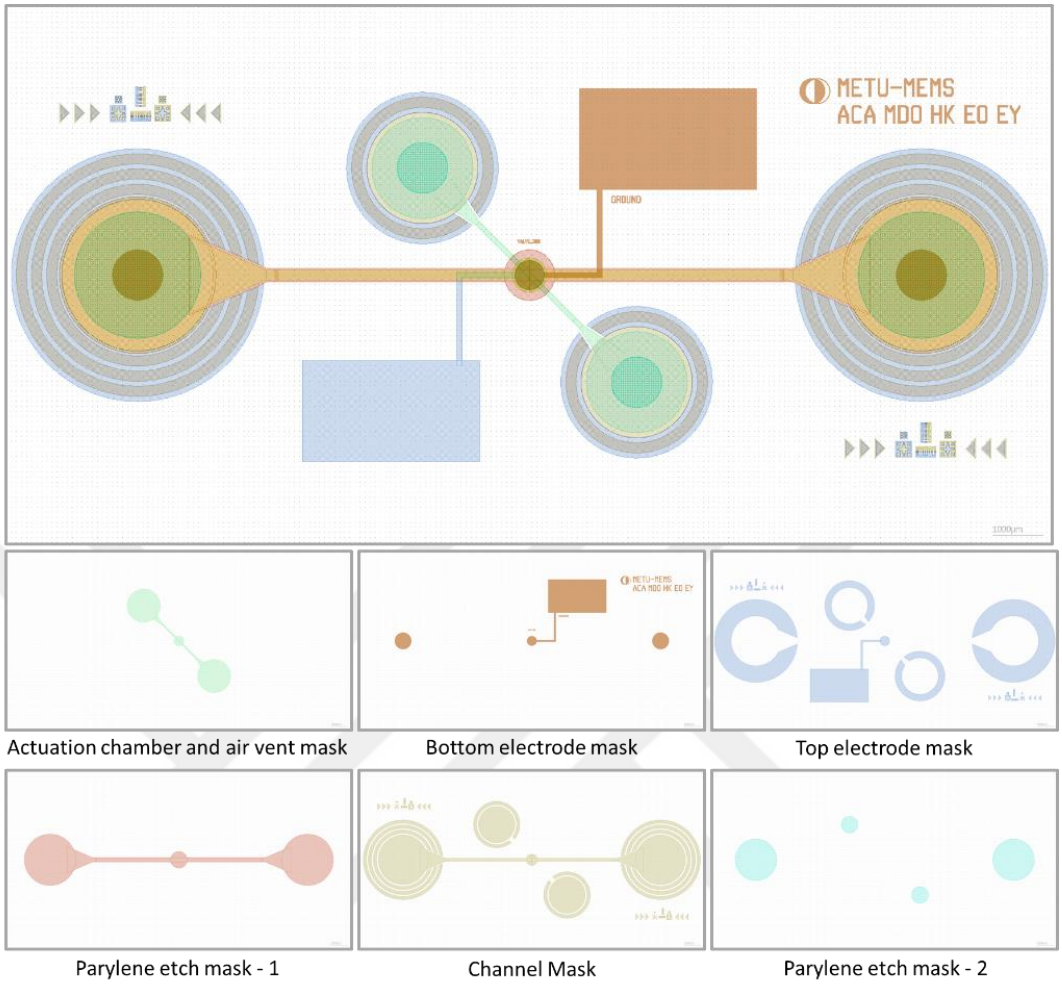


**Figure 3.21.** Wafer-level mask design and die-level mask layouts for the second-generation electrostatic microvalve.

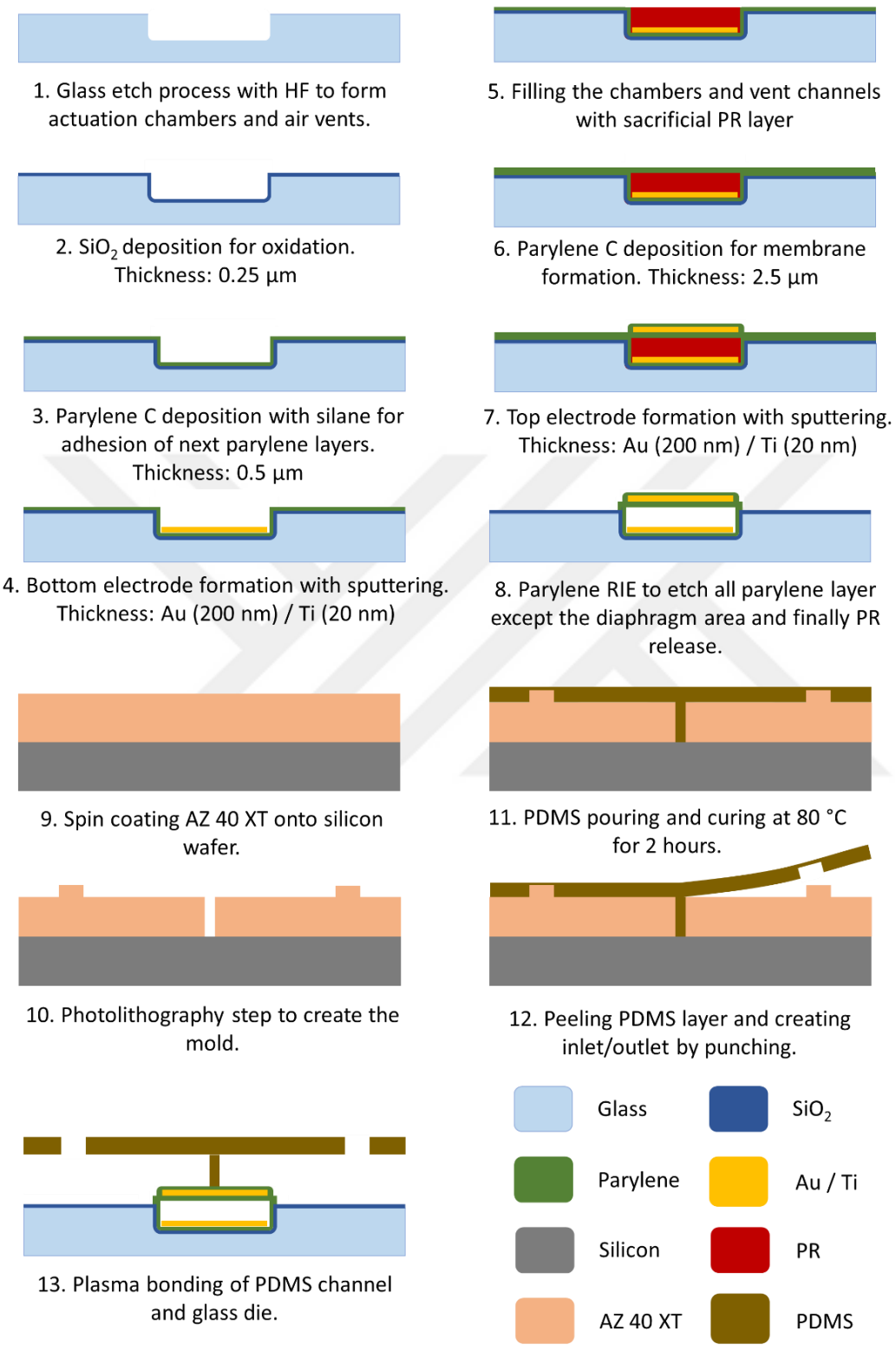


**Figure 3.22.** Fabrication flow of the second-generation microvalve design.


**Figure 3.23.** a) The fabricated second-generation electrostatic microvalve on the glass wafer and b) the plasma bonded die that includes both microvalve and PDMS microchannel.

### 3.3.2.3. Characterization

*Pull-in and Pull-out Voltages:* The second-generation electrostatic microvalves were first tested to determine the pull-in and pull-out voltages under atmospheric pressure without fluid flow. As before, the pull-in voltage value was obtained by increasing the applied voltage value by 1 V-steps. Subsequently, the method of gradually reducing the voltage until the diaphragm returned to its initial closed state was used to determine the pull-out voltage.

Figure 3.24 indicates the relevant test results for the microvalves providing minimum and maximum operation performance in terms of voltages. Relatedly, the closed/open states for different valves with 300 µm and 410 µm in radius and having full and spiral electrodes were investigated. Among these types, the first tested valve was 300 µm-valve with full electrode. The test results showed that 76 ± 11.5 V was obtained as the highest pull-in performance and pull-out voltage was determined as 54.3 ± 9.5 V for the 300 µm-valve with full electrode. Since it was thought from the beginning of the

design process that the voltage could be high, the valve radius was first increased to 410 µm, which aims to reduce the mechanical stiffness. It was found that the pull-in occurred, this time, at 70.8 ± 5.6 V, lower than the first type. Likewise, the pull-out voltage became lower and was determined to be 41.3 ± 9.0 V. Finally, the variation was made on the shape of the top electrode material for further reducing the voltage. It was changed from full to spiral-shape electrode. Then, the voltage for the collapse of the diaphragm was found as 41.5 ± 7.7 V for the valve with 410 µm in diameter with spiral top electrode in shape while the corresponding pull-out voltage for the same valve is 23.0 ± 5.6 V, the lowest pull-in and pull-out voltages. The overall results can be compared in Table 3.3. As can be seen from the results, there is a hysteresis effect observed in the voltage characteristics of the valve as the pull-out occurs at a lower voltage level than pull-in does.

As can be interpreted from the above results, the pull-in voltages found in the experiments are higher than those predicted by both theory and the simulations, which stems from several reasons. First, the fabricated top electrode is not fully clamped at the edges but resides on top of the parylene membrane which is clamped at the outer edges. Second, the parylene membrane also leads to additional stiffness to the pull-in event. Besides, there occurs some unexpected cases during the fabrication such as excessive heating due to baking processes. For all these reasons, additional stiffness effect is introduced, causing the pull-in voltage to increase and thus the pull-out voltage to decrease, correspondingly.

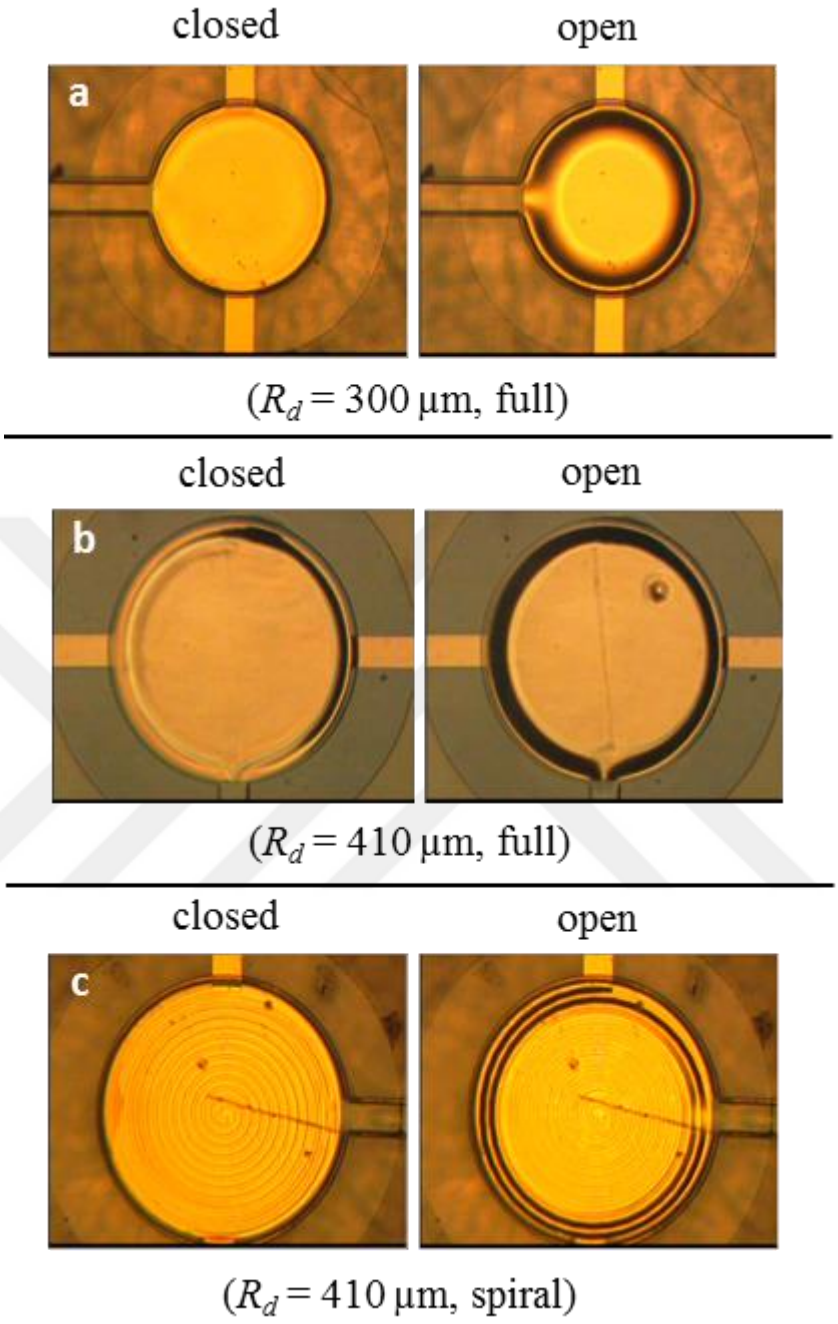


**Figure 3.24.** Determination of the pull-in voltages under atmospheric pressure and no flow for different microvalve types. Pull-in occurs at a voltage of a) 76.0 ± 11.5 V for a full electrode-valve with a radius of 300 µm, b) 70.8 ± 5.6 V for a full electrode-valve with a radius of 410 µm, and c) 41.5 ± 7.7 V for a spiral electrode-valve with a radius of 410 µm.

**Table 3.3.** Characterization results for different electrostatic microvalve types.

| Figure | Type of Top Electrode | Diaphragm Radius (µm) | Pull-in Voltage (V) | Pull-out Voltage (V) | Opening Response Time (s) | Closing Response Time (s) |
|---|---|---|---|---|---|---|
| 2.26.a | Full | 300 | 76.0 ± 11.5 | 54.3 ± 9.5 | 0.87 ± 0.05 | 1.83 ± 0.12 |
| 2.26.b | Full | 410 | 70.8 ± 5.6 | 41.3 ± 9.0 | 0.59 ± 0.06 | 1.89 ± 0.27 |
| 2.26.c | Spiral | 410 | 41.5 ± 7.8 | 23.0 ± 5.7 | 0.74 ± 0.03 | 2.02 ± 0.98 |

To determine the effect of pressure on the pull-in voltage, all tests were tried to be repeated under pressurized air flow. After the characterization under no vacuum applied, microvalves were tested for flow characterization. Air was used as the working fluid in flow characterization tests. The microvalve with a radius of 300 µm was tested for pull-in voltage dependency caused by possible outlet pressures for the operation of the device. The images of the test results are given in Figure 3.25. Under outlet vacuum pressures of 0 kPa, -5 kPa, -10 kPa, -15 kPa, and -20 kPa, the pull-in voltages were determined as 90 V, 130 V, 150 V, 175 V, and 215 V, respectively. The PDMS channel was mechanically bonded to the glass-based device with the help of a custom holder. The results of the tests carried out with air as the working fluid indicate that pull-in voltage increases with increasing outlet pressure. For the sake of visuality, Figure 3.26 show that the change in the pull-in voltage with respect to outlet pressure change is almost linear.

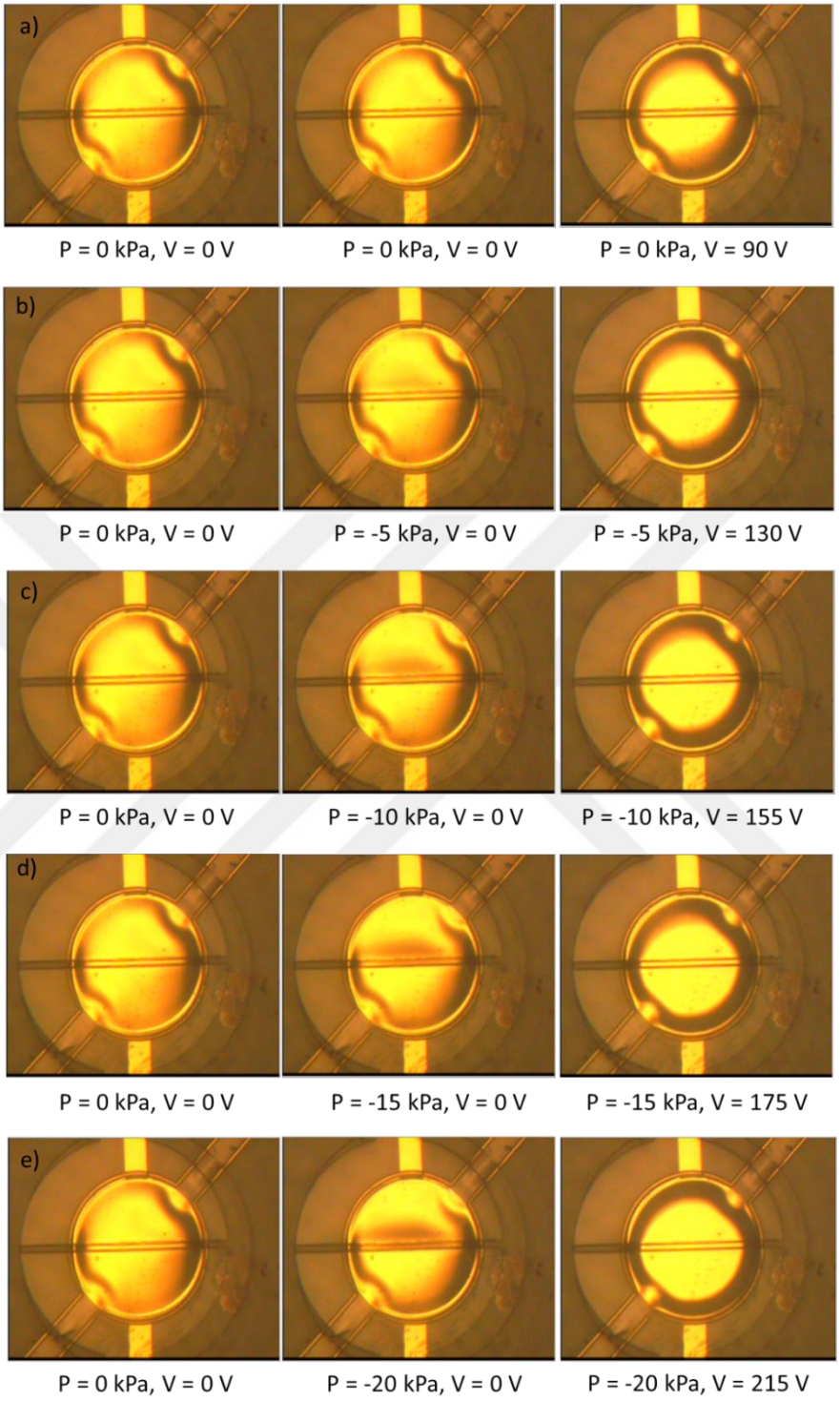


**Figure 3.25.** Determination of pull-in voltages under outlet vacuum pressures of a) 0 kPa, b) -5 kPa, c) -10 kPa, d) -15 kPa, and e) -20 kPa for the microvalve with a radius of 300 µm. The PDMS channel is mechanically bonded to the glass-based device with the help of a custom holder.

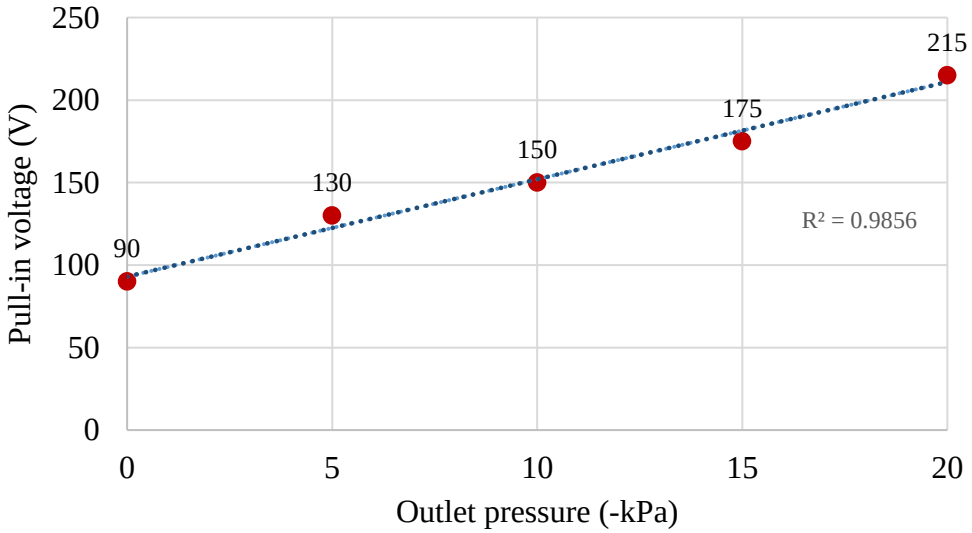


**Figure 3.26.** Pull-in voltage versus outlet pressure for the microvalves with a radius of 300 µm. Dashed line denotes the curve fitted to data with R-squared value.

*Response time:* The opening/closing response characteristics of the valves were also investigated to evaluate their switching performances (Table 3.33). It was measured that the opening response time of the full electrode microvalve with 300 µm in radius is 0.87 ± 0.05 s whereas corresponding closing response time is 1.83 ± 0.12 s. On the other hand, the full electrode valve with a radius of 410 µm opens at 0.59 ± 0.06 s and closes at 1.89 ± 0.27 s. The third type of microvalve, 410 µm-valve with spiral top electrode, responds at 0.74 ± 0.03 s for opening operation after a voltage slightly higher than the pull-in value is applied. It closes at 1.32 ± 0.18 s. Together with the voltage reduction, last microvalve designs offer faster response durations during opening and closing.

As a result, it is observed that the valves can respond to voltage variation in less than 1 s while going from closed state to open state. However, the closing duration is slightly greater than that of opening. The microvalves displayed a performance between 1.5- 2.8 s to close the fluid flow.

*Repeatability:* The microvalves were also tested for repeatability in terms of elasticity of the diaphragm. The valves with 300 µm and 410 µm in radius were applied to 90 V

and 60 V, respectively, which is slightly higher than their pull-in voltages, and made on/off at certain periodic cycles. The microvalves were operated more than 50 times without any significant voltage change, and it was proven that the operations of valves were repeatable despite the increase in their pull-in voltages.

### 3.4. Operation Problems of On-Chip Microvalves

As stated above, the fabrication of the lab-on-a-chip device was mainly performed by bonding of glass device with valves and PDMS device. The PDMS part provides the microchannel configuration and the valve seat or the wall used to prevent fluid flow. During the bonding process, there occurs the intimate contact of the wall with the parylene diaphragm, which we expected in advance. What we did not expect is that the wall causes the diaphragm to partially collapse and even sticks to its surface because PDMS and parylene cannot be normally bonded using plasma bonding. Therefore, it becomes quite difficult to create an opening for the fluid to flow between the wall and the diaphragm, which results in the failure of the valve operation in almost all cases. Figure 3.27 indicates the tests results of valve operation with fluid flow. Since the valve was not operated properly due to wall stiction and the collapse of the diaphragm, red dye could not flow through the opening.

In order to solve this general problem, two possible solutions can be suggested as follows:

1. After completing the fabrication of the glass device, instead of bonding process the PDMS microchannel can be directly formed on the glass device itself. The photoresist for microchannel configuration is created. To prevent the stiction of the wall, micro soap is dropped on these specific areas. Then, PDMS is directly poured on the PR channel so that the PR release is realized after channels are formed without requiring the bonding process.

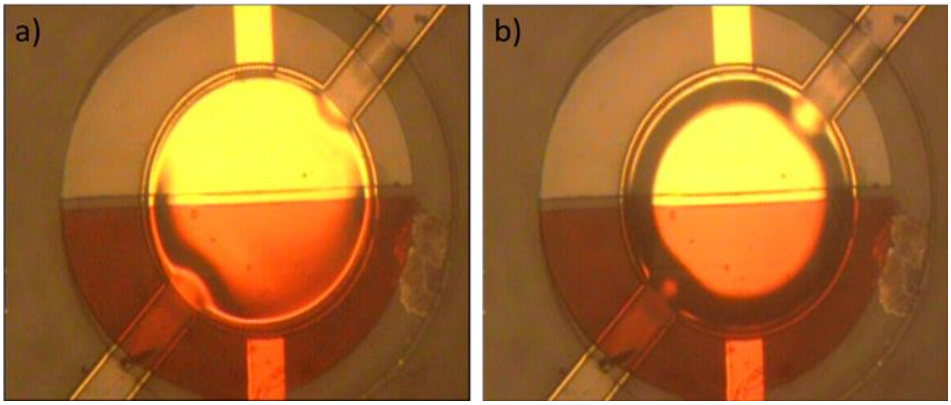


**Figure 3.27.** Microvalve test with fluid flow. a) The fluid given through the channel and the wall prevents the fluidic flow, and b) the voltage is applied to the valve to open for the flow and yet the flow is not realized due to the stiction of the wall to the diaphragm

2. The wall stiction and collapse of the diaphragm can be also overcome by following another fabrication method. Since PDMS is an elastic and sticky material, if the wall is made from a more the rigid material the problems can be solved. For example, the anodic or eutectic bonding of glass and silicon wafers enables that the channels and walls is made of glass material bonded with silicon base containing electrostatic microvalves. Ali Can Atik has been working on the fabrication process for this method, and the results will be shared by him once it is completed.

## 3.5. Conclusion

This chapter presented the theoretical and practical implementation of a normally closed electrostatic microvalve. For this purpose, the analysis of pull-in effect which is a need-to-consider issue for the electrostatic devices was shown based on 1-D lumped and continuous reduced-order models and FEA method. Then, the design details, fabrication flow and test results of the first-generation normally closed electrostatically actuated microvalves were given. Upon the difficulties in the fabrication process and unsatisfactory performance of the first kind, the second-generation microvalve was proposed by examining the design and fabrication. The

fabricated devices were tested to characterize the operation performance and it was seen that their performances were superior to that of first-generation. The theoretically calculated value of the pull-in voltage was calculated as 34.2 V whereas the simulation results yielded that of 37 V. On the other hand, the experimental results showed that the common operation voltage of the first-generation was determined as 177 V, which is a quite high value. The second-generation devices revealed a better performance and the pull-in voltage required during the device operation was determined to be 76 ± 11.4 V for 300 µm-valve with full top electrode and the voltage was reduced to 41.5 ± 7.8 V for 410 µm-valve with spiral top electrode. Moreover, the performance of the final microvalves were tested under an applied pressure for the actual operational scenario.

The reasons why the experimental values are much higher than the theoretical values are the non-ideality of diaphragm boundary conditions, the problems that arose during the fabrication (excessive heat etc.) and the air venting channels that were not included in the theoretical calculations and bring additional air flow resistance for the air inside the actuation chamber during the collapse of the diaphragm. Rather than providing the perfect operational performance, the main purpose of the microvalves is here being integrable to the LOC devices and providing as high yield as possible on a LOC device. These objectives were achieved by establishing steady fabrication process flow and drying method and a great number of operable microvalve were obtained.

# CHAPTER 4

# DRUG EFFECT ANALYSIS TESTS

## 4.1. Fabrication of Lab-on-a-chip System

In the simplest term, the ultimate process integrates the microvalves with microchannel network. The beauty of the integration is that all the fabrication steps are the same as that of microvalve described in Section 3.3.2.2; therefore, these devices are fabricated together with microvalves on the same wafer. Only the design of device is modified with the addition of microchannel network. The detailed process flow is presented in Table B.0.2 in Appendix B. Also, the masks of the system are provided in Figure 4.1. The mask was drawn using Cadence Virtuoso layout editor. The dimensions of parylene channel have been determined considering the appropriate flow rates (predetermined with COMSOL simulations) for the desired droplet generation frequency under a certain pressure using MATLAB tool.

Parylene C is used to facilitate the MEMS fabrication and integration of the electronic components and microchannels of LOC platform. The use of parylene material in microvalve and microchannel fabrication stages offers an advantage of low air-permeability which is an important characteristic during incubation period. In addition, since air permeability of parylene is lower than that of PDMS, parylene also solves the problem of air-permeability-related drying problems.

The fabricated drug effect analysis device is shown in Figure 4.2.a. In the channel network design, it was aimed to go down to channel widths of 50 and 100 μm in the latest models. The corresponding channel depths were defined as 40 and 25 μm, respectively. By this way, the necessary forces required for cells to be aligned at the middle of the microchannel can be revealed. Also, we fabricated the mold wafer for PDMS channel by performing AZ 40 XT photolithography. The mold wafer is shown

in Figure 4.2.b. Finally, the glass die and PDMS microchannel was bonded and the result is given in Figure 4.3.

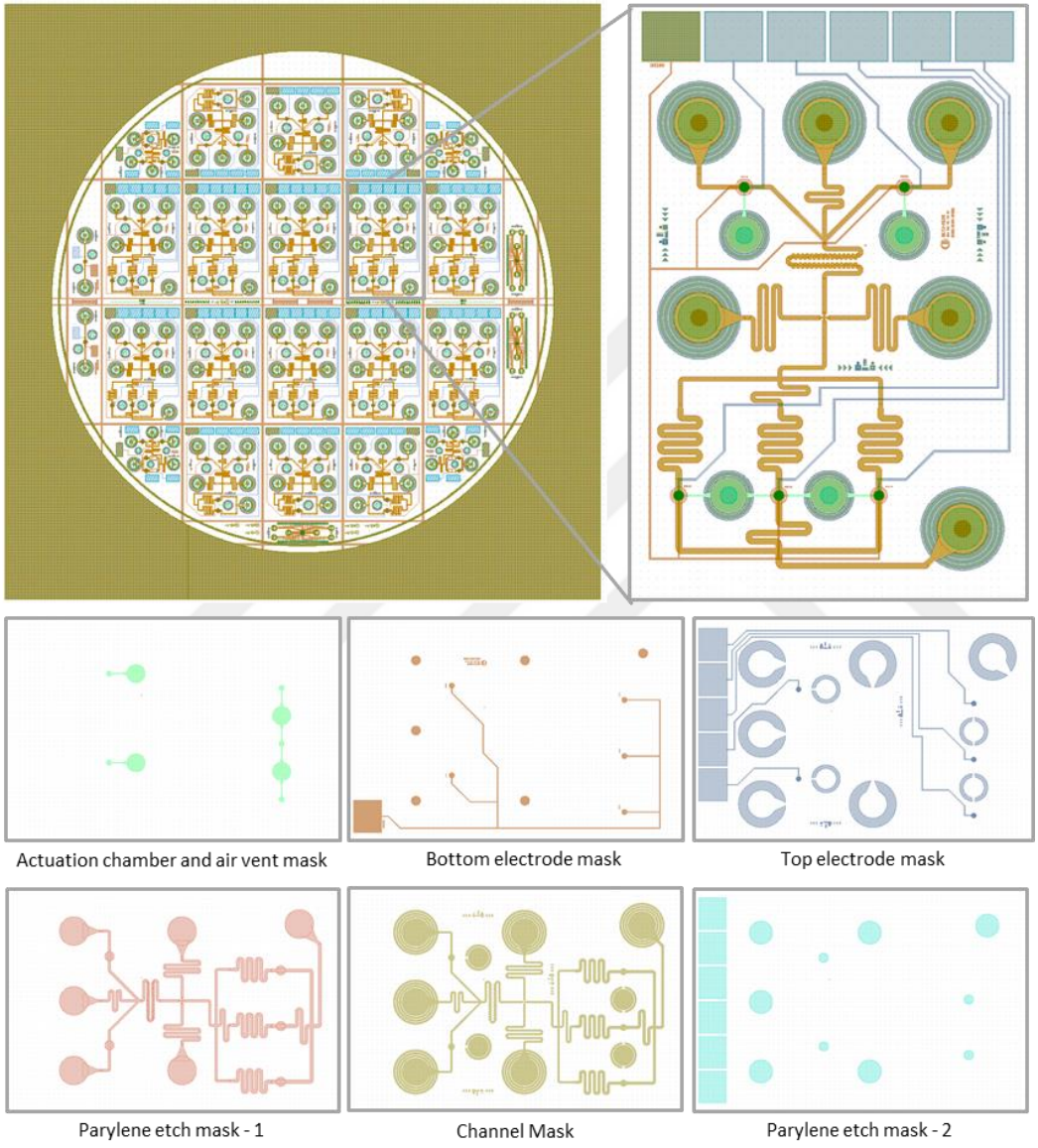


**Figure 4.1.** Wafer-level and die-level masks for drug effect screening system.

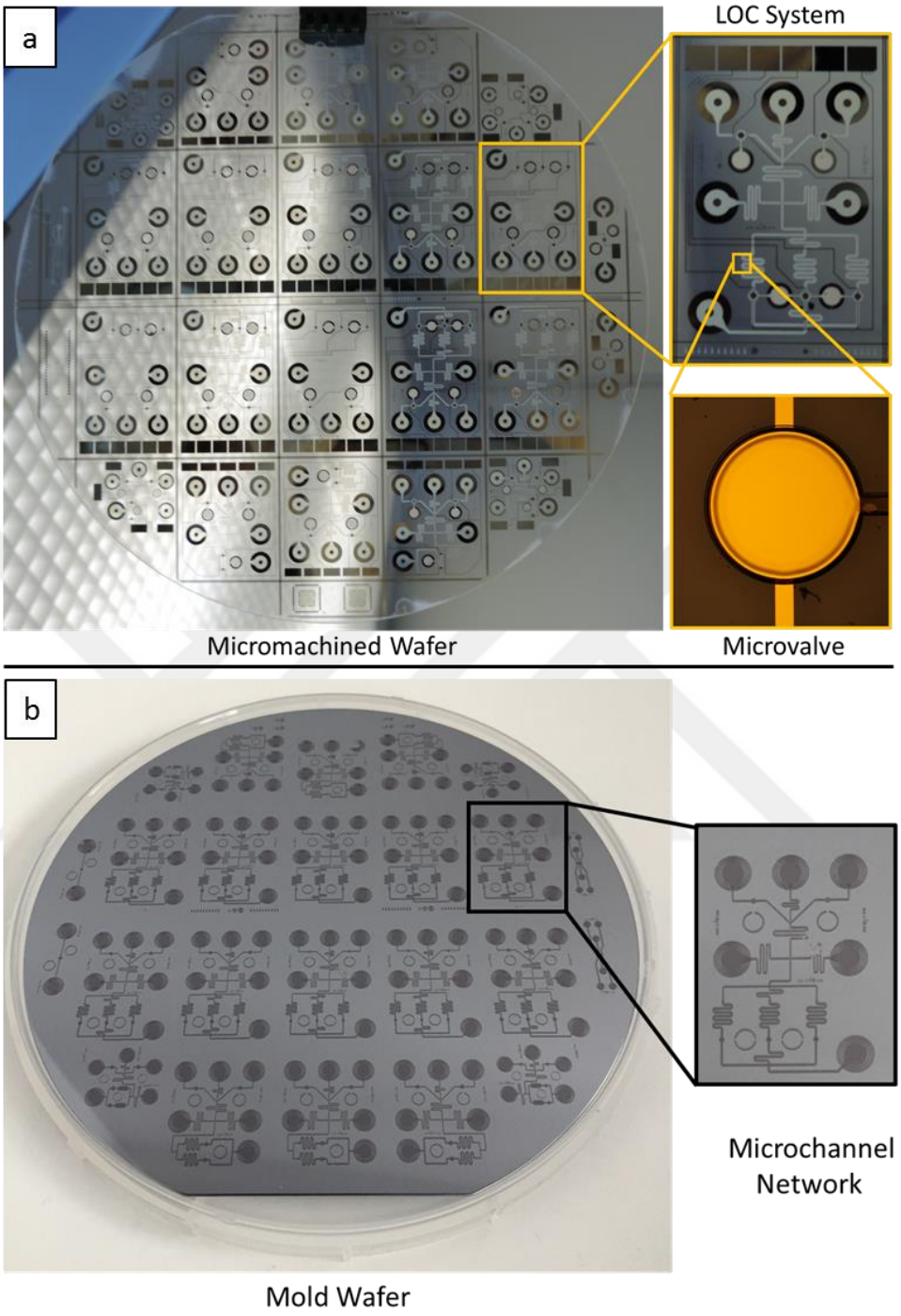


**Figure 4.2.** a) Micromachined glass wafer after parylene RIE process was completed (left), closer view of a die with five electrodes (top right), and microvalve captured under the microscope (bottom right), b) silicon-based mold wafer fabricated with AZ 40XT photolithography process for PDMS-molded microchannel formation (left) and die-level microchannel network (right).

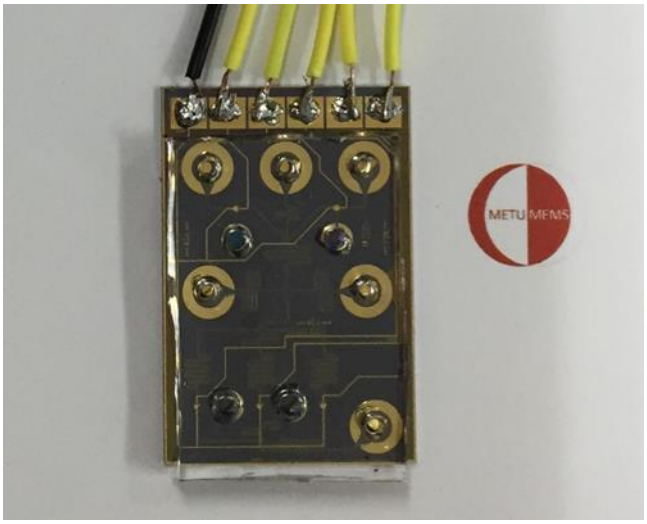


**Figure 4.3.** The fabricated and plasma bonded drug effect analysis system.

## 4.2. Drug Effect Anaylsis Tests using K-562 Leukemia Cells

### 4.2.1. Experimental

The time-dependent analysis for drug efficiency was conducted under fluorescent microscope (Leica Microsystems, DMi8 Microscope). The fluid flows in the system were controlled by means of a vacuum pump (Elveflow VAC-P-600) at a negative vacuum applied through the outlet. The measurement of droplet diameters and image processes of droplet formation frequency and mixing efficiency were conducted using custom image processing algorithms written in MATLAB and ImageJ.

The cell lines used in the experiments was K-562 myeloid leukemia cells supplied by Biology Department of METU. The drug types and dosages to be used in the tests were determined by Maryam Parsian. The drugs whose efficiencies were investigated are Doxorubicin and Imatinib. According to the IC50 values of drugs determined by Maryam Parsian, doxorubicin was prepared for the concentration of 20 μM whereas imatinib dosage was 10 μM. During the droplet formation tests, the mixture of drug(s) and cell suspension containing cell medium, RPMI, was used as dispersed flow

whereas fluorinated oil (HFE-7500, 3M) with 2% PicoSurf-1 (Dolomite Microfluidics, UK) surfactant and later with 5% Krytox FSH 157 (Dupont$^{TM}$, 5 and 10 cSt, 930 kg/m$^3$, Australia) were used as the continuous phases, alternately.

As the fluorescent probes, FDA (Fluorescein Diacetate, Sigma-Aldrich, F-7378) for living cell assay and PI (Propidium Iodide, Sigma-Aldrich, P-4170) for dead cell assay were used. FDA is an agent used in the detection of living cells that fluoresce after it has been enzymatically degraded in the cell through the cell membrane. PI, on the other hand, is a molecule that can label cell DNA as a fluorescent molecule which cannot pass on living cells through cell membranes. When cell viability is no longer protected, PI enters the cell and binds to the cell DNA. Stock solution of FDA was prepared by dissolving 10 µg in 1 ml PBS while that of PI was 1 µg/ml. However, this solution was modified for different experiments to optimize the fluorescent intensity of dead cells. Corresponding to the preferred reagents, the embedded filters in fluorescent microscope FITC and TXR were utilized for live and dead cell assay discrimination, respectively.

The experiments were performed with $10x10^6$ cells/ml concentration to increase the rate of cell encapsulation. For the analysis of cell viability experiments, the following cell staining protocol was applied. Stock solution of FDA of 2.5 µl was added to the cell stain and allowed to wait for 15 min. As the FDA is able to be taken up by cells after a while, the cell stain was washed with RPMI by centrifuging (210 g for 7 min) for 2 times to remove the background dye. Then, PI of 100 µl was added to the stain.

### 4.2.2. Results and Disccusion

To assess the cytotoxicity, it is first necessary to determine at which dosages the drugs will be applied to the cells for a certain amount of time. For this purpose, XTT experiments were carried out by Maryam Parsian. XTT assay analysis is used to screen the number of viable cells regarding activity of cytotoxic agents and cell proliferation. The corresponding analysis results for doxorubicin and imatinib up to 72 hours are

given in Table 4.1 and Table 4.2, respectively. The efficacy of the drugs over the time can be evaluated based on their half maximal inhibitory concentrations, $IC_{50}$. In other words, $IC_{50}$ indicates the necessary drug concentration that decreases the activity of target by 50%. Additionally, $IC_{20}$ value for imatinib was provided below since $IC_{50}$ values for 6 and 12 hours could not be found.

**Table 4.1.** XTT analysis of Doxorubicin dosage.

| DOX | 6h | 12h | 24h | 48h | 72h |
|---|---|---|---|---|---|
| **$IC_{50}$** | 15.15 µM | 9.4 µM | 0.77 µM | 0.047 µM | 0.0124 µM |

**Table 4.2.** XTT analysis of Imatinib dosage.

| IMTNB | 6h | 12h | 24h | 48h | 72h |
|---|---|---|---|---|---|
| **$IC_{50}$** | - | - | 2.3 µM | 0.51 µM | 0.49 µM |
| **$IC_{20}$** | 0.55 µM | 0.76 µM | 0.17 µM | 0.095 µM | 0.048 µM |

The system used here is a droplet-based system in which emulsions of droplets are in contact with each other and the surrounding PDMS material. This may lead to coalescence of droplets due to high interfacial tension. Therefore, droplet stabilization tests were conducted to observe how long the droplets could be volumetrically preserved and how to provide long-term duration of stabilization. Consequently, surfactants were used to lower the interfacial tension, which also increases the frequency of droplet generation. Achieving that the droplets were stabilized with 5% Krytox surfactant up to 6 hours, it was decided to use dosages closer to $IC_{50}$ values of drugs at 6 hours. Therefore, dosage of doxorubicin was used as 20 µM. On the other hand, since $IC_{50}$ value of imatinib could not be determined, an estimated value of 1 µM was used. Later, these values were slightly altered during the experiments depending upon the other factors.

Unlike the use of surfactant for lowering the interfacial tension and increasing the stability duration, there are several factors that uncontrollably lowers the wetness of the droplet surface and thus the test duration. In normal conditions, the droplets should suspend in the continuous phase by preserving the surface wetness. However, the droplets get contact with the PDMS due to gravitational forces, leading to adsorption. Moreover, air permeability of the PDMS material is relatively high that causes drying due to air flow. The experiments were carried out in the cleanroom where continuous air flow exists with a room temperature of 18 °C and a humidity of %17. This leads to the droplets to shrink in volume in a short period of time.

The cytotoxicity screening of cells in droplets requires the cell to maintain their metabolic activities for long durations. This can normally be achieved by refreshing the medium. Yet, such treatment is difficult to realize in droplet-based systems without having array trappers for droplets [89] or open surface for the liquid handling access [90] since the droplets cannot stand still under continuous liquid flow. The system proposed here has closed serpentine microchannels as the observation area without any trappers.

For all reasons above and based on the XTT analysis for time dependent change of K562 cell population regarding the drug dosages, the viability observation in experiments was sufficiently short-term and primarily based on the **fluorescence intensity change**. Accordingly, the duration in the control group experiments was kept as maximum 3 hours before the droplets became unstable.

The integrity of cell membranes was examined using the devices only with microchannel configuration for the proof-of-concept. The K-562 leukemia cancer cells encapsulated within the droplets of drug content were observed under the fluorescent microscope. Firstly, ‘a control group experiment’ was carried out to investigate the viability of cells that did not receive any drug, thus providing an empirical reference to the effect of drugs. The test has been performed until the droplets lost their stability due to shrinkage. The level of cell fluorescence intensity was measured over the time

using an analysis method known as corrected total cell fluorescence (CTCF). Using ImageJ, fluorescence of each cell was analyzed and measured together with that of background. Then, CTCF can be calculated removing the background intensity over the area of cell from integrated density. Figure 4.4 demonstrates the results of experiment for the control group. Figure 4.5 indicates that the fluorescence intensity of live cells did not significantly changes compared by integrated density and cells can be preserved alive after 2 hours with no drug used.

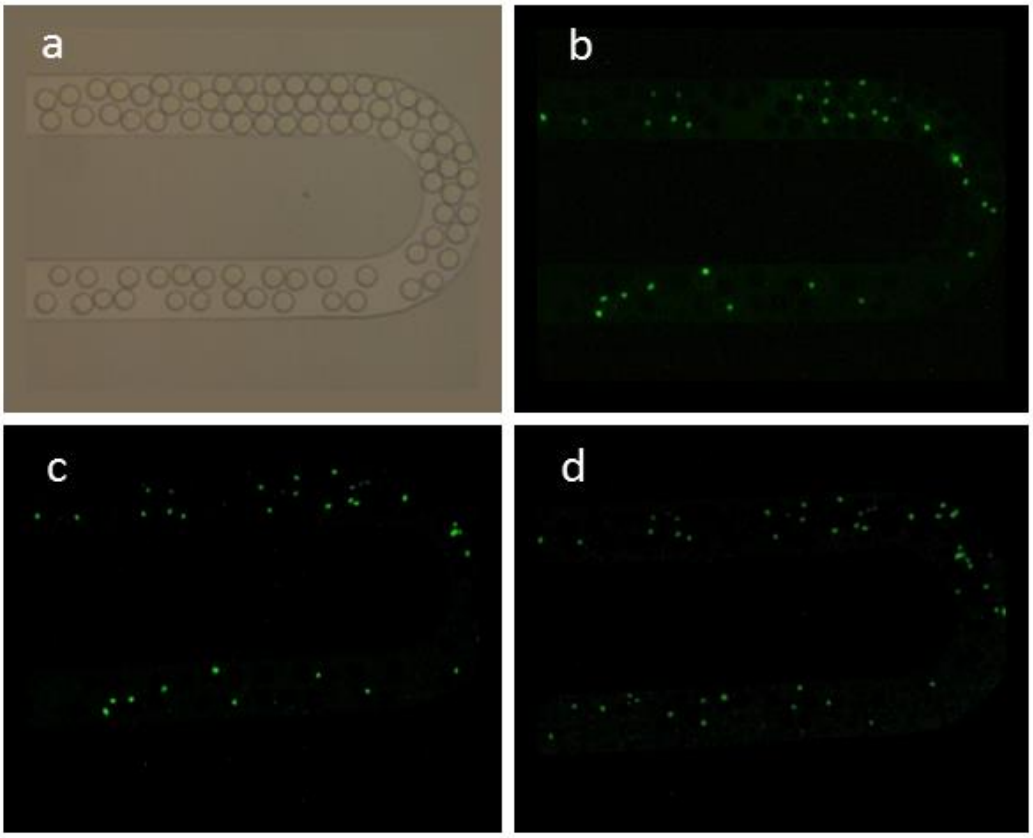


**Figure 4.4.** The results of control group test using FDA with no drug applied. a) Bright field image shows the droplets and cell encapsulate within them. The fluorescent images were taken after b) 0 min, c) 1 hour and d) 2 hours. The intensity of FDA did not significantly decrease over the time. The significant droplet shrinkage was observed.

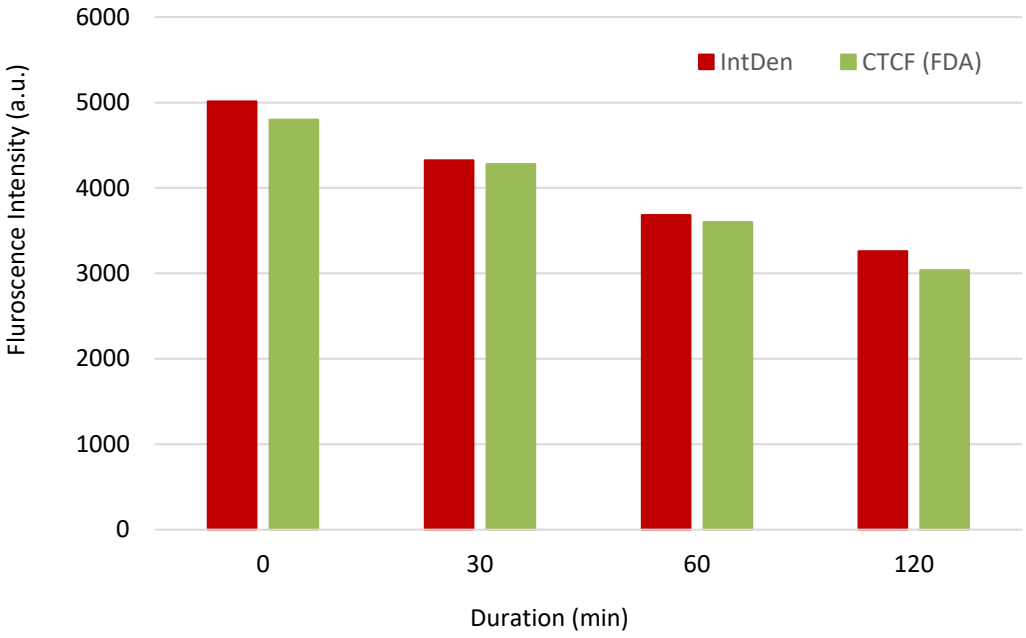


**Figure 4.5.** Time-dependent demonstration of the viability of individual cells trapped in the droplet in the absence of drug. CTCF values for FDA and integrated density are provided. Almost no dead cells observed in 2 hours.

After observing the cell viability for the control group, the kinetic analysis of drug efficacy based on the fluorescent activity were observed. The type of drug whose efficiency was investigated on viability of cells was Doxorubicin with a concentration of 20 µM. The protocol of live/dead cell staining was kept the same as in the previous tests. Figure 4.6 shows the time-lapse images of fluorescently activated cells in the droplets for both FDA and PI up to 2 hours. From CTFC results given in Figure 4.7, it can be interpreted that the brightness of FDA decreased whereas that of PI increased as some of the cells died with doxorubicin concentration of 20 µM.

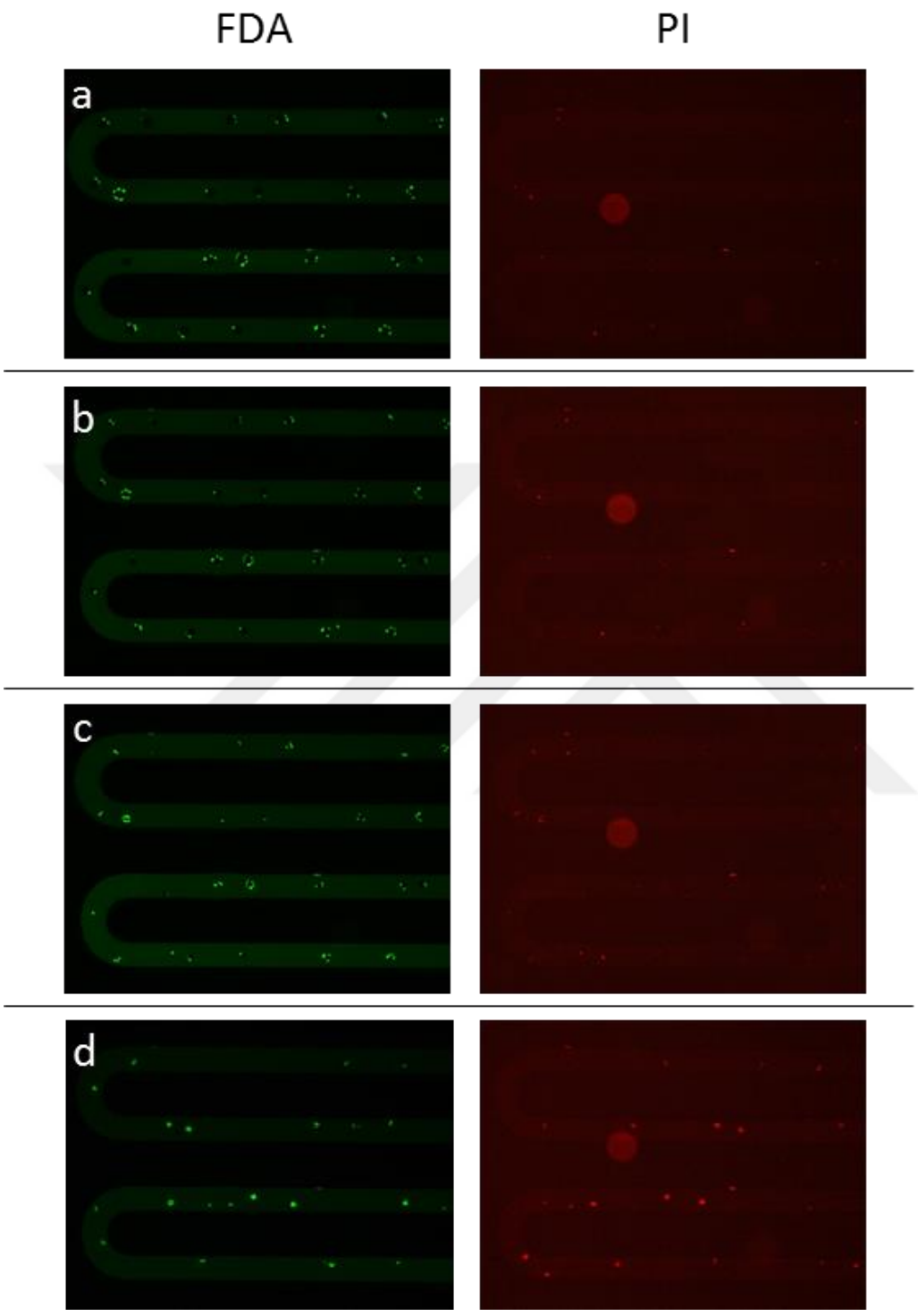


**Figure 4.6.** The results of doxorubicin efficiency test using FDA and PI. The images were taken after a) 0 min, b) 30 min, c) 1 hour and d) 2 hours. The intensity of FDA decreased while that of PI increased as the cells die. The significant droplet shrinkage was observed.

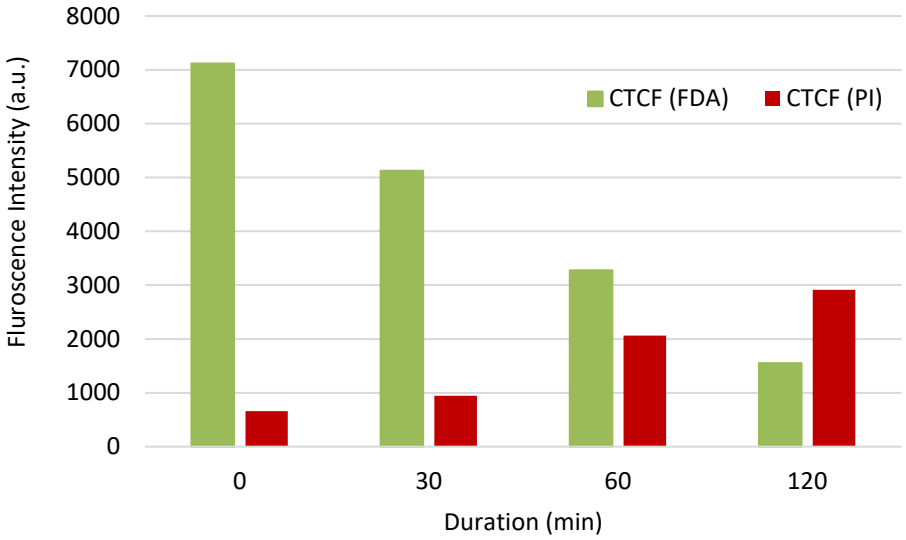


**Figure 4.7.** Time-dependent effect of 20 μM Dox on individual cells trapped in the droplet.

## 4.3. Conclusion

The feasibility of screening drug-cancer cell interactions using a novel lab-on-a-chip system integrated with electrostatic microvalves were demonstrated. The design, operation, and fabrication of the LOC system were presented. Then, the effectivity of the anti-cancer drug, doxorubicin, on K-562 leukemia cancer cells was investigated based on the fluorescent activities of cells dyed with Calcein AM and Propidium Iodide for live and dead cell assays, respectively. The results showed that the fluorescent intensity of the live cells decreased and correspondingly that of dead cells increased after 2 hours. Also, a control group experiment without using any drug was conducted to be able to compare the results. It has been proved that the cells inside the droplets can be alive for 3 hours without drug interaction by observing that the intensity of FDA has not significantly changed. The control group experiment could be maintained up to 3 hours due to shrinkage of droplets under continuous air flow arising from the environment. After all, the proposed LOC system allowed the observation of control group and medicated group and the durations can be extended under proper conditions.

# CHAPTER 5

# CONCLUSION AND FUTURE WORK

The development of a platform allowing the simultaneous and real-time observations of multiple drugs and their combinations was performed. The design details and working principle of the device were explained. Then, droplet microfluidics was the subject that had an important place in the application purpose. The droplet formation tests were performed using the PDMS/glass plasma bonded devices based on the simulation results and necessary calculations. Also, single cell encapsulation tests were performed. fabrication methods were explained.

The proposed electrostatic microvalve was dedicated for a part of the drug efficiency analysis platform. The importance of the valves for this system was that integration of more than one valve enables the use of multiple drugs and their combinations for the simultaneous observations on cancer cells. Then, the emergent total analysis system becomes a powerful tool for the patient specific treatments of cancers.

Based on the established analytical model of electrostatic microvalve, the design of a normally closed type electrostatic microvalve design proposed, fabrication flow was explained, and the performance of the fabricated valves were thoroughly elaborated. Upon the problems of first-generation devices, a second-generation design was asserted for the necessity. While keeping the operation mechanisms the same, the design was developed for the new fabrication proposals. The results showed that the performance of the microvalves were significantly increased in terms of pull-in voltage, response time, repeatability and number of operating microvalves per device.

At the end, the proof-of-concept for testing the system for drug efficiency analysis was demonstrated. The analyses were made on K-562 leukemia cells based on cell encapsulation in droplets approach. The encapsulated cells in different drug droplets of picolitres were observed their responses over the time under fluorescent microscope. The results indicated that the proof-of-concept for observing drug responses at single cell level was demonstrated based on the fluorescence intensity change.

As a future work, the lab-on-a-chip system including six different valves will be first of all used in the experiments. In the experiments presented above, the duration was limited to couple of hours due to droplet stabilization issues. In the future, the duration of drug efficiency screening will be extended at a desired level. Moreover, different types of drugs and their combinations will be observed at the same time at different observation areas of the LOC system. In addition to all these, if the complete system functions properly, it can be integrated with a cell separation platform using dielectrophoresis so that the disease diagnosis and therapy can be conducted at the same time on the same LOC system.

## REFERENCES


[1] "MEMS Microphone: Market, Applications and Business Trends 2014 R…." [Online]. Available: https://www.slideshare.net/Yole_Developpement/yole-mems-microphne2014sample. [Accessed: 20-Jul-2017].

[2] A. Manz, H. M. Widmers, and N. Graber, "Miniaturized total chemical analysis systems: A novel concept for chemical sensing," *Sensors Actuators B Chem.*, vol. 1, no. 1–6, pp. 244–248, 1990.

[3] G. M. Whitesides, "The origins and the future of microfluidics.," *Nature*, vol. 442, no. 7101, pp. 368–73, 2006.

[4] S. C. Terry, J. H. Herman, and J. B. Angell, "A gas chromatographic air analyzer fabricated on a silicon wafer," *IEEE Transactions on Electron Devices*, vol. 26, no. 12. pp. 1880–1886, 1979.

[5] H. J. Fritz *et al.*, "High-pressure liquid chromatography in polynucleotide synthesis.," *Biochemistry*, vol. 17, no. 7, pp. 1257–67, 1978.

[6] J. Frenz and W. S. Hancock, "High performance capillary electrophoresis.," *Trends Biotechnol.*, vol. 9, no. 7, pp. 243–250, 1991.

[7] A. W. Martinez, S. T. Phillips, G. M. Whitesides, and E. Carrilho, "Diagnostics for the developing world: Microfluidic paper-based analytical devices," *Anal. Chem.*, vol. 82, no. 1, pp. 3–10, 2010.

[8] L. Y. Wu, D. Di Carlo, and L. P. Lee, "Microfluidic self-assembly of tumor spheroids for anticancer drug discovery," *Biomed. Microdevices*, vol. 10, no. 2, pp. 197–202, 2008.

[9] J. Ji, F. E. H. Tay, J. Miao, and C. Iliescu, "Microfabricated silicon microneedle array for transdermal drug delivery," *J. Phys. Conf. Ser.*, vol. 34, no. 1, pp. 1127–1131, 2006.

[10] V. Srinivasan, V. K. Pamula, and R. B. Fair, "An integrated digital microfluidic lab-on-a-chip for clinical diagnostics on human physiological fluids.," *Lab*

*Chip*, vol. 4, no. 4, pp. 310–315, 2004.

[11] B. T. C. Lau, C. A. Baitz, X. P. Dong, and C. L. Hansen, "A complete microfluidic screening platform for rational protein crystallization," *J. Am. Chem. Soc.*, vol. 129, no. 3, pp. 454–455, 2007.

[12] D. S. Kong, P. A. Carr, L. Chen, S. Zhang, and J. M. Jacobson, "Parallel gene synthesis in a microfluidic device," *Nucleic Acids Res.*, vol. 35, no. 8, 2007.

[13] J. F. Edd *et al.*, "Controlled encapsulation of single-cells into monodisperse picolitre drops.," *Lab Chip*, vol. 8, no. 8, pp. 1262–4, Aug. 2008.

[14] L. Shui, S. Pennathur, J. C. T. Eijkel, and A. van den Berg, "Multiphase flow in lab on chip devices: A real tool for the future?," *Lab Chip*, vol. 8, no. 7, p. 1010, 2008.

[15] T. Glawdel and C. L. Ren, "Droplet production and transport in microfluidic networks with pressure driven flow control," *Mech. Mechatronics Eng.*, vol. PhD, p. 319, 2012.

[16] T. M. Squires and S. R. Quake, "Microfluidics: Fluid physics at the nanoliter scale," *Rev. Mod. Phys.*, vol. 77, no. 3, pp. 977–1026, 2005.

[17] S. C. Bendall *et al.*, "Single-cell mass cytometry of differential immune and drug responses across a human hematopoietic continuum," *Science (80-. ).*, vol. 332, no. 6030, pp. 687–696, 2011.

[18] F. Courtois *et al.*, "An integrated device for monitoring time-dependent in vitro expression from single genes in picolitre droplets," *ChemBioChem*, vol. 9, no. 3, pp. 439–446, 2008.

[19] B. J. Hindson *et al.*, "High-throughput droplet digital PCR system for absolute quantitation of DNA copy number," *Anal. Chem.*, vol. 83, no. 22, pp. 8604–8610, 2011.

[20] N. R. Beer *et al.*, "On-chip, real-time, single-copy polymerase chain reaction in picoliter droplets," *Anal. Chem.*, vol. 79, no. 22, pp. 8471–8475, 2007.

[21] M. M. Kiss *et al.*, "High-throughput quantitative polymerase chain reaction in picoliter droplets," *Anal. Chem.*, vol. 80, no. 23, pp. 8975–8981, 2008.

[22] C. Zhang, J. Xu, W. Ma, and W. Zheng, “PCR microfluidic devices for DNA amplification,” *Biotechnology Advances*, vol. 24, no. 3. pp. 243–284, 2006.

[23] A. Huebner *et al.*, “Static microdroplet arrays: a microfluidic device for droplet trapping, incubation and release for enzymatic and cell-based assays,” *Lab Chip*, vol. 9, no. 5, pp. 692–698, 2009.

[24] J. R. Burns and C. Ramshaw, “The intensification of rapid reactions in multiphase systems using slug flow in capillaries.,” *Lab Chip*, vol. 1, no. 1, pp. 10–15, 2001.

[25] J. W. Kim, A. S. Utada, A. Fern??ndez-Nieves, Z. Hu, and D. a. Weitz, “Fabrication of monodisperse gel shells and functional microgels in microfluidic devices,” *Angew. Chemie - Int. Ed.*, vol. 46, no. 11, pp. 1819–1822, 2007.

[26] R. K. Shah, J.-W. Kim, J. J. Agresti, D. a. Weitz, and L.-Y. Chu, “Fabrication of monodisperse thermosensitive microgels and gel capsules in microfluidic devices,” *Soft Matter*, vol. 4, no. 12, p. 2303, 2008.

[27] E. Brouzes *et al.*, “Droplet microfluidic technology for single-cell high-throughput screening,” *Proc. Natl. Acad. Sci.*, vol. 106, no. 34, pp. 14195–14200, 2009.

[28] J. F. Edd *et al.*, “Controlled encapsulation of single-cells into monodisperse picolitre drops,” *Lab Chip*, vol. 8, no. 8, p. 1262, 2008.

[29] H. S. Kim, T. P. Devarenne, and A. Han, “A high-throughput microfluidic single-cell screening platform capable of selective cell extraction,” *Lab Chip*, vol. 15, no. 11, pp. 2467–2475, 2015.

[30] J. M. Irish, N. Kotecha, and G. P. Nolan, “Mapping normal and cancer cell signalling networks: towards single-cell proteomics.,” *Nat. Rev. Cancer*, vol. 6, no. 2, pp. 146–155, 2006.

[31] D. Wang and S. Bodovitz, “Single cell analysis: The new frontier in ‘omics,’” *Trends in Biotechnology*, vol. 28, no. 6. pp. 281–290, 2010.

[32] V. Lecault, A. K. White, A. Singhal, and C. L. Hansen, “Microfluidic single

cell analysis: From promise to practice," *Current Opinion in Chemical Biology*, vol. 16, no. 3–4. pp. 381–390, 2012.

[33] Z. Gong *et al.*, "Drug effects analysis on cells using a high throughput microfluidic chip," *Biomed. Microdevices*, vol. 13, no. 1, pp. 215–219, 2011.

[34] K. W. Oh and C. H. Ahn, "A review of microvalves," *J. Micromechanics Microengineering*, vol. 16, no. 5, pp. R13–R39, 2006.

[35] J. Kim *et al.*, "Photopolymerized check valve and its integration into a pneumatic pumping system for biocompatible sample delivery," *Lab Chip*, vol. 6, no. 8, p. 1091, 2006.

[36] J. M. Chen, P. C. Huang, and M. G. Lin, "Analysis and experiment of capillary valves for microfluidics on a rotating disk," *Microfluid. Nanofluidics*, vol. 4, no. 5, pp. 427–437, 2008.

[37] B. J. Kirby, T. J. Shepodd, and E. F. Hasselbrink, "Voltage-addressable on/off microvalves for high-pressure microchip separations," *J. Chromatogr. A*, vol. 979, no. 1–2, pp. 147–154, 2002.

[38] S. C. Jacobson, S. V. Ermakov, and J. M. Ramsey, "Minimizing the number of voltage sources and fluid reservoirs for electrokinetic valving in microfluidic devices," *Anal. Chem.*, vol. 71, no. 15, pp. 3273–3276, 1999.

[39] A. Meckes, J. Behrens, W. Benecke, and K. Strasse, "Electromagnetically Driven Microvalve Fabricated in Silicon," pp. 0–3, 1997.

[40] J. S. Bintoro and P. J. Hesketh, "An electromagnetic actuated on/off microvalve fabricated on top of a single wafer," *J. Micromechanics Microengineering*, vol. 15, no. 6, pp. 1157–1173, 2005.

[41] J. Sutanto, P. J. Hesketh, and Y. H. Berthelot, "Design, microfabrication and testing of a CMOS compatible bistable electromagnetic microvalve with latching/unlatching mechanism on a single wafer," *J. Micromechanics Microengineering*, vol. 16, no. 2, p. 266, 2006.

[42] I. Fazal and M. C. Elwenspoek, "Design and analysis of a high pressure piezoelectric actuated microvalve," *J. Micromechanics Microengineering*, vol.

17, no. 11, pp. 2366–2379, 2007.

[43] H. Q. Li *et al.*, “Fabrication of a high frequency piezoelectric microvalve,” in *Sensors and Actuators, A: Physical*, 2004, vol. 111, no. 1, pp. 51–56.

[44] D. C. Roberts *et al.*, “A piezoelectric microvalve for compact high-frequency, high-differential pressure hydraulic micropumping systems,” *J. Microelectromechanical Syst.*, vol. 12, no. 1, pp. 81–92, 2003.

[45] L. Yobas, S. Martens, W.-L. Ong, and N. Ranganathan, “High-performance flow-focusing geometry for spontaneous generation of monodispersed droplets,” *Lab Chip*, vol. 6, no. 8, p. 1073, 2006.

[46] C. Goll, W. Bacher, B. Büstgens, D. Maas, R. Ruprecht, and W. K. Schomburg, “An electrostatically actuated polymer microvalve equipped with a movable membrane electrode,” *J. Micromechanics Microengineering*, vol. 7, no. 3, pp. 224–226, 1997.

[47] A. V. Desai, J. D. Tice, C. A. Apblett, and P. J. A. Kenis, “Design considerations for electrostatic microvalves with applications in poly(dimethylsiloxane)-based microfluidics,” *Lab Chip*, vol. 12, no. 6, p. 1078, 2012.

[48] D. E. Lee, S. Soper, and W. Wang, “Design and fabrication of an electrochemically actuated microvalve,” in *Microsystem Technologies*, 2008, vol. 14, no. 9–11, pp. 1751–1756.

[49] C. R. Neagu, J. G. E. Gardeniers, M. Elwenspoek, and J. J. Kelly, “An electrochemical microactuator: Principle and first results,” *J. Microelectromechanical Syst.*, vol. 5, no. 1, pp. 2–9, 1996.

[50] H. Suzuki and R. Yoneyama, “Integrated microfluidic system with electrochemically actuated on-chip pumps and valves,” *Sensors Actuators, B Chem.*, vol. 96, no. 1–2, pp. 38–45, 2003.

[51] C. R. Neagu, J. G. E. Gardeniers, M. Elwenspoek, and J. J. Kelly, “An electrochemical active valve,” *Electrochim. Acta*, vol. 42, no. 20–22, pp. 3367–3373, 1997.

[52] R. Pal, M. Yang, B. N. Johnson, D. T. Burke, and M. A. Burns, “Phase change

microvalve for integrated devices," *Anal. Chem.*, vol. 76, no. 13, pp. 3740–3748, 2004.

[53] B. Yang and Q. Lin, "A latchable microvalve using phase change of paraffin wax," *Sensors Actuators, A Phys.*, vol. 134, no. 1, pp. 194–200, 2007.

[54] A. Luque, J. M. Quero, C. Hibert, P. Flückiger, and A. M. Gañán-Calvo, "Integrable silicon microfluidic valve with pneumatic actuation," *Sensors Actuators, A Phys.*, vol. 118, no. 1, pp. 144–151, 2005.

[55] K. Hosokawa and R. Maeda, "A pneumatically-actuated three-way microvalve fabricated with polydimethylsiloxane using the membrane transfer technique," *J. Micromechanics Microengineering*, vol. 10, no. 3, p. 415, 2000.

[56] J. Y. Baek, J. Y. Park, J. Il Ju, T. S. Lee, and S. H. Lee, "A pneumatically controllable flexible and polymeric microfluidic valve fabricated via in situ development," *J. Micromech. Microeng*, vol. 15, pp. 1015–1020, 2005.

[57] H. Takao, M. Ishida, and K. Sawada, "A pneumatically actuated full in-channel microvalve with MOSFET-like function in fluid channel networks," *J. Microelectromechanical Syst.*, vol. 11, no. 5, pp. 421–426, 2002.

[58] H. Sugioka, "High-speed rotary microvalves in water using hydrodynamic force due to induced-charge electrophoresis," *Phys. Rev. E - Stat. Nonlinear, Soft Matter Phys.*, vol. 81, no. 3, 2010.

[59] S. Saliterman, *Fundamentals of bioMEMS and medical microdevices*. Wiley-Interscience, 2006.

[60] M. A. Unger, H. P. Chou, T. Thorsen, A. Scherer, and S. R. Quake, "Monolithic microfabricated valves and pumps by multilayer soft lithography.," *Science*, vol. 288, no. 5463, pp. 113–6, 2000.

[61] K. a Addae-Mensah, Y. K. Cheung, V. Fekete, M. S. Rendely, and S. K. Sia, "Actuation of elastomeric microvalves in point-of-care settings using handheld, battery-powered instrumentation.," *Lab Chip*, vol. 10, pp. 1618–1622, 2010.

[62] N. T. Nguyen and S. Wereley, "Fundamentals and applications of microfluidics," *Artech House*, p. 111, 2006.

[63] T. L. Sounart, T. A. Michalske, and K. R. Zavadil, “Frequency-dependent electrostatic actuation in microfluidic MEMS,” *J. Microelectromechanical Syst.*, vol. 14, no. 1, pp. 125–133, 2005.

[64] M.-P. Chang and M. M. Maharbiz, “Electrostatically-driven elastomer components for user-reconfigurable high density microfluidics.,” *Lab Chip*, vol. 9, no. 9, pp. 1274–81, 2009.

[65] E. Yıldırım, “Design and Implementation of Low Leakage MEMS Microvalves,” 2011.

[66] E. Yildirim, H. Kulah, and M. A. S. Arikan, “An electrostatically actuated parylene microvalve for lab-on-a-chip applications,” in *2011 16th International Solid-State Sensors, Actuators and Microsystems Conference, TRANSDUCERS’11*, 2011, pp. 250–253.

[67] E. Yildirim, M. A. S. Arikan, and H. Külah, “A normally closed electrostatic parylene microvalve for micro total analysis systems,” *Sensors Actuators, A Phys.*, vol. 181, pp. 81–86, 2012.

[68] P. B. Umbanhowar, V. Prasad, and D. A. Weitz, “Monodisperse emulsion generation via drop break off in a coflowing stream,” *Langmuir*, vol. 16, no. 2, pp. 347–351, 2000.

[69] J. Hua, B. Zhang, and J. Lou, “Numerical simulation of microdroplet formation in coflowing immiscible liquids,” *AIChE J.*, vol. 53, no. 10, pp. 2534–2548, 2007.

[70] S. L. Anna, N. Bontoux, and H. A. Stone, “Formation of dispersions using ‘flow focusing’ in microchannels,” *Appl. Phys. Lett.*, vol. 82, no. 3, pp. 364–366, 2003.

[71] P. Garstecki, I. Gitlin, W. Diluzio, G. M. Whitesides, E. Kumacheva, and H. A. Stone, “Formation of monodisperse bubbles in a microfluidic flow-focusing device,” *Appl. Phys. Lett.*, vol. 85, no. 13, pp. 2649–2651, 2004.

[72] Q. Xu and M. Nakajima, “The generation of highly monodisperse droplets through the breakup of hydrodynamically focused microthread in a microfluidic device,” *Appl. Phys. Lett.*, vol. 85, no. 17, pp. 3726–3728, 2004.

[73] J. H. Xu, S. W. Li, J. Tán, Y. J. Wang, and G. S. Luo, “Preparation of highly monodisperse droplet in a T-junction microfluidic device,” *AIChE J.*, vol. 52, no. 9, pp. 3005–3010, 2006.

[74] P. Garstecki, M. J. Fuerstman, H. a Stone, and G. M. Whitesides, “Formation of droplets and bubbles in a microfluidic T-junction-scaling and mechanism of break-up.,” *Lab Chip*, vol. 6, no. 3, pp. 437–446, 2006.

[75] T. Nisisako, T. Torii, and T. Higuchi, “Droplet formation in a microchannel network.,” *Lab Chip*, vol. 2, no. 1, pp. 24–26, 2002.

[76] H. Liu and Y. Zhang, “Droplet formation in a T-shaped microfluidic junction,” *J. Appl. Phys.*, vol. 106, no. 3, 2009.

[77] W. M. Zhang, H. Yan, Z. K. Peng, and G. Meng, “Electrostatic pull-in instability in MEMS/NEMS: A review,” *Sensors Actuators, A Phys.*, vol. 214, pp. 187–218, 2014.

[78] H. C. Nathanson, W. E. Newell, R. A. Wickstrom, and J. R. Davis, “The resonant gate transistor,” *IEEE Trans. Electron Devices*, vol. 14, no. 3, pp. 117–133, 1967.

[79] S. D. Senturia, *Microsystem Design*, vol. 49, no. 0. 2001.

[80] G. W. Vogl and A. H. Nayfeh, “A reduced-order model for electrically actuated clamped circular plates,” *J. Micromechanics Microengineering*, vol. 15, no. 4, pp. 684–690, 2005.

[81] L. De Liao, P. C. P. Chao, C. W. Huang, and C. W. Chiu, “Dc dynamic and static pull-in predictions and analysis for electrostatically actuated clamped circular micro-plates based on a continuous model,” *J. Micromechanics Microengineering*, vol. 20, no. 2, 2010.

[82] P. C. P. Chao, C. W. Chiu, and C. Y. Tsai, “A novel method to predict the pull-in voltage in a closed form for micro-plates actuated by a distributed electrostatic force,” *J. Micromechanics Microengineering*, vol. 16, no. 5, pp. 986–998, 2006.

[83] G. N. Nielson and G. Barbastathis, “Dynamic pull-in of parallel-plate and

torsional electrostatic MEMS actuators," *J. Microelectromechanical Syst.*, vol. 15, no. 4, pp. 811–821, 2006.

[84] H. C. Koydemir, H. Kulah, and C. Ozgen, "Solvent Compatibility of Parylene C Film Layer," *J. Microelectromechanical Syst.*, vol. 23, no. 2, pp. 298–307, 2014.

[85] H. Ceylan Koydemir, H. Külah, C. Özgen, and I. Tosun, "Effects of solvents on dissolution of photoresist in parylene microchannels," in *Nanotechnology 2012: Electronics, Devices, Fabrication, MEMS, Fluidics and Computational - 2012 NSTI Nanotechnology Conference and Expo, NSTI-Nanotech 2012*, 2012, vol. Santa Clar, pp. 372–375.

[86] Z. Yapu, "Stiction and anti-stiction in MEMS and NEMS," *Acta Mech. Sin.*, vol. 19, no. l, pp. 1–10, 2003.

[87] N. Takeshima, K. J. Gabriel, M. Ozaki, J. Takahashi, H. Horiguchi, and H. Fujita, "Electrostatic parallelogram actuators," in *TRANSDUCERS '91: 1991 International Conference on Solid-State Sensors and Actuators. Digest of Technical Papers*, 1991, pp. 63–66.

[88] J. R. Gilbert, G. K. Ananthasuresh, and S. D. Senturia, "{3D} modeling of contact problems and hysteresis in coupled electro-mechanics," *Proc. 9th Annu. Int. Work. Micro Electro Mech. Syst. (MEMS '96)*, pp. 127–132, 1996.

[89] D. Wlodkowic, S. Faley, M. Zagnoni, J. P. Wikswo, and J. M. Cooper, "Microfluidic single-cell array cytometry for the analysis of tumor apoptosis," *Anal. Chem.*, vol. 81, no. 13, pp. 5517–5523, 2009.

[90] I. Barbulovic-Nad, S. H. Au, and A. R. Wheeler, "A microfluidic platform for complete mammalian cell culture," *Lab Chip*, vol. 10, no. 12, p. 1536, 2010.

# APPENDICES

## APPENDIX A

## PROCESS FLOWS

**Table A.0.1:** Process flow of a first-generation normally closed electrostatic microvalve and microchannel network, namely the first-generation lab-on-a-chip system.

| Step | Process Step | | Comment |
|---|---|---|---|
| 1 | **Substrate-Silicon <100> OSP** | Orientation: <100><br>Diameter: 150mm (6")<br>Thickness: 525µm +/- 25µm<br>Polished: Single side (OSP)<br>Resistivity: 5-10Ωcm<br>Type: p | |
| 2 | **Photolithography**<br>Mask: Actuation Chamber and Air Vent | 1. Dehydration at 110 °C for 20 min.<br>2. Spin HMDS at 1000 rpm for 30 sec, at 4000 rpm for 30 sec.<br>3. Spin AZ 5124 at 1000 rpm for 30 sec, at 4000 rpm for 30 sec.<br>4. Soft bake at 115 °C for 30 sec (above) +60 sec.<br>5. Exposure at 14 mW/sec for 5 sec.<br>6. Post exposure bake at 120 °C for 120 sec. (!)<br>7. Flood Exposure at 14 mW/sec for 20 sec.<br>8. Development using MF319 for 70 sec.<br>9. Rinse (2x90 sec) and dry.<br>10. Hard Bake at 110 °C for 20 min. | Define locations of actuation chambers and air vent channels |
| 3 | **DRIE** | 1. Santez-2 recipe (20 sec).<br>2. $O_2$ plasma for polymer removal. | |
| 4 | **Parylene Deposition** | 1. Parylene coating with SILANE for a thickness of 0.5 µm. | 1 gr for electrical insulation |

| | | | |
|---|---|---|---|
| 5 | **Bottom Electrode Sputtering** | 1. Dehydration at 90 °C for 10 min.<br>2. Ti sputtering (AJA/Bestec) at 350 W for 180 sec. (20nm).<br>3. Au sputtering (AJA/Bestec) at 350 W for 540 sec. (200nm). | |
| 6 | **Photolithography**<br>Mask: Bottom Electrode | 1. Dehydration at 90 °C for 10 min.<br>2. Spin HMDS at 500 rpm for 15 sec, at 3300 rpm for 40 sec.<br>3. Spin SPR 220-7 at 500 rpm for 15 sec, at 3300 rpm for 40 sec.<br>4. Soft bake at 115 °C for 30 sec (above) + 2:30 min.<br>5. Edge Bead Removal at 1000 rpm!<br>6. Exposure at 14 mW/sec for 45 sec.<br>7. Development using MF319 for 90 sec.<br>8. Rinse (2x90 sec) and dry.<br>9. Hard Bake at 90 °C for 40 min. | Define locations of bottom electrodes |
| 7 | **Wet Etch** | 1. Descum at 300 W for (2x2min).<br>2. Etch Au using transgene gold etchant for 60 sec.<br>3. Rinse (2x90 sec), dry and inspect<br>4. Etch Ti using etchant an etchant for 45 sec., prepare 4000 ml $H_2O$ + 25 ml HF + 25 ml $H_2O_2$.<br>5. Rinse (2x90 sec) and dry and inspect.<br>6. PR strip (SVC-14) | |
| 8 | **Photolithography**<br>Mask: Actuation Chamber and Air Vent | 1. Dehydration at 90 °C for 10 min.<br>2. Spin HMDS at 500 rpm for 15 sec, at 1000 rpm for 60 sec.<br>3. Spin SPR 220-3 at 500 rpm for 15 sec, at 1000 rpm for 60 sec.<br>4. Soft bake at 115 °C for 30 sec (above) + 2:30 min.<br>5. Edge Bead Removal at 750 rpm!<br>6. Exposure at 14 mW/sec for 45 sec.<br>7. Development using MF319 for 90 sec.<br>8. Rinse (2x90 sec) and dry.<br>9. Inspect with Dektak.<br>10. Hard Bake at 90 °C for 3-5 hrs. | Fill actuation chambers and air vent channels |
| 9 | **Parylene Deposition** | 1. Parylene coating without silane for a thickness of 2.5 µm. | 5 gr<br>Diaphragm |

| | | | |
|---|---|---|---|
| 10 | **Top Electrode Sputtering** | 1. Dehydration at 90 °C for 10 min.<br>2. Ti sputtering (AJA/Bestec) at 75 W for 180 sec. (20nm).<br>3. Au sputtering (AJA/Bestec) at 75 W for 540 sec. (200nm). | |
| 11 | **Photolithography**<br>Mask: Top Electrode | 1. Dehydration at 90 °C for 10 min.<br>2. Spin HMDS at 500 rpm for 15 sec, at 3300 rpm for 40 sec.<br>3. Spin SPR 220-7 at 500 rpm for 15 sec, at 3300 rpm for 40 sec.<br>4. Soft bake at 115 °C for 30 sec (above) + 2:30 min.<br>5. Edge Bead Removal at 1000 rpm!<br>6. Exposure at 14 mW/sec for 45 sec.<br>7. Development using MF319 for 90 sec.<br>8. Rinse (2x90 sec) and dry.<br>9. Hard Bake at 90 °C for 40 min. | Define locations of top electrodes |
| 12 | **Wet Etch** | 1. Descum at 300 W for (2x2min).<br>2. Etch Au using transgene gold etchant for 60 sec.<br>3. Rinse (2x90 sec), dry and inspect.<br>4. Etch Ti using etchant an etchant for 45 sec., prepare 4000 ml $H_2O$ + 25 ml HF + 25 ml $H_2O_2$.<br>5. Rinse (2x90 sec) and dry and inspect.<br>6. PR strip (SVC-14). | |
| 13 | **Parylene Deposition** | 1. Parylene coating without silane for a thickness of 1 µm. | 2 gr<br>To prevent electrolysis |
| 14 | **Photolithography**<br>Mask: Channel | 1. Dehydration at 90 °C for 10 min.<br>2. Spin HMDS at 500 rpm for 10 sec, at 1500 rpm (2400 rpm) for 30 sec.<br>3. Spin AZ 40 XT at 500 rpm for 10 sec, at 1500 rpm (2400 rpm) for 30 sec.<br>4. Wait horizontally for 2 hours.<br>5. Soft bake at 126 °C initially in air, vertical teflon, horizontal teflon, tweezer for 2 min each. Then, continue soft bake at 126 °C on hot plate for 7 min.<br>6. Edge Bead Removal at 1000 rpm!<br>7. Exposure at 14 mW/sec for 22.5 sec + 22.5 sec (35 sec).<br>8. Wait for 15 min. | Microchannel Formation<br>1500 rpm => 50 µm<br>2400 rpm => 25 µm |

| | | | |
|---|---|---|---|
| | | 9. Post exposure bake at 105°C for 90 sec.<br>10. Development using AZ 826 MIF for 2:30-3:30 min (2-2:30 min).<br>11. Rinse (2x90 sec) and dry. | |
| 15 | **Parylene Deposition** | 1. Parylene coating without silane for a thickness of 10 µm. | 20 gr<br>To form microchannels |
| 16 | **Photolithography**<br>Mask: Opening | 1. Dehydration at 90 °C for 10 min.<br>2. Spin HMDS at 500 rpm for 10 sec, at 750 rpm for 30 sec.<br>3. Spin AZ 9260 at 500 rpm for 10 sec, at 750 rpm for 30 sec. (30 µm)<br>4. Pre-bake at 115 °C for 3 min.<br>5. 15 min-relaxation in horizontal cassette.<br>6. Edge Bead Removal at 1000 rpm!<br>7. Soft bake ramping from room temperature to 90 °C for 1 hr.<br>8. Rehydration for minimum 1 hr. (can be a day)<br>9. Exposure at 14 mW/sec for 35 sec.<br>10. Development using AZ 826-MIF for 30 min.<br>11. Rinse (2x90 sec) and dry. | Define locations of inlets and outlets |
| 17 | **Parylene RIE** | 1. Parylene etch under $O_2$ and $CF_4$ flow for 45 min.,<br>2. Inspect. | 20 min + 15 min + 10 min. |
| 18 | **Release** | 1. Dicing (wafers can be coated with SPR 220-3)<br>2. Immerse dies in acetone for 5-8 days,<br>3. Treatment with IPA and methanol for 30 min, both.<br>4. Treatment with liquid t-butyl alcohol for 30 min,<br>5. Placing device in the refrigerator for couple of min. for t-butyl alcohol to freeze,<br>6. Placing device under vacuum for sublimation for 3 hrs. | |

**Table B.0.2:** Process flow of a second-generation normally closed electrostatic microvalve and microchannel network, namely the second-generation lab-on-a-chip system.

| Step | Process Step | Comment |
|---|---|---|
| | **Microvalve Fabrication on Glass Wafer** | |
| 1 | **Substrate - Glass**<br>Diameter: 150mm (6")<br>Thickness: 300µm +/- 25µm<br>Piranha Cleaned | |
| 2 | **Cr/Au Sputtering**<br>1. Dehydration at 110 °C for 20 min.<br>2. Cr sputtering (AJA/Bestec) at 300 W for 50nm.<br>3. Au sputtering (AJA/Bestec) at 350 W for 500nm. | Creation of masking layer for glass etching |
| 3 | **Photolithography**<br>Mask: Actuation Chamber and Air Vent<br>1. Dehydration at 110 °C for 20 min.<br>2. Spin HMDS at 1000 rpm for 30 sec, at 4000 rpm for 30 sec.<br>3. Spin AZ 5124 at 1000 rpm for 30 sec, at 4000 rpm for 30 sec.<br>4. Soft bake at 115 °C for 30 sec (above) +60 sec.<br>5. Exposure at 14 mW/sec for 5 sec.<br>6. Post exposure bake at 120 °C for 120 sec. (!)<br>7. Flood Exposure at 14 mW/sec for 20 sec.<br>8. Development using MF319 for 70 sec.<br>9. Rinse (2x90 sec) and dry.<br>10. Hard Bake at 110 °C for 40 min from RT. | Define locations of actuation chambers and air vent channels |
| 4 | **Wet Etch**<br>1. Descum at 150 W for (2x3min).<br>2. Etch Au using transgene gold etchant for 50 sec.<br>3. Rinse (2x90 sec), dry and inspect.<br>4. Etch Cr using commercial etchant for 40 sec and then immerse in 2% $H_2SO_4$ solution (7000 ml $H_2O$ + 140 ml $H_2SO_4$) for 15 seconds.<br>5. Rinse (2x90 sec) and dry and inspect.<br>6. PR strip (PRS 2000). | |

| | | | |
|---|---|---|---|
| 5 | **Glass Etch** | 1. Etch glass for 50 seconds in pure HF while stirring on hotplate.<br>2. Rinse and dry.<br>3. Remove sacrificial PR completely (PRS-2000). | |
| 6 | **Wet Etch** | 1. Completely etch Au using transgene gold etchant.<br>2. Rinse (2x90 sec), dry and inspect.<br>3. Completely etch Cr using commercial etchant and then immerse in 2% $H_2SO_4$ solution (7000 ml $H_2O$ + 140 ml $H_2SO_4$).<br>4. Rinse (2x90 sec) and dry and inspect.<br>5. Immerse in BHF (1:7) for 3 min. | |
| 7 | **Parylene Deposition** | 1. Parylene coating with SILANE for a thickness of 0.5 μm. | 1 gr for electrical insulation |
| 8 | **Bottom Electrode Sputtering** | 1. Dehydration at 90 °C for 10 min.<br>2. Ti sputtering (AJA/Bestec) at 350 W for 20nm.<br>3. Au sputtering (AJA/Bestec) at 350 W for 200nm. | |
| 9 | **Photolithography**<br>Mask: Bottom Electrode | 1. Dehydration at 90 °C for 10 min.<br>2. Spin HMDS at 500 rpm for 15 sec, at 3300 rpm for 40 sec.<br>3. Spin SPR 220-7 at 500 rpm for 15 sec, at 3300 rpm for 40 sec.<br>4. Soft bake at 115 °C for 30 sec (above) + 2:30 min.<br>5. Edge Bead Removal at 1000 rpm!<br>6. Exposure at 14 mW/sec for 45 sec.<br>7. Development using MF319 for 90 sec.<br>8. Rinse (2x90 sec) and dry.<br>9. Hard Bake at 90 °C from RT for 40 min. | Define locations of bottom electrodes |
| 10 | **Wet Etch** | 1. Descum at 150 W for (2x3min).<br>2. Etch Au using transgene gold etchant for 40 sec.<br>3. Rinse (2x90 sec), dry and inspect<br>4. Etch Ti using etchant an etchant for 35 sec (prepare 4000 ml $H_2O$ + 25 ml HF + 25 ml $H_2O_2$).<br>5. Rinse (2x90 sec) and dry and inspect. | |

| | | | |
|---|---|---|---|
| | | 6. PR strip in acetone. | |
| 11 | **Photolithography**<br>Mask: Actuation Chamber and Air Vent | 1. Dehydration at 90 °C for 10 min.<br>2. Spin HMDS at 500 rpm for 15 sec, at 1000 rpm for 60 sec.<br>3. Spin SPR 220-3 at 500 rpm for 15 sec, at 1000 rpm for 60 sec.<br>4. Soft bake at 115 °C for 30 sec (above) + 2:30 min.<br>5. Edge Bead Removal at 750 rpm!<br>6. Exposure at 14 mW/sec for 45 sec.<br>7. Development using MF319 for 90 sec.<br>8. Rinse (2x90 sec) and dry.<br>9. Inspect with Dektak.<br>10. Hard Bake at 90 °C for 6 hours from RT. | Fill actuation chambers and air vent channels |
| 12 | **Parylene Deposition** | 1. Parylene coating without silane for a thickness of 2.5 µm. | 5 gr<br>Diaphragm |
| 13 | **Top Electrode Sputtering** | 1. Dehydration at 90 °C for 10 min.<br>2. Ti sputtering (AJA/Bestec) at 75 W for 20 nm.<br>3. Au sputtering (AJA/Bestec) at 75 W for 200 nm. | |
| 14 | **Photolithography**<br>Mask: Top Electrode | 1. Dehydration at 90 °C for 10 min.<br>2. Spin HMDS at 500 rpm for 15 sec, at 3300 rpm for 40 sec.<br>3. Spin SPR 220-7 at 500 rpm for 15 sec, at 3300 rpm for 40 sec.<br>4. Soft bake at 115 °C for 30 sec (above) + 2:30 min.<br>5. Edge Bead Removal at 1000 rpm!<br>6. Exposure at 14 mW/sec for 45 sec.<br>7. Development using MF319 for 90 sec.<br>8. Rinse (2x90 sec) and dry.<br>9. Hard Bake at 90 °C for 40 min from RT. | Define locations of top electrodes |
| 15 | **Wet Etch** | 1. Descum at 150 W for (2x3min).<br>Etch Au using transgene gold etchant for 40 sec.<br>2. Rinse (2x90 sec), dry and inspect.<br>3. Etch Ti using etchant an etchant for 35 sec (prepare 4000 ml $H_2O$ + 25 ml HF + 25 ml $H_2O_2$).<br>4. Rinse (2x90 sec) and dry and inspect. | |

| | | | |
|---|---|---|---|
| | | 5. PR strip in acetone. | |
| 16 | **Parylene Deposition** | 1. Parylene coating <u>without silane</u> for a thickness of 1 µm. | 2 gr<br><br>To prevent electrolysis |
| 17 | **Photolithography**<br>Mask: Opening | 1. Dehydration <u>at 90 °C</u> for 10 min.<br>2. Spin HMDS at 500 rpm for 10 sec, at 750 rpm for 30 sec.<br>3. Spin AZ 9260 at 500 rpm for 10 sec, at 750 rpm for 30 sec. (30 µm)<br>4. Pre-bake at 115 °C for 3 min.<br>5. 15 min-relaxation in horizontal cassette.<br>6. Edge Bead Removal at 1000 rpm!<br>7. Soft bake ramping from room temperature to 90 °C for 1 hr.<br>8. Rehydration for minimum 1 hr. (can be a day)<br>9. Exposure at 14 mW/sec for 35 sec.<br>10. Development using AZ 826-MIF for 30 min.<br>11. Rinse (2x90 sec) and dry. | Define locations of microchannels, inlets and outlets |
| 18 | **Parylene RIE** | 1. Parylene etch under $O_2$ and $CF_4$ flow for 45 min (20min + 15min + 10min).<br>2. Inspect. | 20 gr<br><br>To form microchannels |
| 19 | **PR Release** | 1. Wafer dicing (priorly SPR 220-3 coating).<br>2. Immerse dies in acetone for 2-3 days.<br>3. Treat with IPA and methanol for 30 minutes each, respectively.<br>4. Immerse dies in liquid t-butyl alcohol for 20 minutes. Keep them at +4 °C for 10 minutes for solidification in refrigerator.<br>5. Perform sublimation of t-butyl alcohol under vacuum for 4-5 hours. | |
| **Mold Wafer and PDMS Microchannel Fabrication** | | | |
| 20 | **Substrate-Silicon <100> OSP** | Orientation: <100><br>Diameter: 150mm (6”)<br>Thickness: 525µm +/- 25µm<br>Polished: Single side (OSP)<br>Resistivity: 5-10Ωcm<br>Type: p | |

| | | | |
|---|---|---|---|
| 20 | **Photolithography**<br>Mask: Channel | 1. Dehydration at 110 °C for 20 min.<br>2. Spin HMDS at 500 rpm for 10 sec, at 1500 rpm (2400 rpm) for 30 sec.<br>3. Spin AZ 40 XT at 500 rpm for 10 sec, at 1500 rpm (2400 rpm) for 30 sec.<br>4. Wait horizontally for 2 hours.<br>5. Soft bake at 126 °C initially in air, vertical teflon, horizontal teflon, tweezer for 2 min each. Then, continue soft bake at 126 °C on hot plate for 7 min.<br>6. Edge Bead Removal at 1000 rpm!<br>7. Exposure at 14 mW/sec for 45 sec (35 sec).<br>8. Wait for 15 min.<br>9. Post exposure bake at 105°C for 90 sec.<br>10. Development using AZ 826 MIF for2:30-3:30 min (2-2:30 min).<br>11. Rinse (2x90 sec) and dry. | Microchannel Formation<br><br>1500 rpm => 50 µm<br><br>2400 rpm => 25 µm |
| 21 | **PDMS Preparation** | 1. Mix the curing agent and elastomer Sylgard 184 at a ratio of 1:10 and stir the mixture for 5 minutes.<br>2. Hold the mixture under vacuum for 1-2 hours to remove air bubbles.<br>3. Pour the PDMS onto the mold wafer and cure in the oven for 2 hours at 80 °C.<br>4. Remove the PDMS form the wafer and cut into pieces and create inlets and outlets using punch. | For PDMS devices on 6” wafer, the mixture of 110 gr is prepared. |
| 22 | **Plasma Bonding PDMS/Glass** | 1. Expose glass die and PDMS channel device to oxygen plasma at 40 W for 40 seconds at a flow rate of 26 sccm.<br>2. Align the two devices under a microscope by dropping methanol in between.<br>3. After alignment, wait until methanol evaporates on hot plate at 110 °C. | |